

**Metal ion and pH Sensors based on Carbon Nanotubes**

by

**Pingping Gou**

B.S. in Chemistry, University of Science and Technology of China, 2003

Master in Chemistry, Brown University, 2005

Submitted to the Graduate Faculty of

Chemistry in partial fulfillment

of the requirements for the degree of

Doctor of Philosophy

University of Pittsburgh

2012

UNIVERSITY OF PITTSBURGH

Dietrich Graduate School of Arts and Sciences

This dissertation was presented

by

Pingping Gou

It was defended on

February 13<sup>th</sup>, 2012

and approved by

Dr. David H. Waldeck, Professor, Department of Chemistry

Dr. Toby Chapman, Associate Professor, Department of Chemistry

Dr. Yi Luo, Assistant Professor, Department of Electrical and Computer Engineering

(Carnegie Mellon University)

Dissertation Advisor: Dr. Alexander Star, Associate Professor, Department of Chemistry

Copyright © by Pingping Gou

2012

## **Metal Ion and pH Sensors based on Carbon Nanotubes**

Pingping Gou, PhD

University of Pittsburgh, 2012

The sensitive and selective detection of metal ions and pH levels is important in environmental and biomedical applications. Conventional methods are limited in their potential due to high cost, big size, and lack of portability. A new system incorporating single-walled carbon nanotubes (SWNTs) modified with polymers or proteins has been developed to create a cost-effective, easy-to-use metal ion/pH sensing platform. This system utilized SWNTs modified with metal ion/pH sensitive materials because pristine SWNTs are only sensitive to high concentrations of metal ions ( $> 1 \text{ mM}$ ), and strong base ( $\text{pH} > 12$ ) or acid ( $\text{pH} < 2$ ), and lack selectivity as well.

This work uses noncovalent functionalization approaches to chemically modify SWNTs because noncovalent modifications do not disrupt SWNT electronic properties. When the modified-SWNT system encounters metal ions or pH solutions, the alteration in modified layers, such as conformational change or charge transfer, initiates signal transduction processes, thus changing the electrical and optical properties of the underlying SWNTs. The properties of modified SWNTs were characterized by a variety of techniques including optical spectroscopy, and electrical transport measurements in solid state or liquid state, through which the transduction mechanism of the system was investigated.

The modified SWNT-based metal ion/pH sensors offer promise in applications and provide a platform for fundamental understanding of the transduction mechanism that help us to develop better chemical sensors in the future.

## TABLE OF CONTENTS

<b>PREFACE.....</b>	<b>XIV</b>
<b>1.0 INTRODUCTION.....</b>	<b>1</b>
<b>1.1 METAL ION SENSORS.....</b>	<b>1</b>
<b>1.1.1 Sensors in Nature .....</b>	<b>1</b>
<b>1.1.2 The Importance of Metal Ion (&amp; pH) Sensors .....</b>	<b>2</b>
<b>1.1.3 Design of Metal Ion Sensors.....</b>	<b>3</b>
<b>1.2 CARBON NANOTUBES .....</b>	<b>4</b>
<b>1.2.1 Physical and Electronic Structure of Carbon Nanotubes .....</b>	<b>4</b>
<b>1.2.2 SWNT Networks .....</b>	<b>9</b>
<b>1.2.3 Noncovalent Chemical Functionalization of SWNTs .....</b>	<b>13</b>
<b>1.2.4 Correlation between Spectroscopic and Electrical Properties of SWNTs.</b> <b>.....</b>	<b>14</b>
<b>1.2.5 Applications of Noncovalently Modified SWNTs for Chemical Sensing</b>	<b>16</b>
<b>2.0 POLYMERIC REARRANGEMENT ON SINGLE-WALLED CARBON</b> <b>NANOTUBES FOR METAL ION DETECTION.....</b>	<b>17</b>
<b>2.1 CHAPTER PREFACE .....</b>	<b>17</b>
<b>2.2 INTRODUCTION .....</b>	<b>18</b>
<b>2.3 EXPERIMENTAL.....</b>	<b>20</b>

<b>2.4</b>	<b>RESULTS AND DISCUSSION .....</b>	<b>23</b>
2.4.1	Synthesis and Characterization .....	23
2.4.2	Metal Ion Coordination.....	26
2.4.3	Interactions of PAM with SWNTs.....	29
2.4.4	Co <sup>2+</sup> Detection on SWNT Devices.....	33
2.4.5	Transduction Mechanism for Co <sup>2+</sup> Sensing.....	36
2.4.6	Cu <sup>2+</sup> Detection on PAM/SWNT Devices .....	40
<b>2.5</b>	<b>CONCLUSION .....</b>	<b>41</b>
<b>2.6</b>	<b>SUPPORTING INFORMATION .....</b>	<b>41</b>
<b>3.0</b>	<b>SOLID STATE PH SENSORS BASED ON CARBON NANOTUBES.....</b>	<b>59</b>
3.1	CHAPTER PREFACE.....	59
3.2	INTRODUCTION .....	60
3.3	EXPERIMENTAL.....	62
3.4	RESULTS AND DISCUSSION .....	65
<b>4.0</b>	<b>BIOSENSORS BASED ON CARBON NANOTUBES FOR METAL ION DETECITION.....</b>	<b>79</b>
4.1	INTRODUCTION .....	79
4.1.1	Carbon nanotubes as biosensors.....	79
4.1.2	Interactions between Carbon Nanotubes and Protein Molecules .....	83
4.1.3	NTFET fabrication .....	83
<b>4.2</b>	<b>CALMODULIN MODIFIED SWNTS FOR DETECTION OF CALCIUM IONS .....</b>	<b>85</b>
4.2.1	Introduction.....	85

4.2.2	Experimental .....	87
4.2.3	Result and Discussion .....	87
4.2.4	Conclusion .....	97
4.3	<b>BACTERIOFERRITIN MODIFIED SWNTS FOR DETECTION OF IRON IONS</b> .....	<b>98</b>
4.3.1	Introduction.....	98
4.3.2	Experimental .....	101
4.3.3	Results and Discussion.....	101
4.3.4	Conclusion .....	119
	<b>BIBLIOGRAPHY</b> .....	<b>120</b>

## **LIST OF TABLES**

Table 3-1. Summary of the effect of the number of CV cycle on the sensitivity of the devices.. 78

## LIST OF FIGURES

Figure 1-1. Carbon nanotube (CNT) structure.....	6
Figure 1-2. Formation of different type of carbon nanotubes.....	7
Figure 1-3. Density of states (DOS) of SWNTs contributing to the near-IR and UV-visible absorption.....	8
Figure 1-4. Scanning Electron Microscopy (SEM) images of the SWNT networks.....	11
Figure 1-5. The UV-Vis-NIR optical absorption spectra of a SWNT film on quartz. ....	12
Figure 1-6. Density of states (DOS) of metallic and semiconducting SWNTs of two molecular interactions.....	15
Figure 2-1. Optical dependence of PAM and MAC to $\text{Co}^{2+}$ ions.....	28
Figure 2-2. Optical and electrical dependence of PAM/SWNT and MAC/SWNT to $\text{Co}^{2+}$ ions..	35
Figure 2-3. Optical and electrical response of bare SWNT to $\text{Co}^{2+}$ ions.....	38
Figure 2-4. Schematic representation of the proposed mechanism of detection. ....	39
Figure 3-1. Optical measurements of PAA/o-SWNT film. ....	69
Figure 3-2. Device fabrication and characterization of PAA/o-SWNT.....	73
Figure 3-3. Electrical measurements of PAA/o-CNT.....	74
Figure 3-4. Additional/Control experiments for PAA/SWNT.....	75
Figure 4-1. Schematic representation of a back-gate nanotube field-effect transistor (NTFET) device.....	81

Figure 4-2. Schematic illustration of detection in liquid with functionalized NTFET by using liquid gate configuration.....	82
Figure 4-3. Structure of apo CaM and Ca <sup>2+</sup> -CaM.....	86
Figure 4-4. Electronic detection of Ca <sup>2+</sup> -CaM interactions on NTFET device.....	89
Figure 4-5. Sensitivity study with Zn <sup>2+</sup> as control on CaM-modified NTFET devices.....	90
Figure 4-6. Real-time detection of the binding of Ca <sup>2+</sup> to a CaM/o-SWNT device.....	93
Figure 4-7. Control experiment on a pristine SWNT device.....	94
Figure 4-8. Control experiment on a bare o-SWNT device.....	95
Figure 4-9. AFM images of apo-CaM/SWNTs and Ca <sup>2+</sup> -CaM/SWNTs.....	96
Figure 4-10. Structure of <i>Pseudomonas aeruginosa</i> bacterioferritin B (Pa BfrB) and its ferroxidase center upon complexation of Fe <sup>2+</sup> ions.....	100
Figure 4-11. Electronic detection of Fe <sup>2+</sup> ions on Pa BfrB/ P3-SWNTFET device.....	104
Figure 4-12. Electronic detection of metal ions interactions with bare P3-SWNTFETs.....	105
Figure 4-13. Electronic detection of competition between Fe <sup>2+</sup> (first added) and Zn <sup>2+</sup> (next added) on Pa BfrB/o-SWNTFET devices.....	108
Figure 4-14. Electronic detection of competition between Zn <sup>2+</sup> (first added) and Fe <sup>2+</sup> (next added) on Pa BfrB/o-SWNTFET devices.....	109
Figure 4-15. Electronic detection of on Pa BfrB/P3-SWNTFET devices in 1h incubation.....	110
Figure 4-16. Electronic detection of on Pa BfrB/P3-SWNTFET devices in 6h incubation with first treatment with Fe <sup>2+</sup> then Zn <sup>2+</sup> next.....	111
Figure 4-17. Electronic detection of on Pa BfrB/P3-SWNTFET devices in 6h incubation with first treatment with Zn <sup>2+</sup> then Fe <sup>2+</sup> next.....	112
Figure 4-18. Control experimental on Pa BfrB/pristine-SWNT device.....	113

Figure 4-19. Conductance measurement on Pa BfrB/o-SWNT device .....	115
Figure 4-20. AFM images of bare P3-SWNTs before and after Fe <sup>2+</sup> addition.....	117
Figure 4-21. AFM images of Pa BfrB/P3-SWNTs before and after Fe <sup>2+</sup> addition.....	118
FigureS 2-1. <sup>1</sup> H-NMR (CDCl <sub>3</sub> , 300 MHz) of PAM polymer.....	48
FigureS 2-2. FTIR (NaCl) spectra of PAM polymer .....	49
FigureS 2-3. UV-vis absorption spectra of PAM and its constituent monomers .....	50
FigureS 2-4. Normalized absorption and emission spectra of PAM polymer (in THF).....	51
FigureS 2-5. Optical reponse of PAM polymer in acidic and basic vapors.....	52
FigureS 2-6. AFM images of bare SWNT, MAC/SWNT and PAM/SWNT.....	53
FigureS 2-7. UV-vis-NIR absorption spectra of SWNT, PAM, and PAM/SWNT .....	54
FigureS 2-8. UV-vis-NIR absorption spectra of SWNT and MAC/SWNT .....	55
FigureS 2-9. UV-Vis titration of PAM polymer with CuCl <sub>2</sub> .....	56
FigureS 2-10. Opitcal and electrial dependence of PAM/SWNTs to Cu <sup>2+</sup> ions.....	57
FigureS 2-11. Electrical dependence of bare SWNTs to Cu <sup>2+</sup> ions.....	58

## LIST OF SCHEMES

Scheme 2-1. Synthesis of polyazomethine (PAM) polymer and salophen macrocycle (MAC). .	25
Scheme 3-1. Sythesis of poly(1-amino anthracene ) (PAA). .....	66
Scheme 3-2. Proposed mechanism of detection pH for pAA and SWNT. ....	77
SchemeS 2-1. Synthesis of polyazomethine (PAM) and salophen macrocycle (MAC) in detail.	44

## **PREFACE**

Firstly, I would like to thank my research advisor, Professor Alexander Star for his help, inspiration, encouragement, and patience.

I would like to thank all members of the Star Group for their help and support throughout my research.

I would also like to thank all of my friends who have accompanied me and shared experiences for all of these years in Pittsburgh.

I would express my sincere gratitude towards my parents, for their endless love and support, and for never questioning why I spent such a long time for a PhD degree in a foreign country.

Finally, I thank my husband, Ming Liu, for always being by my side, loving, supporting, and believing in me, and for making each day vivid.

## **1.0 INTRODUCTION**

### **1.1 METAL ION SENSORS**

#### **1.1.1 Sensors in Nature**

Nature has evolved varieties of amazing sensory systems with specialized adaptations. Many living organisms have developed sophisticated sense organs. For example, insects have sensory hairs and antennae, which allow detection of external stimuli. Mammals also possess olfaction and gustation systems that identify a whole gamut of smells and tastes. Some bacteria excel in metal ion detection, with a regulatory network to control the levels of harmful metal ions they uptake and detoxify.<sup>1</sup>

Those extraordinary biological sensory systems continue to inspire researchers in the design of chemical sensors. Typically, chemical sensors contain two main components, a receptor and a transducer.<sup>2</sup> The receptor binds to a specific chemical analyte and transforms the chemical information into an energy change, where the sensitivity and selectivity are the result of the receptor response. Then the transducer converts this energy change into a useful analytical signal. Given view of complex natural sensors, the design of an artificial sensor should include the fabrication of a system consisting of a receptor and a transducer, and achievement of the selectivity and sensitivity of the complex system.

### 1.1.2 The Importance of Metal Ion (& pH) Sensors

Metal ions are essential for life processes; nevertheless, some metals are toxic to central metabolic pathways and metalloenzymes. The accumulation of heavy metals, such as lead, cadmium, and mercury, in living organisms can cause impairment of organ function or even death at relatively low concentrations. For example, the European Union guidelines for maximum cadmium levels in drinking water is set at 5 ppb because severe effects can be observed upon exposure to higher levels. Because of its long biological half-life of 15 to 30 years, cadmium excretion is nearly impossible, and it accumulates in the human body and especially in the kidneys, leading to irreversible dysfunction of the kidney with impaired reabsorption of proteins, glucose, or amino acids.<sup>3</sup> However, even essential metals such as zinc, iron, copper, chromium, and cobalt can cause toxic effects at elevated levels.<sup>4</sup> For example, copper is an essential requirement for a healthy body with an estimated daily intake 2-3 mg, yet an excess of copper can be harmful, and can cause gastrointestinal symptoms such as nausea, abdominal pain, and vomiting.<sup>4</sup> Cobalt plays an essential role in the metabolism of ions and formation of hemoglobin, also it is a key constituent of vitamin B<sub>12</sub>. The daily requirement for cobalt has been estimated to be only up to 40 µg. However, an excessive level of this trace element in the body may result in goiter formation and reduced thyroid activity. Exposure to cobalt increases the risk of development of cardiomyopathy.<sup>4</sup>

On the other hand, the entire metabolic process depends on delicately balanced pH levels, because pH controls the speed of biochemical reactions. Outside the acceptable range of pH, proteins can be denatured and digested, enzymes can lose their ability to function, and even death may occur.

Therefore, the determination of trace amounts of metal ions and pH levels is of great importance in many scientific fields, including medicine and environmental monitoring. Thus, development of methods for the detection and estimation of metal ions and pH values is an important goal for contemporary sensor research.

### **1.1.3 Design of Metal Ion Sensors**

State-of-the-art techniques for the determination of metal ions are carried out by instrumental analysis using atomic absorption spectroscopy (AAS), inductively coupled plasma atomic emission spectrometry (ICPAES), and inductively coupled plasma-mass spectrometry (ICP-MS).<sup>5</sup> These analytical methods are highly sensitive and selective. However, these methods are expensive to run and maintain, and they are typically limited to a laboratory. There is a need to develop sensors that are sensitive, portable and easy-to-use so that measurements can be performed in real time without taking samples back to the lab for analysis.

There is much interest in development of organic compounds for use as ion receptors in sensors. The detections of specific metal ions have been realized through the changes in redox potential,<sup>6</sup> UV-Vis absorption<sup>7</sup> or fluorescence spectra.<sup>8</sup> Here we show that electrochemical techniques such as conductometric titration using carbon nanotubes as transducing medium and modifying carbon nanotubes for ion recognition are alternative and very attractive methods for metal ion detection.

## 1.2 CARBON NANOTUBES

### 1.2.1 Physical and Electronic Structure of Carbon Nanotubes

Carbon nanotubes (CNTs) were generally considered to be first discovered by S. Iijima in 1991,<sup>9</sup> though they were actually been known earlier.<sup>10</sup> Carbon nanotubes can be visualized as a sheet of graphene rolled up into a hollow cylindrical tube (Figure 1-1a).<sup>11</sup> CNTs consist of coaxial tubes of graphene sheets are called multi-walled nanotubes (MWNT), as shown in Figure 1-1c. Each MWNT contains from two to 50 such tubes, with inner diameters from 1.5 to 15 nm and outer diameters from 2.5 to 30 nm. CNTs composed of one single graphene sheet are classified as single-walled nanotubes (SWNT), with diameters ranging from 1 to 5 nm (Figure 1-1b).<sup>9</sup>

Typically, the diameter, curvature, and electronic properties of a SWNT are uniquely defined by details of how the graphene sheet is rolled up.<sup>11</sup> A graphene sheet consists of a two-dimensional hexagonal lattice of  $sp^2$  hybridized carbon through which electronic conduction can occur *via* the  $\pi$ -conjugated electron system.<sup>12</sup> The sheet of graphene can be rolled up into a tube according to different rollup vectors which are denoted as  $(n, m)$ ,<sup>11</sup> as shown in Figure 1-2. The rollup vector can be defined as a linear combination of base vectors  $a_1$  and  $a_2$  of the basic hexagon:  $r = na_1 + ma_2$ , where  $n$  and  $m$  are integers. The values of  $n$  and  $m$  determine the chirality, which defines the nanotube types. If  $m = 0$ , the nanotubes are called “zigzag”. If  $n = m$ , the nanotubes are called “armchair.” If  $n \neq m$ , they are called “chiral.” The  $(n,m)$  indices strongly dictate the electronic structure of the SWNT.<sup>13</sup> If  $n-m$  values equal to  $3q$  or zero, where  $q$  is any integer, the SWNT is metallic, otherwise it is semiconducting. In particular, all armchair nanotubes are metallic; two-thirds of zigzag nanotubes are semiconducting and the other third are metallic.

Carbon atoms in SWNT have  $sp^2$  hybridization, and each possesses one 2p electron that can build a delocalized  $\pi$ -electron structure. Since SWNT has a diameter on the nanometer scale, the delocalized  $\pi$ -electrons undergo quantum confinement and cause quantized energy levels. The number density of states at each energy level are described by a density of states (DOS) diagram. The sharp spikes in the DOS are called van Hove singularities (VHS) and stem from electron confinement around the SWNT circumference.<sup>14</sup> The electron transitions between VHS are labeled as  $M_{11}$  for metallic SWNTs,  $S_{11}$  and  $S_{22}$  for semiconducting SWNTs (Figure 1-3). The metallic SWNTs have a finite density of electronic states at the Fermi level ( $E=0$ ), which is located between the valence band and conduction band, making them analogous to metals. The semiconducting SWNT exhibits an energy gap with zero density of states inside the gap, thus creating the optical and electrical characteristics of a semiconductor. The top of valence band for semiconducting SWNTs is partially depleted of electrons, indicating a p-type semiconductor.<sup>15</sup>

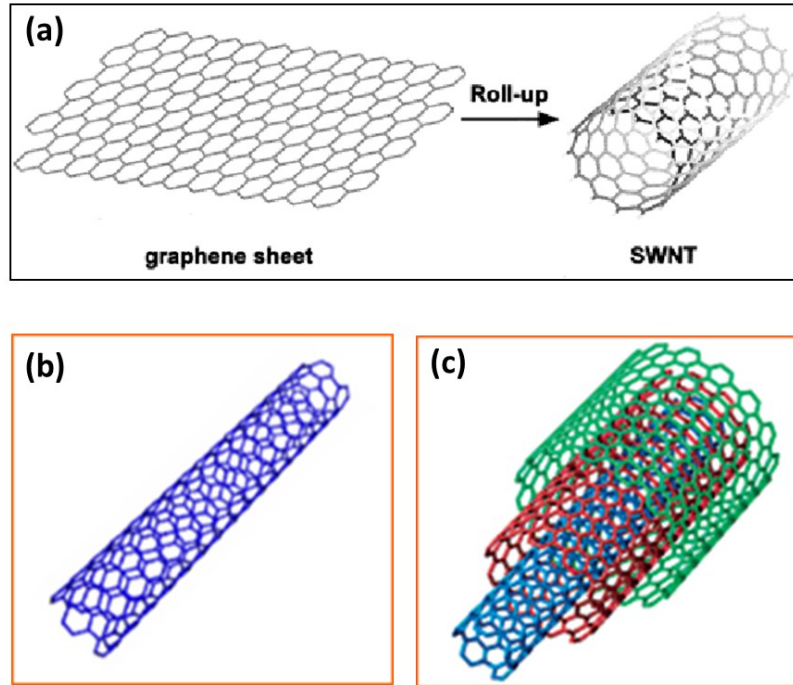


**Figure 1-1.** Carbon nanotube (CNT) structure

(a) Rolling up a graphene sheet forms a carbon nanotube (CNT). Adapted from Reference 11a. (b) The structure of SWNT consists of one cylindrical graphene sheet. (c) The structure of multi-walled nanotube (MWNT) of several nested cylinders.

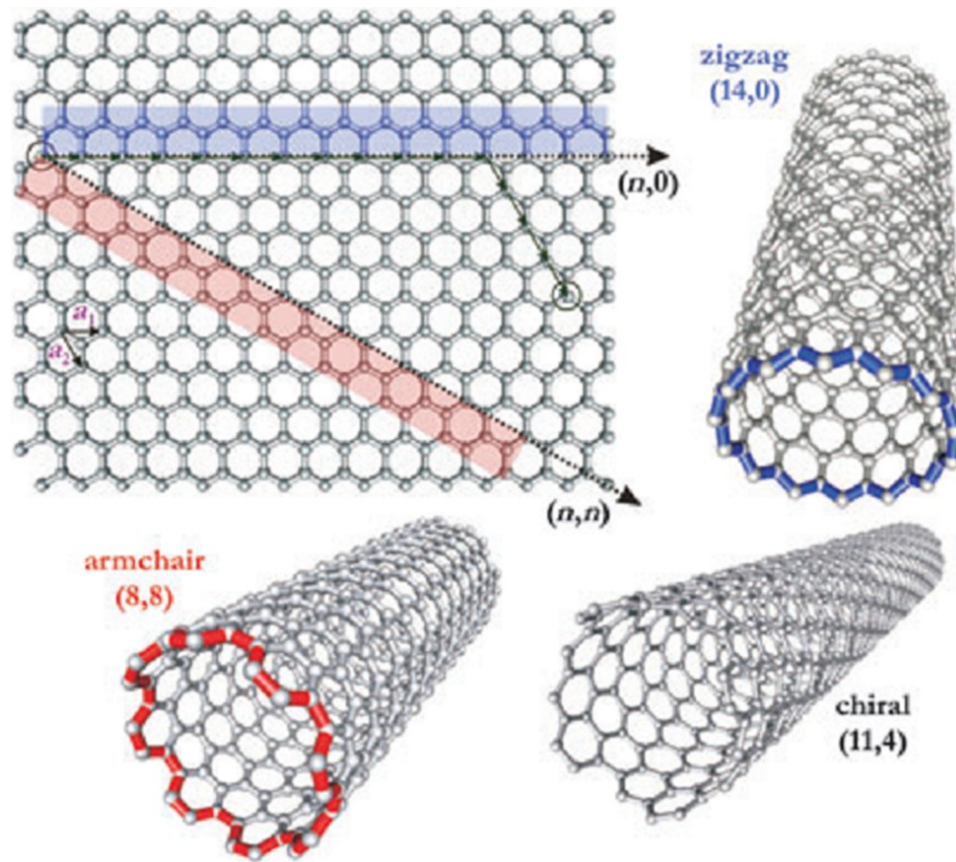


**Figure 1-2.** Formation of different type of carbon nanotubes

Schematic structure of a graphene sheet. SWNT can be formed by rolling up the sheet along lattice vector  $(n, m)$ .  $a_1$  and  $a_2$  are the unit vectors. Rolling along the different vectors leads to the different type carbon nanotubes as “armchair” ( $n = m$ ), “zigzag”( $n, 0$ ) and “chiral” ( $n \neq m$ ) SWNTs, respectively. Adapted from Reference 11b.

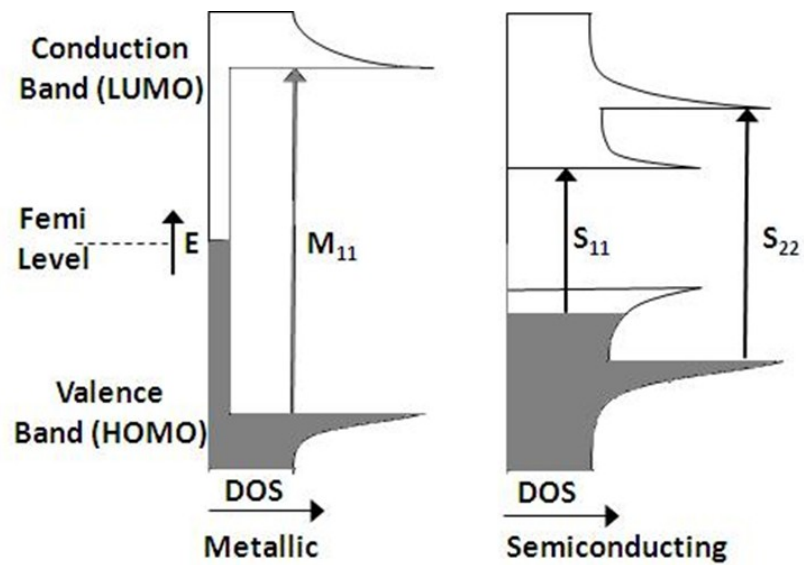


**Figure 1-3.** Density of states (DOS) of SWNTs contributing to the near-IR and UV-visible absorption  
 Semiconducting SWNT:  $S_{11}$  and  $S_{22}$  correspond to the first and second interband transitions; metallic SWNT:  $M_{11}$  is the first metallic transition.

### 1.2.2 SWNT Networks

Recently two-dimensional (2D) nanotube networks and three-dimensional (3D) nanotube films have emerged as a new class of materials.<sup>16,17,18,19</sup> The individual variations in diameter and chirality from tube to tube become obscured by averaging over a large number of tubes, resulting in uniform physical and electronic properties. Typically, percolation theory is used to study the properties of the random networks of SWNT.<sup>20,21</sup>

Percolation is the formation of long-range connectivity in random systems.<sup>22</sup> At a critical threshold the infinite connectivity first appears, called percolation threshold.<sup>21</sup> While SWNT networks are formed by tube alignments and intersections, percolation is achieved when junctions of carbon nanotubes create the infinite connectivity, forming a complete circuit through network between source and drain electrodes. Since the percolation threshold is the lowest concentration of tubes at which the circuit begins, it is dependent upon tube distribution, length and angle between tubes.

Grüner's group has illustrated percolation of SWNT networks that were fabricated by vacuum filtering of a dilute suspension of SWNTs through a porous alumina filtration membrane.<sup>20</sup> Figure 1-4 shows SEM images of three samples (a, b, and c) that have been prepared by filtering different volumes of SWNTs. The film is spatially uniform, containing randomly oriented nanotubes with no preferential direction. Notice that each line in the networks is actually a small bundle of nanotubes, due to van der Waals interactions. At high volumes of SWNTs like that shown in Figure 1-4b, the film becomes conductive and is above the percolation threshold.

The electrical conductivity through SWNT networks is strikingly different from regular conductive thin films. In SWNT networks with low interconnectivity which typically contain

only two to three connections, increasing the distance to the electrodes leads to large reduction on network conductance; while in networks with high interconnectivity, the distance to the electrodes has a negligible effect on the local conductance, which depends strongly on the number of connections in the network.<sup>23</sup>

Several methods have been reported for fabricating carbon nanotube films, such as drop casting,<sup>24</sup> spin coating,<sup>16</sup> dip-casting,<sup>25</sup> vacuum filtering on membrane,<sup>21</sup> and spray coating.<sup>26</sup> The carbon nanotube networks have been applied as thin-film transistors,<sup>16</sup> field-activated optical modulators,<sup>17</sup> strain<sup>27</sup> and field emission devices,<sup>28</sup> and transparent conductive coatings,<sup>17</sup> diodes,<sup>29</sup> field effect transistors<sup>30</sup> and chemical sensors.<sup>31, 32, 33</sup> In chemical sensors, thin films of random SWNT networks exhibited p-type semiconducting behavior and can operate as the conducting channel of the device.<sup>31, 32, 33</sup> In this case, the charge transfer between the conductive nanotube channel and the analytes appeared as the electrical signal for chemical response.

Current synthetic methods result in a mixture of semiconducting and metallic CNT varieties, thus the optical absorption of SWNT networks is actually a superposition of individual peaks from both semiconducting and metallic species of differing chirality and diameter.<sup>34</sup> The metallic and semiconducting SWNT species have absorption features associated with transitions between matching van Hove singularities in conduction and valence bands. The semiconducting SWNTs have two main absorption peaks in the UV, visible, and near IR regions named as S<sub>11</sub> and S<sub>22</sub> transitions, respectively. The metallic SWNTs display an absorption peak, called M<sub>11</sub>, at shorter wavelength than transitions of semiconducting SWNTs. Figure 1-5 shows the adsorption spectra of SWNT networks that were obtained commercially from *Carbon Solutions Inc*, and were prepared by the electric arc discharge method.<sup>9</sup> Three prominent absorption bands (S<sub>11</sub>, S<sub>22</sub> and M<sub>11</sub>) clearly appear in the spectrum.

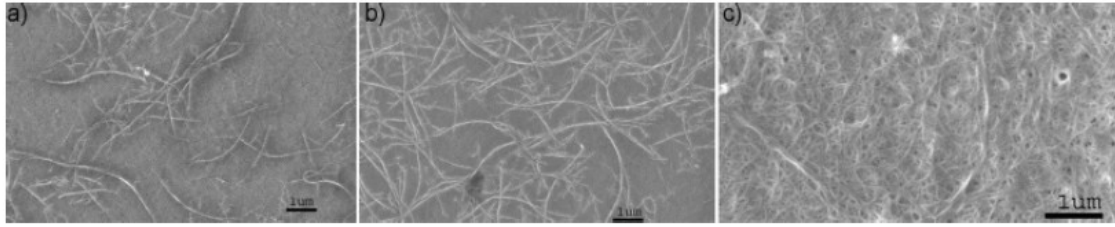


**Figure 1-4.** Scanning Electron Microscopy (SEM) images of the SWNT networks

on alumina substrates, scale bar is 1  $\mu\text{m}$ . (a) Network resulting from filtering 7 mL of SWNT solution through the membrane. The filter pores are not visible in the scale shown. The network is near the percolation threshold and has few or no percolative paths through the sample. (b) 10 mL of SWNT solution for this sample. The network is above the percolation threshold and has several parallel pathways, allowing electrical conduction across the film. (c) Film resulting from 400 mL of solution. Film is several layers thick. Adapted from Reference 20.

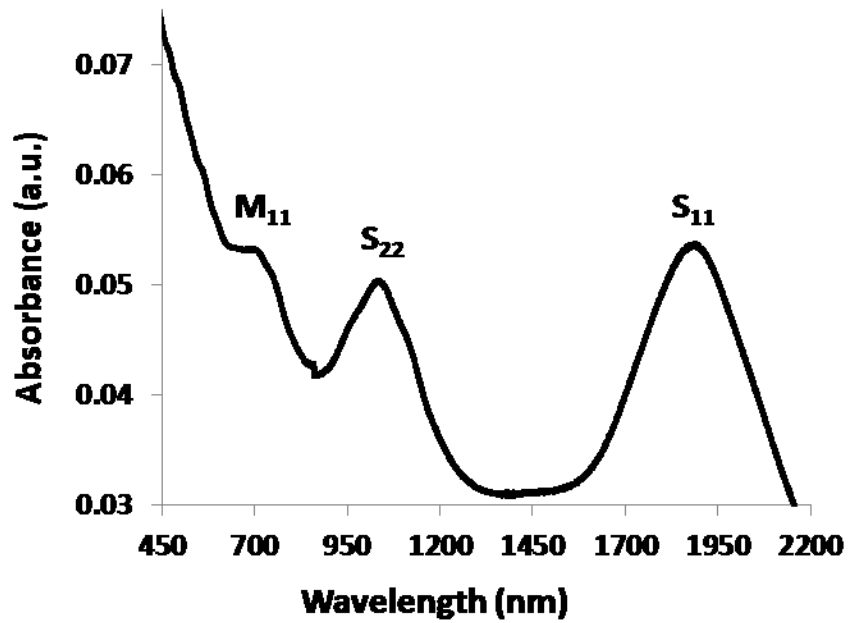


**Figure 1-5.** The UV-Vis-NIR optical absorption spectra of a SWNT film on quartz

Each absorption band,  $S_{11}$ ,  $S_{22}$  and  $M_{11}$ , is actually a superposition of the individual absorption peaks from many SWNTs of varying chirality and diameter.

### 1.2.3 Noncovalent Chemical Functionalization of SWNTs

Noncovalent functionalization approaches have been applied to chemically modified SWNTs for chemical and biological sensors.<sup>32,35</sup> Unlike covalent functionalization that unavoidably results in a disruption of  $\pi$ -electron conjugated structure of SWNTs, noncovalent modification does not change SWNT properties. There are four commonly mentioned types of noncovalent interactions: hydrogen bonds, ionic bonds, van der Waals forces, and hydrophobic interactions. In the latter types, various aromatic compounds are known to interact strongly with graphitic sidewalls of SWNTs through effective  $\pi$ - $\pi$  stacking.<sup>36,37</sup> These interactions improve the solubilization of SWNTs in aromatic solvents<sup>38</sup> and solutions of polymers.<sup>39</sup>

Moreover, the noncovalent interactions of SWNT with electron-donating or electron-withdrawing molecules can influence the spectroscopic and electronic behavior of SWNTs. For p-type SWNTs, the valence band are partially depleted,<sup>15</sup> and noncovalent interactions of SWNTs with absorbing molecule will induce charge transfer into or out of the top of valence band of SWNTs. Typically, the relative energy position of molecular orbitals (MOs) toward valence band (or LUMO) of semiconducting SWNT can lead to the shift of Fermi level (Figure 1-6). As a result, the interactions alter the electronic density of semiconducting SWNT valence band, which will appear as spectroscopic and electronic changes of SWNT films.<sup>40,41</sup> In contrast, covalent chemical modification of SWNTs destroys their aromaticity, eventually resulting in the loss of any spectral features.<sup>38</sup>

#### 1.2.4 Correlation between Spectroscopic and Electrical Properties of SWNTs

Whenever strong electron donating or accepting molecules, such as  $\text{NO}_2$  or  $\text{NH}_3$ , interact with the p-type semiconducting SWNTs, there is a significant change in density of the charge carriers in the semiconductor, holes in this case, that causes changes in the spectroscopic and electrical properties of SWNTs.<sup>42</sup> As shown in Figure 1-6, an electron donor has a full MO with higher energy level near or above the SWNT valence band, thus the adsorption of these molecules on SWNT networks will render the electron transfer to nanotube valence band. As a result, electron donation will result in the increase of the electron density of SWNT valence band, thus leading to increased  $S_{11}$  band absorbance of the SWNT networks. Meanwhile, the band gap will be reduced, leading to a red shift of the  $S_{11}$  absorption band to lower energy wavelength. Moreover, the electron-hole recombination caused by electron donation will also serve to decrease the film conductance of SWNT networks. Alternatively, electron accepting species have an unfilled MO with energy level lower than the top of the SWNT valence band, so the adsorption will cause a decrease in electron density of the SWNT valence band. A decrease in electron density will lead to reduced  $S_{11}$  band intensity and to a blue-shift in  $S_{11}$  band as a result of an increased band gap. Additionally, increased concentrations of hole carriers for p-type SWNTs will serve to increase the nanotube film conductance.

Furthermore, the molecular adsorption on SWNTs can cause a change in the local dielectric environment of SWNTs, leading to changes in both  $S_{11}$  and  $S_{22}$  absorption band intensities even no charge transfer is expected.<sup>41</sup> In this case, the  $S_{11}/S_{22}$  ratio in the SWNT optical spectra (Figure 1-5) can be applied to investigate the electron transfer: a higher  $S_{11}/S_{22}$  ratio than unmodified SWNTs will indicate the electron donation, and a smaller  $S_{11}/S_{22}$  ratio could be a result of electron withdrawal.

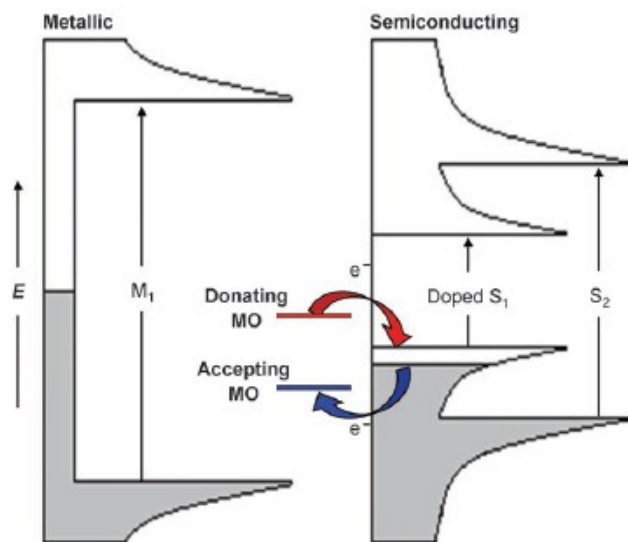


**Figure 1-6.** Density of states (DOS) of metallic and semiconducting SWNTs of two molecular interactions. Interaction with an electron-donating molecular orbital (MO) that resides at a higher energy than semiconducting SWNT valence band and interaction with an electron-accepting MO that is partially vacant and resides slightly lower in energy than SWNT valence band.

### 1.2.5 Applications of Noncovalently Modified SWNTs for Chemical Sensing

Specifically, the changes in the absorption intensity of the first semiconducting electron transition ( $S_{11}$ ) as well as the electrical conductance of the SWNT stem from charge transfer and chemical doping effects by various molecules. This behavior builds the basis of applications of SWNTs as electrical chemical sensors. However, sensors based on bare SWNTs lack selectivity toward analytes. To overcome the challenges, noncovalent functionalization of the SWNT can make SWNT sensors more selective while maintaining their ultrasensitivity.<sup>43, 44</sup> This functionalization scheme can help to add a detection layer on surface of SWNT without interrupting its  $sp^2$  hybridized structure and has been proven effective in developing sensors.<sup>45,46,32</sup> Therefore, noncovalent functionalization of SWNTs with metal ion/pH selective ligands should allow for development of highly sensitive metal ion/pH sensors.

The following chapters serve to demonstrate metal ion/pH detection based on SWNTs, where the changes in spectroscopic and electrical properties of the SWNT device upon chemical sensing could arise from charge transfer between the ligand layer and the SWNT. Moreover, the presence of ligand layer has been proven to amplify the electrical signals of SWNT devices, offering a platform to investigate the mechanism between the interactions.

## 2.0 POLYMERIC REARRANGEMENT ON SINGLE-WALLED CARBON NANOTUBES FOR METAL ION DETECTION

The results presented in this chapter will be submitted for publication in the near future.

**List of Authors:** Pingping Gou, Ian Matthew Feigel, and Alexander Star.

### 2.1 CHAPTER PREFACE

The aim of this work was to develop SWNT-based sensor systems, in which the sensing responses stem from varying conformational changes of molecular ligands adsorbed on sidewalls of SWNTs. We compared two types of molecular ligands for noncovalent modification of SWNTs; both ligands can chelate transition metal ions as well as exhibit  $\pi$ - $\pi$  stacking interactions with carbon nanotubes. One ligand is rigid triangular-shaped conformation of salophenyl macrocycle (Mac), while a linear polyazomethine (PAM) polymer can experience a large conformational change upon complexation with metal ions. The differences in ligands' conformational behavior led to the different performance of the sensory systems. The combination of optical spectroscopy and electrical measurements was utilized to study the detection of metal ions, as well as to gain an understanding of the mechanistic aspects of SWNT sensor response.

## 2.2 INTRODUCTION

Single-walled carbon nanotubes (SWNT) can be either semi-conducting or metallic, and they can be ultrasensitive sensors because of their composition of only surface atoms. Additionally, their high aspect ratio allows for facile integration into conventional micrometer sized electronic circuitry. Such features make SWNTs highly sensitive to charge transfer and chemical doping effects by various molecules. Whenever strong electron withdrawing or donating molecules, such as NO<sub>2</sub> or NH<sub>3</sub>, interact with the p-type semiconducting SWNTs, there is a significant change in density of the charge carriers in the semiconductor, holes in this case, that causes observable changes in the optical and electronic properties of SWNTs.<sup>42</sup> Specifically, there is a significant change in the absorption intensity of the first semiconducting electron transition (S<sub>11</sub>) as well as the electrical conductance of the SWNT. This behavior forms the basis of applications of SWNTs as electrical chemical sensors. However, sensors based on bare SWNTs lack selectivity toward analytes, as even contact with an inert gas will cause signal changes in SWNTs. To overcome this challenge, functionalization schemes have been developed to make SWNT sensors more selective while retaining their ultrasensitivity.<sup>43, 44</sup> Noncovalent functionalization on the SWNT can help to add a detection layer without interrupting its sp<sup>2</sup> hybridized structure and has proven effective in developing sensors.<sup>45,46,32</sup> Noncovalent functionalization is a type of surface functionality where two species are held together through van der Waals forces,  $\pi$ - $\pi$  stacking in this case. Therefore, functionalization of SWNTs with metal ion selective ligands should allow for the creation of an ultrasensitive metal ion detection device. Changes in the electronic properties of the SWNT device upon metal ion coordination could arise from charge transfer between the ligand and the SWNT or from conformational changes of the ligand (disruption of the  $\pi$ - $\pi$  stacking interactions).

A rigid, shape-persistent macrocycle, salophen macrocycle (MAC), has been reported for its coordination with metal ions. Interestingly, by slightly adjusting the chemical synthesis, we designed and synthesized a chain version of MAC, termed polyazomethine (PAM) which offers the same chelating properties while having significant morphology differences, specifically it is one-dimensional and flexible. The  $\pi$  conjugated backbone of these molecules make them ideal targets for studying with carbon nanotube (CNT) devices as they offer a great advantage in noncovalent functionalization.

PAM and MAC were both synthesized and characterized as necessary. Optical spectroscopy titrations were performed on the ligand species in order to determine the number of metal ions that coordinate with each ligand. MAC was found to coordinate three  $\text{Co}^{2+}$  ions, agreeing well with literature, while PAM was found to coordinate only 0.3  $\text{Co}^{2+}$  ions per repeating unit (there are 3 repeating units in MAC). This suggests that several PAM repeating units are required to coordinate only one metal ion in either inter- or intra-molecular fashion, and therefore a conformational change of the polymer occurs upon introduction to metal ions. This hypothesis is supported by the observation of a distinct change in the color of PAM upon addition of  $\text{Co}^{2+}$  ions, revealing rearrangement of the polymer matrix. In order to continue studying the difference between PAM and MAC, a SWNT network device was fabricated onto a quartz plate, which allows for simultaneous optical and electrical measurements. Distinct changes in the  $S_{11}$  electronic transition of SWNTs upon ligand modification is observed for both ligand devices suggesting strong noncovalent functionalization. The optical response of the ligand functionalized SWNTs was performed using UV-vis-NIR spectroscopy. A much larger change in the  $S_{11}$  transition is observed for a PAM/SWNT film when exposed to  $\text{Co}^{2+}$  ions, as compared to the MAC/SWNT complex. Additionally, the conductance change of the

PAM/SWNT film was greater than that of MAC/SWNT and offers the additional advantage of a greater dynamic range. The signal changes in MAC are comparable to that of bare SWNTs, signifying that the rigid macrocycle does not offer any advantages, such as charge transfer into the SWNT, upon metal ion coordination. It is proposed that rearrangement of PAM, due to its flexible nature, on the nanotube network results in a new type of transduction mode and thus enhances the signals of the SWNT device.

### 2.3 EXPERIMENTAL

**Materials and Instrumentation.** SWNTs (prepared by arc discharge technique)<sup>47</sup> were purchased from Carbon Solutions, Inc. (P2-SWNT). Chemicals were purchased from Sigma Aldrich and used as received. Solvents were dried, distilled, and stored under argon. All reactions were carried out in a N<sub>2</sub> atmosphere unless otherwise stated. 3, 6-diforymlcatechol,<sup>48</sup> 1,2-dioctyloxy-4,5-phenylenediamine,<sup>49</sup> and 1,4-dioctyloxy-2,5-phenylenediamine were synthesized following published procedure (see Supporting Information for details).

FT-IR spectra were recorded as either thin films on NaCl plates or as KBr pellets on an Avatar 380 Nicolet FT-IR spectrometer. Proton nuclear magnetic resonance (<sup>1</sup>H-NMR) spectra were recorded on a Bruker DPX 300 NMR spectrometer (300 MHz) at 25 °C. Deuterated solvent was used as the lock and the residual solvent was used as an internal standard. Molecular weights of polymers were determined by using a Waters Gel Permeation Chromatography system equipped with a Water 510 HPLC pump, phenogel columns, and a Waters 410 Differential Refractometer at a flow rate of 0.4 mL/min. All molecular weights were measured against polystyrene standards in THF.

UV-vis-NIR spectroscopic measurements were recorded on a PerkinElmer Lambda 900 spectrophotometer. Additionally the SWNT network conductance versus time,  $G(t)$ , was monitored by applying a bias voltage of 50 mV through the network and measuring the resultant current using a Keithley model 2400 Source Meter interfaced to LabView software.

**Synthesis of Salophen Macrocycle (MAC).**<sup>50</sup> MAC was synthesized following published procedure.<sup>50</sup> 1,2-dioctyloxy-4,5-phenylenediamine (1.9 g, 6.0 mmol) was dissolved in 60 mL of 1:1 degassed  $\text{CHCl}_3$  : MeCN under a  $\text{N}_2$  environment. 3,6-diformylcatechol (1.0 g, 6mmol) was added, changing the appearance of the solution from colorless to deep red. After heating at 90 °C while refluxing for 2 h, the solution was cooled to room temperature, yielding red needles of salophen macrocycle, which was isolated on a funnel, washed with chilled MeCN, and dried under vacuum.

**Synthesis of polyazomethine (PAM) polymer.** Freshly prepared 1,4-dioctyloxy-2,5-phenylenediamine (109 mg, 0.3mmol) was added to a solution of 3,6-diformylcatechol (50 mg, 0.30 mmol), LiCl (55 mg, 1.2 mmol) and 4-Dimethylaminopyridine (DMAP) (3.7 mg, 0.03 mmol) in a mixture of 3 mL of hexamethylphosphoramide (HMPA) and 3mL of anhydrous methylpyrrolidone (NMP)). The reaction mixture (deep orange red color) was stirred for 48 hours under ambient conditions. 23  $\mu\text{L}$  (0.15 mmol) of t-butylaniline was added to the solution and the resultant mixture was stirred for additional 6 hours. The resulting precipitate (polymer) was extracted from MeOH (200 mL), and washed thoroughly with MeOH and distilled water. PAM polymer was further purified by washing with MeOH in a Soxhlet extractor for 12 h to afford a brown orange solid (83 mg, 56%).  $\nu_{\text{C=N}}$ , 1614 $\text{cm}^{-1}$ ;  $\nu_{\text{O-C-O}}$  1215  $\text{cm}^{-1}$ ;  $^1\text{H-NMR}$  ( $\text{CDCl}_3$ )  $\delta$  12.71 (2H, s, OH), 8.63 (2H, s, CH=N), 7.48 (4H, d, aromatic CH), 4.03 (4H, m,  $\text{OCH}_2$ ), 1.89 (m,  $\text{CH}_2$ ), 1.35 (m,  $\text{CH}_2$ ), 0.88 (t,  $^3J_{\text{HH}} = 6.3$  Hz,  $\text{CH}_3$ ). The molecular weight ( $M_n = 24,600$

g/mol) [2,700] and polydispersity index (PDI = 1.378) [1.304] of polymer were determined in THF by Gel Permeation Chromatography (GPC) against polystyrene standard in THF. Anal. Calc'd for  $(C_{30}H_{42}N_2O_4)_n$ : C, 72.84; H, 8.56; N, 5.66. Found: C, 73.08; H, 8.60; N, 5.71.

**Device Fabrication.** Nanotube devices were fabricated as described previously.<sup>31</sup> Briefly, SWNTs were suspended in DMF using ultrasonication and then spraycast onto heated 1" x 1" fused quartz ( $SiO_2$ ) plates (0.0625 in thick; Quartz Scientific; reported specific resistance of  $10 \times 10^{18} \Omega \text{ cm}^{-3}$  at 20 °C) using a commercial air gun (Iwata, Inc.). The plates, which served as the device substrates, were cleaned prior to SWNT deposition with acetone, and then subsequently rinsed with water and dried under compressed air. Electrodes were created by placing Al tape and Ag paint (SPI supplies) on top of the SWNT network leaving a spacing of 1.5 cm to create an unobstructed optical window. One drop of PAM (10  $\mu\text{M}$ ) in THF was subsequently deposited onto the SWNT network. For comparison of PAM to its corresponding macrocycle, MAC ( $1.4 \times 10^{-4} \text{ M}$ ) was dropcast onto the network instead of PAM.

**Metal Ion Interactions.** Cobalt chloride ( $CoCl_2$ ) solutions in MeCN were prepared at eight different concentrations:  $1 \times 10^{-12} \text{ M}$  to  $1 \times 10^{-2} \text{ M}$ . A 10  $\mu\text{L}$  drop of the  $CoCl_2$  solution was added to the center of the SWNT/PAM film and allowed to evaporate in air. UV-vis-NIR absorption spectroscopy and electrical conductance measurements were collected for 1000 seconds. The evaporation of MeCN drop typically takes a few seconds and the signals were steady within 1000 seconds.

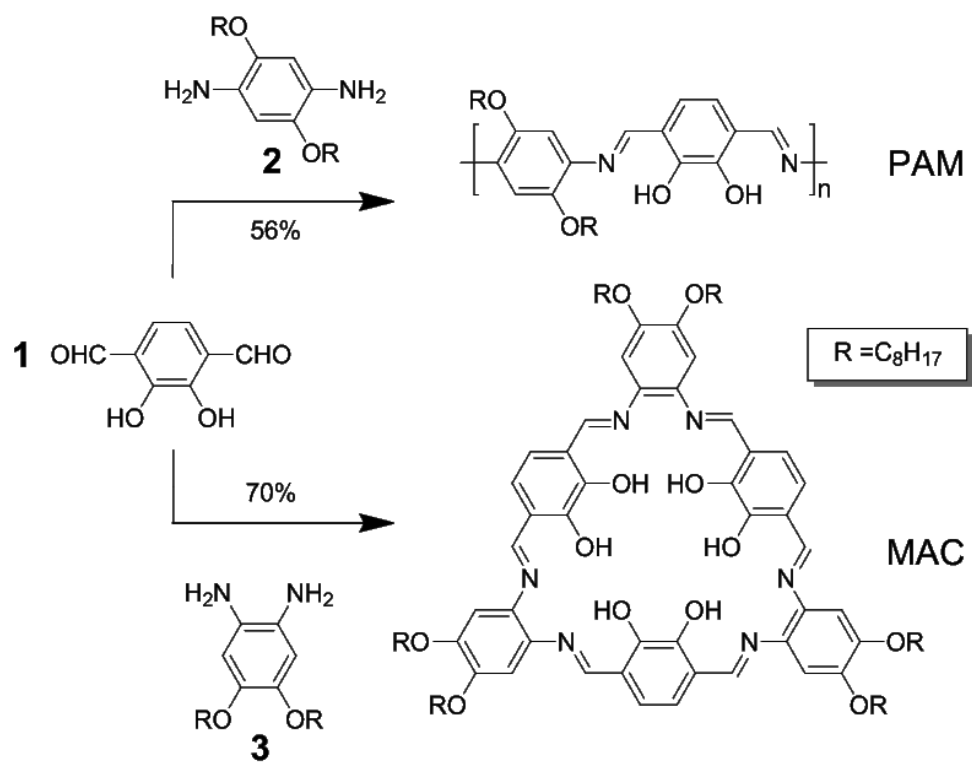
## 2.4 RESULTS AND DISCUSSION

### 2.4.1 Synthesis and Characterization

Salophen macrocycle (MAC) was prepared (Scheme 2-1) by polycondensation of 3,6-diformylcatechol (**1**) and 1,2-dioctyloxy-4,5-phenylenediamine (**3**) following the reported procedure.<sup>50</sup> In order to compare the rigid macrocycle with a flexible molecule, polyazomethine (PAM) polymer was synthesized from the same dialdehyde **3** with 1,4-dioctyloxy-2,5-phenylenediamine (**2**) as the diamine. PAM polymer, a repeating chain version of MAC, was obtained as a brown-red powder that is miscible in many organic solvents such as THF, CHCl<sub>3</sub>, and CH<sub>2</sub>Cl<sub>2</sub>. Its good solubility can be partially attributed to the presence of octyloxy groups incorporated in the polymer backbone. The chemical structure of PAM was confirmed by <sup>1</sup>H NMR spectroscopy (Supporting Information Figure S2-1), FTIR spectroscopy (S2-2), and elemental analysis. The <sup>1</sup>H NMR spectrum was in good agreement with the polymeric structure. Additionally, the presence of a major signal at  $\delta = 8.77$  ppm for the azomethine protons suggests the predominance of one isomer, which presumably is the thermodynamically more stable *anti* isomer. The broader signal at  $\delta 12.7$  ppm corresponds to hydroxyl protons, the integration of O-H proton gives a number less than the expected number of protons on the hydroxyl groups, which is due to the fact that protons on heteroatoms such as oxygen can undergo rapid proton-deuterium exchange with water. The end groups of the polymer such as -NH<sub>2</sub> and -CHO are hardly seen on the spectrum, indicating a degree of polymerization higher than ten. The FTIR spectrum showed a strong absorption band at 1614 cm<sup>-1</sup> assigned to the imine (C=N) stretching. This band was shifted to a higher wavenumber compared to other PAM polymers, suggesting strong intramolecular hydrogen bonding between the imine nitrogen and phenol hydrogen (O-

H $\cdots$ N=C) in the *ortho*-position of the azomethine aromatic ring. Additionally, elemental analysis was consistent with the chemical composition of the polymer, and Gel Permeation Chromatography (GPC) analysis indicated that there are 68 average repeating units on the polymer main chain ( $M_n = 24,600$  g/mol and PDI = 1.4).

Furthermore, UV-vis absorption spectroscopy was utilized to look at electron transitions in PAM both in solution and as a solid film (Figure S2-3). PAM exhibits a main band centered at 492 nm and a weaker band around 346 nm which are associated with the  $\pi$ - $\pi^*$  and n- $\pi^*$  transitions in the polymer backbone, respectively. The main absorption band of PAM is significantly red shifted as compared to both starting monomers; 1,4-dioctyloxy-2,5-phenylenediamine ( $\lambda_{\max} = 307$  nm) and 3,6-diformylcatechol ( $\lambda_{\max} = 394$  nm). This shift can be attributed to the increased degree of  $\pi$  conjugation in the polymer backbone compared to the reactants. When PAM is deposited as a thin film, the absorption band of PAM film is broadened and further red shifted ( $\sim 80$  nm). This is typical for polymers when in solid form due to an increased planarity induced by interchain stacking.<sup>51</sup> The HOMO-LUMO difference of PAM can be estimated to be ca. 2.1 eV, determined from the intercept of the normalized absorption and emission spectra (Figure S2-4). However, this energy gap is somewhat smaller than that of prototypical PAM polymer without phenol groups, reported previously to be 2.4 eV.<sup>52</sup> The difference in the band gap values suggests that intramolecular hydrogen bonding (OH $\cdots$ N) stabilizes the backbone of the molecule by reducing the rotational freedom of the azomethine ring.



**Scheme 2-1.** Synthesis of polyazomethine (PAM) polymer and salophen macrocycle (MAC)

## 2.4.2 Metal Ion Coordination

In order to elucidate the mechanism of metal ion coordination within the ligand molecules, optical titrations were performed in order to determine the number of metal ions that complex with the ligands. It has been previously demonstrated that the salophen macrocycle can form a stable complex with three transition metal ions, and its triangular conformation remains largely unchanged after the complexation.<sup>53</sup> On the other hand, PAM has a more flexible backbone which can undergo conformational changes and can chelate metal ions using different chains (molecules). Such interchain coordination of metal ions should result in a cross-linked polymer network, which in turn should result in a change in optoelectronic properties of the polymer because of improved orbital overlap of  $\pi$ -conjugated chains.<sup>54</sup> The assumed complexation modes were investigated by UV-vis spectroscopy and photoluminescence (PL) emission spectroscopy (Figure 2-1). Addition of  $\text{Co}^{2+}$  ions to a PAM solution in THF ( $10^{-4}$  M) lead to  $\sim 140$  nm red-shift of the polymer main peak, indicating that the resulting polymer backbone has a greater  $\pi$ -electron delocalization and a reduced band gap (Figure 2-1A). Assembly of  $\pi$ -conjugated PAM polymer chains through the metal coordination is assumed to be responsible for the observed change in the optoelectronic properties. As the concentration of  $\text{Co}^{2+}$  ions increases the UV-vis characteristic curve changes until finally becoming saturated. The inset of Figure 2-1A displays the nonlinear dependence of the absorption intensity on the concentration of  $\text{Co}^{2+}$  at  $\lambda_{\text{max}}$  (631 nm) with saturation occurring at a metal ion to PAM ratio of 0.3. These results suggest the formation of the previously discussed cross-linked polymer network upon metal complexation. Emission spectroscopy was also utilized to study metal complexation, specifically fluorescence quenching was observed with the addition of  $\text{Co}^{2+}$  ions upon PL titration (Figure 2-1B). The quenching may arise from energy transfer in inter-strand

interactions. The quenching is saturated with a metal ion to polymer unit ratio around 0.3, which is consistent with UV-vis titration. In contrast to PAM, monitoring UV-vis during metal complexation of MAC (Figure 2-1C) shows only a modest red shift (~30 nm) upon complexation. Additionally complexation stoichiometry of three cobalt ions with one MAC molecule is in good agreement with literature results.<sup>53</sup> The relatively smaller red shift of can be attributed to the rigid structure remaining the same after complexation, compared to obvious conformational change of PAM polymer.

The observed change in the UV-vis absorption spectra of PAM upon complexation with transition metals can be applied toward the design of fluorescent and colorimetric sensors. While a  $10^{-4}$  M  $\text{Co}^{2+}$  solution has a weak blue color hardly detected by the naked eye, however, when added to the deep red PAM solution, the entire mixture becomes a very strong blue color. To study this effect spectroscopically, a polymer film was prepared by spin coating a solution of PAM in  $\text{CHCl}_3$  onto a quartz plate. Dropcasting of 10  $\mu\text{L}$  of  $10^{-3}$  M  $\text{Co}^{2+}$  solution in MeCN onto the polymer film led to 100 nm red shift in UV-vis absorption of the film and an obvious color change from red to blue (Figure 2-1D). The color and maximum wavelength both recover upon treatment with MeCN/ethylenediamine (9:1). Ethylenediamine strongly chelates  $\text{Co}^{2+}$  ions breaking the cross-linked network. The decrease in absorbance of the film after treatment arises from some film dissolution in MeCN. The inset of Figure 2-1D is a photograph of the PAM film after addition of  $\text{Co}^{2+}$  ions. The proposed structures of the ligands complexed with  $\text{Co}^{2+}$  ions is given in Figure 2-1E. The three binding sites of MAC are open and complexation does not affect the structure or orientation of the ligand, however in order for PAM to fully chelate the metal ions numerous chains are necessary.

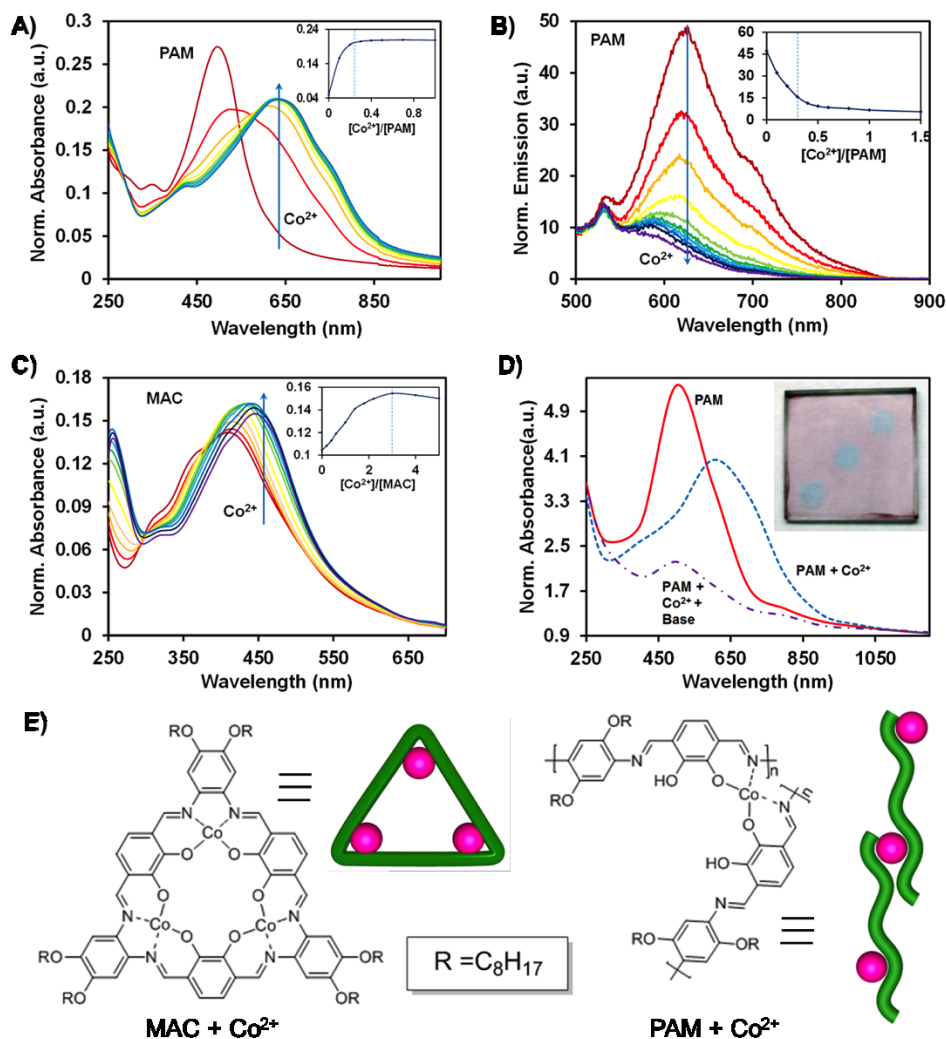


**Figure 2-1.** Optical dependence of PAM and MAC to  $\text{Co}^{2+}$  ions

A) UV-vis titration of PAM polymer with  $\text{CoCl}_2$ . The inset plots the intensity of absorption at 630 nm versus the ratio of  $\text{Co}^{2+}$  ions to polymeric units, and reveals that ca. 0.33  $\text{Co}^{2+}$  ions complex with each polymer repeat unit. B) Photoluminescence (PL) emission spectra (500 nm excitation) upon titration of PAM with  $\text{CoCl}_2$ . The inset depicts the intensity of the emission at 621 nm as a function of the ratio of  $\text{Co}^{2+}$  ions to polymeric units. C) UV-vis titration of MAC with  $\text{CoCl}_2$ . Inset: the titration curve is consistent with the presented structure of the complex with three equivalents of  $\text{Co}^{2+}$  ions per macrocycle. D) UV-vis-NIR absorption of PAM film (red), after treatment with  $\text{CoCl}_2$  ( $10^{-3}$  M in MeCN) (green) and then after dipping into MeCN: ethylenediamine (9:1) (purple) to remove  $\text{Co}^{2+}$  ions. Inset: Optical image of a PAM film with three drops of  $\text{Co}^{2+}$  ions along its diagonal distinctly showing the red to blue color change. E) Representation of MAC (left) and PAM (right) upon complexation with  $\text{Co}^{2+}$  ions.

In a control experiment, a thin film of PAM was exposed to acidic (HCl) and basic (NH<sub>3</sub>) vapors (Supporting Information Figure S2-5). Treatment of the film with acidic vapors resulted in a color change of PAM film from deep red to light blue and a red shift (35 nm) of the main peak with decreased intensity. This change is most likely due to protonation of the imine nitrogen, which disrupts the n- $\pi$  conjugation between imine nitrogen lone pair electrons and the adjacent phenylene ring. Compared to metal ion complexation, protonation had similar color change but a much smaller red shift. Treatment with basic vapors, which will deprotonate the polymer backbone, changed the film color back to red, and a 20 nm blue shift is observed in the UV-Vis absorption spectrum. The absorption maximum does not return to the original position most likely due to the loss of intramolecular hydrogen bonding from the addition of NH<sub>3</sub> vapors. It is worth mentioning that the protonation and deprotonation of the PAM thin film after the second cycle are reversible and can be repeated without significant degradation.

### **2.4.3 Interactions of PAM with SWNTs**

#### **Device Fabrication**

In order to investigate optical and electronic changes caused by noncovalent interactions between SWNT and the ligands, a sensing platform was developed. A network of SWNT was deposited onto a quartz plate to provide a transparent yet conductive transducer, in which the ligand was subsequently added (Figure 2-2A). The SWNT devices were fabricated as described previously in the literature.<sup>55</sup> A solution of SWNTs in DMF was spray cast onto quartz plates *via* a spray gun. Then electrodes were formed by applying Al metal tape on the edge of the quartz plate, and connecting them to the SWNT network with silver paint (Figure 2-2B). Subsequently either PAM or MAC was dropcast from a solution of THF onto the SWNT network. Fabrication of a

SWNT network device on a transparent surface allowed for combined spectroscopy and electrical measurements of the device.<sup>55</sup> SEM images of a typical PAM/SWNT complex prepared from PAM dropcast onto SWNT networks are shown in Figure 2-2B, depicting the morphology of PAM. The SEM images also indicate that PAM combines with the SWNT networks with noncovalent binding interactions.

### **Noncovalent interactions between ligands and SWNTs**

An insight toward the mechanism of interaction of PAM and SWNTs is related to the stabilization of SWNTs in organic solvent. Sonication of SWNTs in a THF solution containing PAM polymer resulted in a stable SWNT suspension which exhibited no precipitation over several days, while SWNT suspensions in THF alone tends to aggregate and precipitate after 24 hours. The stability of the suspension is directly related to interactions between PAM polymer and SWNTs. The hydrophobic aromatic backbone of the PAM polymer forms  $\pi$ - $\pi$  stacking interactions with SWNT sidewalls, while the octyloxy groups provide solubility for the PAM/SWNT composite in organic solvent. Similar structures such as PmPV polymers have previously been used to suspend SWNTs in organic solvents.<sup>39</sup> Comparatively, sonication of SWNTs in THF solution containing MAC resulted in a suspension with a brown red color, but SWNTs aggregated in 24 hours. This observed effect proves that MAC has weaker interactions with SWNTs than PAM polymer. Addition of  $\text{Co}^{2+}$  ions into the PAM/SWNT composite suspension resulted in a sudden precipitation of all SWNTs from the solution, presumably due to crosslinking PAM polymer through  $\text{Co}^{2+}$  ions. Additionally, the color of the polymer solution changed from red to blue, similarly to previously discussed results.

The presence of the ligands on the SWNTs was confirmed and characterized by atomic force microscopy (AFM) (Figure S2-6). The SWNTs showed a marked increase in diameter from

~ 1 nm (bare SWNTs) to ten or several tens of nanometers after PAM modification. As a comparison, AFM imaging revealed that the average diameters for MAC adsorbed on SWNT sidewalls ranged approximately from ~ 5 to 10 nm. Thus, AFM studies confirmed that the metal complex ligands, PAM and MAC both associate strongly with SWNTs through noncovalent interactions.

UV-vis-NIR absorption spectroscopy was also utilized to study the interactions of SWNT with the PAM or MAC ligands (Figures S2-7 and S2-8 respectively). Thin films of SWNT deposited onto quartz substrates were studied both before and after deposition of PAM polymer. The absorption spectrum for pristine SWNT clearly depicts the first two semiconducting and metallic electronic transitions, referred to as  $S_{11}$ ,  $S_{22}$ , and  $M_{11}$ , respectively. Figure 2-2C schematically illustrates these transitions in a density of states plot. The origin and significance of SWNT transition bands have been heavily studied and reported in detail.<sup>56,34</sup> All UV-vis-NIR spectra are normalized at 1400 nm, where no SWNT absorption band appears. There is one major absorption band observed for the PAM film, with a maximum wavelength value around 535 nm, and the SWNT film does not show any prominent peaks in this UV region. When PAM polymer was deposited on top of the SWNT film the major absorption peak was broadened and red-shifted by 35 nm ( $\lambda_{\max}$  value of 570 nm), presumably as a result of noncovalent  $\pi$ - $\pi$  interactions between the SWNTs and the  $\pi$ -conjugated PAM backbone. Moreover, the first two semiconducting transitions bands of SWNTs were affected when complexed with PAM polymer. Upon addition of PAM polymer onto the SWNT film, the  $S_{11}$  band has a reduced intensity and a red-shift of about 20 nm which can be also attributed to  $\pi$ - $\pi$  stacking interactions between the carbon nanotube networks and polymer backbone. The  $S_{22}$  band was not shifted but did experience a reduction in intensity. The  $M_{11}$  band was masked by the PAM absorption in the

UV-vis region, so any changes were not evident. The observed reduction in both  $S_{11}$  and  $S_{22}$  suggests that the polymer coating changes the dielectric environment of the SWNTs. Since PAM itself is not a conducting polymer due to its non-planar polymer backbone, PAM modified SWNT forms a dielectric layer. Specifically charge carriers do not flow through the polymer layer, but transfer between polymer layer and SWNT networks upon molecular interactions. Another important observation is that the conductance of the SWNT film suppressed greatly upon the polymer modification from  $628 \pm 2 \mu\text{S}$  for bare SWNT films to  $341 \pm 2 \mu\text{S}$  for PAM/SWNT complex (not shown). This observation is consistent with the reduction in both  $S_{11}$  and  $S_{22}$ , indicating a dielectric layer formed by PAM attachment. As an analog, the effect of MAC's interactions with a SWNT film has been studied using optical spectroscopy. Figure S2-8 shows that a peak at 392 nm appears upon addition of MAC to a SWNT suggesting that MAC is noncovalently attached to the SWNT film. The  $S_{11}$  band of SWNT film is shifted from 1847 to 1875 nm (a 28 nm red-shift) upon attachment, supporting the evidence of  $\pi$ - $\pi$  stacking interactions. These interactions play an important role in electron transport of the SWNT device. The increased absorption intensity of the  $S_{11}$  transition can be attributed to electron transfer from the higher HOMO of MAC toward the lower valence band of SWNT. Another possible factor is the electron donor hydroxyl groups in the MAC modified SWNT complex. Although these interactions are individually weak, the involvement of  $\pi$ - $\pi$  stacking interactions and electron-donor transfer along the MAC/SWNT complex provides a stable, noncovalently functionalized SWNT device.

#### 2.4.4 Co<sup>2+</sup> Detection on SWNT Devices

The thin film devices described previously were tested as chemical sensors for the detection of heavy- metal ions. Ligand modified SWNT thin films were brought into contact with Co<sup>2+</sup> ions, and UV-vis-NIR absorption and electrical conductance data were recorded. Co<sup>2+</sup> ions were deposited onto the chip from MeCN and allowed to dry in ambient. The UV-vis-NIR spectra of the ligand/SWNT thin film before and after addition of Co<sup>2+</sup> ions are shown in Figure 2-2. The complexation of Co<sup>2+</sup> ion with the PAM/SWNT thin film results in a small red shift for both SWNT and PAM electronic transition bands (Figure 2-2D). Additionally, the absorption intensities of the S<sub>11</sub> transitions increased upon Co<sup>2+</sup> additions. However, as the concentrations of Co<sup>2+</sup> are much lower than those used for solution titration, the color change of the PAM films was difficult to discern by the naked eye. These observations suggest that studying the optical properties alone does not provide an effective means for sensing the metal ions at very low concentrations. In addition, the changes for the S<sub>22</sub> transition were miniscule. For the analog device, MAC modified SWNTs, very little change in the spectrum were observed upon addition of Co<sup>2+</sup> ions, besides a miniscule increase in absorption intensity of the S<sub>11</sub> transition upon Co<sup>2+</sup> addition. (Figure 2-2E)

Taking advantage of the electrical configuration of the sensor device, real-time conductance measurements were taken for addition of cobalt ions at varying concentrations (Figure 2-2F-H). The conductance of PAM/SWNT decreased upon addition of Co<sup>2+</sup> ions with concentrations ranging from picomolar to millimolar range (Figure 2-2F). The response in SWNT conductance ( $\Delta G/G_0$ ) as a function of Co<sup>2+</sup> concentration ( $[Co^{2+}]$ ) (Figure 2-2H) scale with the logarithm (base 10) of the concentration of Co<sup>2+</sup> ions. It should be recalled here that color changes of the PAM film upon Co<sup>2+</sup> addition was only visible at relatively high

concentrations ( $10^{-4}$  M), thus they were not observed in this experiment. These results suggest that the PAM/SWNT thin film electrical device shows great potential for future development of SWNT-based metal ion sensor devices. For the analog device, MAC/SWNT complex, conductance measurement revealed that the film conductance decreased with addition of cobalt ion (Figure 2-2G), however, the change in conductance was significantly less than the PAM based device, and the response was only linear over the range of  $10^{-6}$  to  $10^{-3}$  M. The conductance of bare SWNTs when exposed to  $\text{Co}^{2+}$  ions increased in real-time with increasing concentrations of  $\text{Co}^{2+}$  ions. This response is opposite to those observed on PAM/SWNT and MAC/SWNT devices, indicating that chelation of  $\text{Co}^{2+}$  with the PAM or MAC ligands is responsible for the decrease in the conductance of the film. Plotting the relative response as a function of the concentration of  $\text{Co}^{2+}$  ions of PAM/SWNT and MAC/SWNT together reveals that the sensitivity (magnitude of slope of the curve) is much greater for PAM/SWNT complex. The conductance change of the PAM/SWNT device is linear to the logarithm of  $\text{Co}^{2+}$  concentration over all the ranges tested, while the change of MAC/SWNT is ten times diminished and has a much narrower dynamic range ( $10^{-6}$  to  $10^{-3}$  M). One possible explanation is that the PAM polymer has a large conformational change upon metal ion complexation. The conformational change of the polymer disturbed the carbon nanotube networks through  $\pi$ - $\pi$  stacking interactions, thus amplifying the electrical signal change. In contrast, the triangle conformation of macrocycle molecule is little affected by metal ion complexation, thus smaller influence on SWNT networks giving rise to its inherently lower sensitivity.

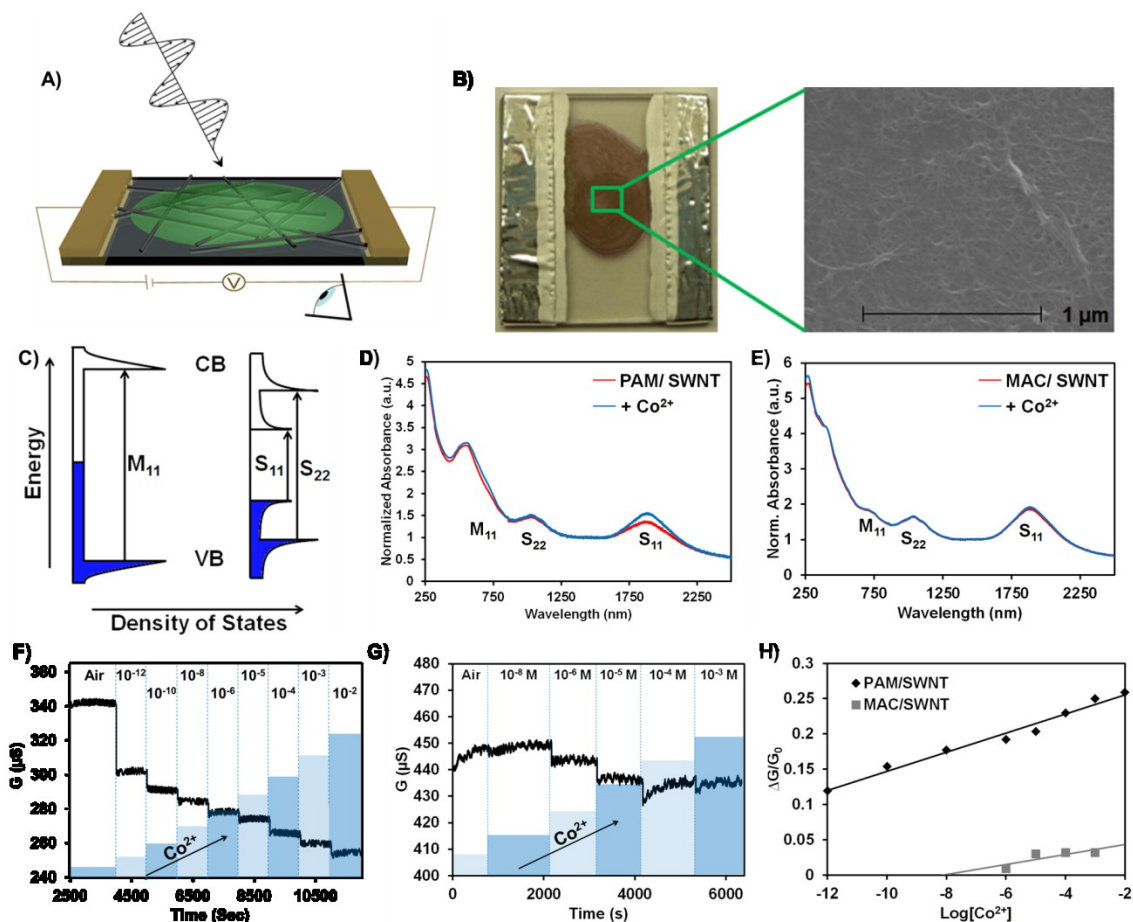


Figure 2-2. Optical and electrical dependence of PAM/SWNT and MAC/SWNT to  $\text{Co}^{2+}$  ions

A) Schematic drawing of a carbon nanotube/polymer device used in this study. Single-walled carbon nanotubes (SWNT) and a noncovalently functionalized ligand deposited on a quartz plate forming a transparent yet conducting thin film. B) Photograph of a quartz plate with two Al foil electrodes conned to the film using silver paint. Magnification of the PAM/SWNT via scanning electron microscopy (SEM) reveals the morphology of the nanotube/polymer film. C) Density of states (DOS) diagram showing the electron transitions in SWNTs. D) Optical response of PAM/SWNT to  $\text{Co}^{2+}$  ions. Specifically the S11 SWNT band increases upon addition of  $\text{Co}^{2+}$  ions. E) Optical response of MAC/SWNT to  $\text{Co}^{2+}$  ions where the change in the S11 transition band is significantly less. F) Electrical conductance (G) of PAM/SWNT film in air and in varying concentrations (M) of  $\text{Co}^{2+}$  ions. G) Real-time conductance measurement of MAC/SWNT to varying concentrations of  $\text{Co}^{2+}$  ions. H) Relative response plot comparing  $\text{Co}^{2+}$  ion sensitivity of PAM/SWNT to MAC/SWNT. PAM/SWNT shows the greatest response over the largest dynamic range, and additionally, the response scales with the logarithm of the concentration of ions.

#### 2.4.5 Transduction Mechanism for $\text{Co}^{2+}$ Sensing

Insight about the transduction mechanism for cobalt ion detection can be obtained by looking at the combined spectroscopic and electrical behavior of bare SWNTs undergoing noncovalent interactions with an electron-donor or electron-acceptor (Figure 2-3). The increased conductance on a bare p-type SWNT upon increasing concentrations of cobalt ions (Figure 2-3B) is expected for positively charged ions adsorbed on p-type SWNTs because they increase the concentration of p-type carriers (hole-carriers); at the same time, electron density in the SWNT is reduced and thus the decrease in the intensity of the  $S_{11}$  transition band (Figure 2-3A). On the contrary, quite the opposite effect was observed for the ligand/SWNT complexes. Specifically, the exposure to  $\text{Co}^{2+}$  ions enhanced the  $S_{11}$  transitions, and increased the overall conductance of the device. The increase in absorption intensity of the  $S_{11}$  transition band is indicative of electron donation to the top of the SWNT valence band. This would also decrease the number of hole-carriers which explains the decrease in the film conductance. Moreover, the conformational changes of the PAM polymer upon cobalt coordination deform the SWNT network through  $\pi$ - $\pi$  stacking interactions and thus amplify conductance signals as a result. This possible explanation is supported by the significant lowering of the detection limit for the PAM based device compared to the rigid MAC.

Figure 2-4 schematically illustrates the difference between the three systems tested for  $\text{Co}^{2+}$  ion sensitivity. In Figure 2-4A,  $\text{Co}^{2+}$  ions attach to the sidewalls of SWNTs resulting in changes in electrical and optical properties. Additionally, for MAC/SWNT,  $\text{Co}^{2+}$  ions will complex with available macrocycles resulting in similar changes in the properties of SWNTs as bare SWNTs. However, when PAM is functionalized onto SWNTs, addition of  $\text{Co}^{2+}$  ions results

in a rearrangement of the polymer on the SWNT surface, amplifying changes in electrical and optical properties of SWNTs.

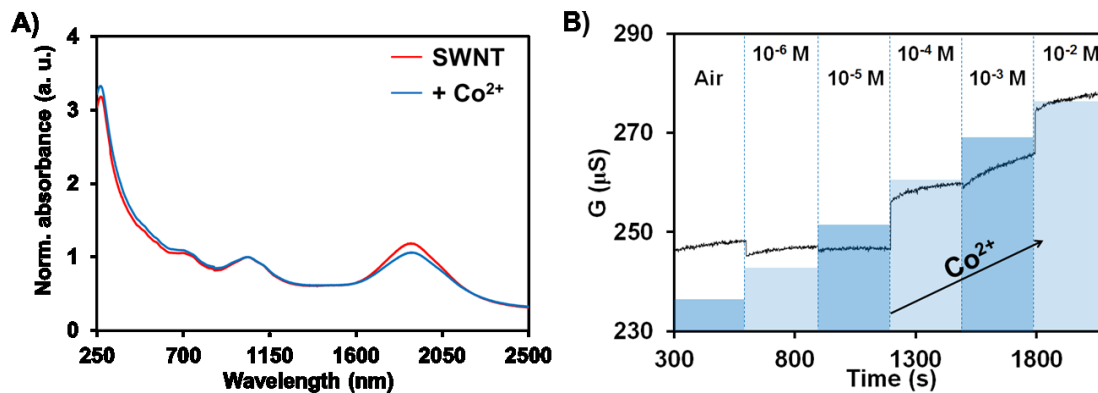


**Figure 2-3.** Optical and electrical response of bare SWNT to  $\text{Co}^{2+}$  ions

A) UV-vis-NIR absorption spectra of bare SWNT (red) and the response of SWNT to  $10^{-2}$  M  $\text{Co}^{2+}$  ions (blue). B) Real-time conductance measurements of bare SWNT for varying concentration of  $\text{Co}^{2+}$  ions.

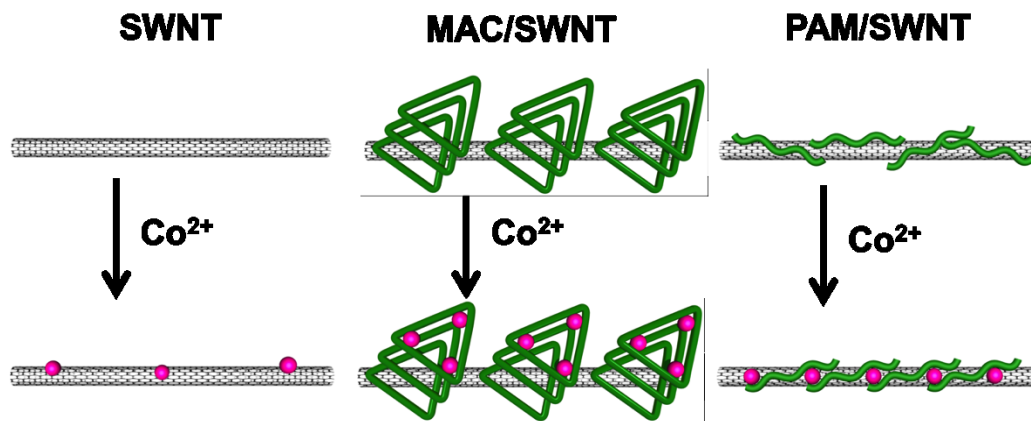


**Figure 2-4.** Schematic representation of the proposed mechanism of detection

Upon addition of  $\text{Co}^{2+}$  ions to MAC/SWNT the ions fill any open macrocycles, which offers no advantage over bare SWNT with respect to changes in electrical conductance. On the other hand, addition of  $\text{Co}^{2+}$  ions to PAM/SWNT will invoke a rearrangement of the polymer to bind with the metal ion resulting in a great enhancement in signal.

#### 2.4.6 Cu<sup>2+</sup> Detection on PAM/SWNT Devices

PAM complexation has been studied with various transition metal ions such as Co<sup>2+</sup>, Fe<sup>2+</sup>, Zn<sup>2+</sup>, and Cu<sup>2+</sup>. Among these metal complexation, PAM undergoes the largest conformational change upon Co<sup>2+</sup> coordination supported by the largest red-shift (~ 160 nm). On the other hand, Cu<sup>2+</sup> coordination undergoes a relatively weaker conformational change with a red-shift of only ~ 40 nm. (Figure S2-9) Therefore the optical/electrical device was tested for varying concentration of Cu<sup>2+</sup> ions in order to further understand the transduction mechanism of the PAM/SWNT sensor device (Figure S2-10). UV-vis-NIR absorption spectroscopy reveals a decrease in the absorption intensity of the S<sub>11</sub> transition band upon addition of 10<sup>-3</sup> M Cu<sup>2+</sup> ions. At the same time, the film conductivity increased upon increasing concentrations of Cu<sup>2+</sup> ions from the picomolar to millimolar range. Presuming that Cu<sup>2+</sup> works as an electron acceptor, its addition onto the PAM/SWNT film induces electron withdrawal from SWNT valence band, thus reducing the S<sub>11</sub> transition band. Meanwhile, the increased amount of hole carriers results in the enhancement of film conductance with increasing concentration of copper ions. However, the conformational change of PAM upon coordination of Cu<sup>2+</sup> is much smaller than coordination with Co<sup>2+</sup>, which elucidates the origin of the smaller response, and supporting the reasoning behind PAM/SWNT thin film device selectivity to cobalt ions. Additionally the response of bare SWNTs to varying concentrations of Cu<sup>2+</sup> ions similar to that of Co<sup>2+</sup> ions suggesting that the increased response is from the polymer and not the nanotube (Figure S2-11).

## 2.5 CONCLUSION

In conclusion, ultrasensitive  $\text{Co}^{2+}$  ion detection has been presented based on a noncovalent PAM/SWNT optoelectronic device. Detection of picomoles ( $10^{-12}$  moles) of  $\text{Co}^{2+}$  ions has been demonstrated with a fast response time and high selectivity. Both spectroscopic and electrical signals agree and their comparison gives insight on the mechanism of detection. Additional information was gained on the sensor transduction pathway by comparing the properties of two similar molecules, PAM and MAC, with their only significant difference being their flexible versus rigid nature respectively. While signal changes in the MAC/SWNT device did not significantly differ from that of a bare SWNT device, it has been concluded that, due to the flexible nature of PAM, rearrangement of the chain molecule upon metal ion coordination induces electron transfer with the SWNT network.

**ACKNOWLEDGMENT** This work was performed in support of ongoing research in sensor systems and diagnostics at the National Technology Laboratory (NETL) under RES contract DE-FE0004000.

## 2.6 SUPPORTING INFORMATION

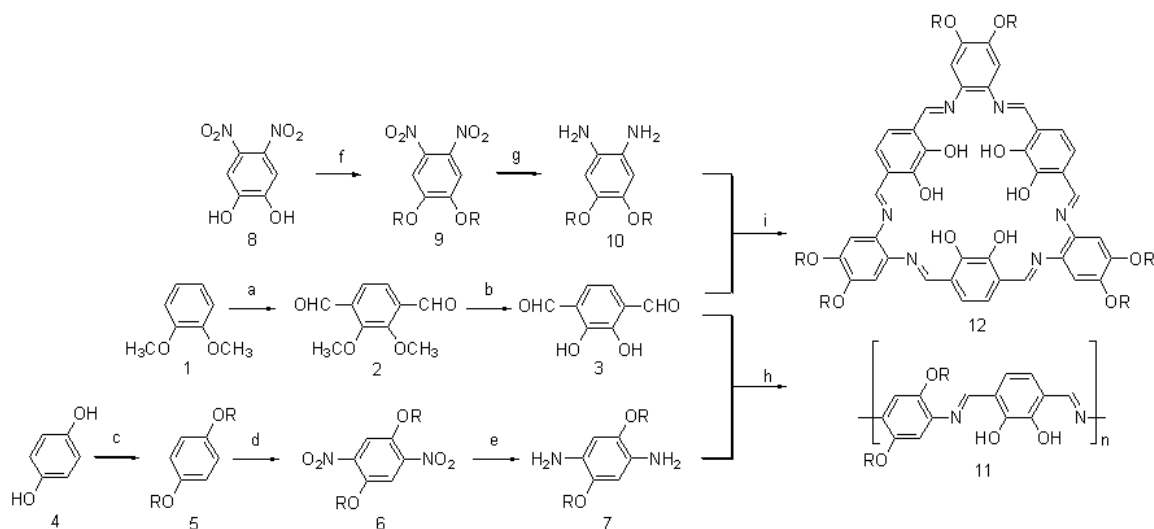
### Table of Contents:

- I. Experimental Section
- II. Figure S2-1.  $^1\text{H}$ -NMR spectrum of polyazomethine (PAM) polymer.
- III. Figure S2-2. FTIR spectrum of PAM polymer.
- IV. Figure S2-3. UV-vis-NIR absorption spectra of PAM and its constituent monomers.

- V. Figure S2-4. Normalized absorption and emission spectra of PAM polymer
- VI. Figure S2-5. Optical response of PAM polymer to acidic and basic vapors.
- VII. Figure S2-6. AFM images of bare SWNTs, PAM/SWNT, and MAC/SWNT.
- VIII. Figure S2-7. UV-vis-NIR absorption spectra of SWNT, PAM, and PAM/SWNT.
- IX. Figure S2-8. UV-vis-NIR absorption spectra of SWNT and MAC/SWNT.
- X. Figure S2-9. UV-Vis titration of PAM polymer with  $\text{CuCl}_2$ .
- XI. Figure S2-10. Optical and electrical dependence of PAM/SWNTs to  $\text{Cu}^{2+}$  ions
- XII. Figure S2-11. Electrical dependence of bare SWNTs to  $\text{Cu}^{2+}$  ions.

## Experimental Section

**Materials and Instrumentation.** Chemicals were purchased from Aldrich and used as received. Solvents were dried, distilled, and stored under argon. All reactions were carried out under N<sub>2</sub> atmosphere unless otherwise stated. Column chromatography was performed using Merck silica gel 60. Melting points (mp) were determined on an Electrothermal melting apparatus and are uncorrected. UV/Visible spectra were obtained using a PerkinElmer Lambda 900 spectrophotometer. FT-IR spectra were recorded as thin film on NaCl plates or as KBr pellets on an Avatar 380 Nicolet FI-IR spectrometer. Proton and carbon nuclear magnetic resonance (<sup>1</sup>H-NMR) spectra were recorded on a Bruker DPX 300 (300 MHz) NMR spectrometer at 25°C, using the deuterated solvent as lock and the residual solvent as internal standard. Electron impact ionization mass spectrometry (EI-MS) was performed on a VG-AutoSpec instrument. High resolution mass spectra were taken on a VG-Autospec double focusing spectrometer. Molecular weights of polymers were determined by using a Waters Gel Permeation Chromatography system equipped with Waters 510 HPLC pump, phenogel columns and a Waters 410 Differential Refractometer at a flow rate of 0.4 mL/min. All molecular weights were measured against polystyrene standards in THF.



**Scheme S 2-1.** Synthesis of polyazomethine (PAM) and salophen macrocycle (MAC) in detail

Reagents and Conditions: (a)(i)  $n\text{-BuLi}$ , TMEDA,  $\text{Et}_2\text{O}$ , reflux, 10 hr. (ii) DMF,  $\text{H}_2\text{O}$ , HCl, 28%; (b)  $\text{BBr}_3$ ,  $\text{CH}_2\text{Cl}_2$ , then  $\text{H}_2\text{O}$ , 90%; (c)  $\text{C}_8\text{H}_{17}\text{Cl}$ ,  $\text{K}_2\text{CO}_3/\text{DMF}$ ,  $80^\circ\text{C}$ , 36 h, 98%; (d)  $\text{HNO}_3/\text{AcOH}$ , 27%; (e)(i) 10% Pd/C,  $\text{N}_2\text{H}_4$ , EtOH, reflux, 70%; (ii) recryst, hexane, 46%; (f)  $\text{C}_8\text{H}_{17}\text{Br}$ ,  $\text{CS}_2\text{CO}_3/\text{DMF}$ ,  $100^\circ\text{C}$  3 h, 60%; (g) 10% Pd/C,  $\text{N}_2\text{H}_4$ , EtOH, reflux, 86%; (h)  $\text{LiCl}/\text{DMAP}/\text{HMPA}/\text{NMP}$ , RT, 56%; (i)  $\text{CHCl}_3/\text{MeCN}$ ,  $90^\circ\text{C}$ , 2 hr, 70%

**1,2-Dimethoxy-3,6-diformylbenzene (2).**<sup>57</sup> Tetramethylethylenediamine (TMED) (4.61 mL, 180 mmol) was added to a solution of 1,2-dimethoxybenzene (**1**) (4.61 mL, 36mmol) in 50 mL of anhydrous Et<sub>2</sub>O at RT. A 1.6 M solution of n-BuLi in hexane (112.65mL, 180 mmol) was added dropwise to the reaction mixture at 0°C. The mixture was then heated under reflux for 10 hours to form a grey yellow organolithium salt intermediate. After cooling to 0°C, anhydrous dimethylformamide (DMF) (13.30 ml, 180 mmol) was added and the reaction mixture and stirred for an additional 30 min. To the resulting orange mixture, 100 mL of H<sub>2</sub>O and 40 mL of 3M HCl were added and the product was extracted into 100 mL of Et<sub>2</sub>O three times. The product was then washed with H<sub>2</sub>O, dried in Na<sub>2</sub>SO<sub>4</sub>, and the solvent was evaporated off. The product mixture was separated by column chromatography (SiO<sub>2</sub>: Hexane/EtOAc, 10:1), and crystallization from petrol ether yielded 1,2-dimethoxy-3,6-diformylbenzene as a light yellow solid (1.98 g, 28%). m.p. 72-88 °C (light petroleum). <sup>1</sup>H-NMR (CDCl<sub>3</sub>) δ 10.43 (2H, s, CHO), 7.62 (2H, s, aromatic CH), 4.05 (6H, s, OMe).

**3,6-Diformylcatechol (3).**<sup>48</sup> A 1.0 M solution of BBr<sub>3</sub> in 8.51 mL (8.51 mmol) of CH<sub>2</sub>Cl<sub>2</sub> was added dropwise through a septum with use of a syringe to a stirred solution of 500 mg (2.6 mmol) 1,2-dimethoxy-3,6-diformylbenzene (**2**) in 5mL of dry CH<sub>2</sub>Cl<sub>2</sub> at -78 °C. The reaction mixture was stirred under inert atmosphere for an additional 40 min at room temperature. The reaction mixture was subsequently poured into 50 mL of ice water, stirred for 40 min, and then saturated with NaCl salt. The product was isolated by extraction into 30 mL of CH<sub>2</sub>Cl<sub>2</sub> three times, washed with H<sub>2</sub>O, dried in Na<sub>2</sub>SO<sub>4</sub>, and evaporated to afford 3,5-diformylcatechol as a grassy yellow solid (388 mg, 90%). m.p. 143-145°C (hexane). <sup>1</sup>H-NMR (DMSO-D<sub>6</sub>) δ 10.28 (2H, s, CHO), 7.25 (2H, s, aromatic CH). EI, m/e (relative intensity): 166.03 (100). HR EI-MS:

calcd. For C<sub>8</sub>H<sub>6</sub>O<sub>4</sub> (M<sup>+</sup>) 166.026609; found 166.026491. Anal. Calc'd for C<sub>8</sub>H<sub>6</sub>O<sub>4</sub> : C, 57.87; H, 3.64. Found: C, 58.08; H, 3.79.

**1,4-Dioctyloxybenzene (5).** A solution of hydroquinone (**4**) (11 g, 0.1mmol), of 1-chlorooctane (51 mL, 0.3 mol), and of K<sub>2</sub>CO<sub>3</sub> (69 g, 0.5 mol) in 200 mL of DMF was heated for 36 h at 80°C. After cooling, the precipitate was filtered off, and the solution was concentrated under high vacuum. The product was isolated by precipitation with MeOH to afford 1,4-dioctyloxybenzen as white solid (23g, 98%). Mp 55-56°C. <sup>1</sup>H-NMR (CDCl<sub>3</sub>) δ 6.82 (4H, s, aromatic CH), 3.89 (4H, t, <sup>3</sup>J<sub>HH</sub> = 6.6 Hz, OCH<sub>2</sub>), 1.75 (4H, m, CH<sub>2</sub>), 1.44 (20H, m, CH<sub>2</sub>), 0.88 (6H, t, <sup>3</sup>J<sub>HH</sub> = 6.0 Hz, CH<sub>3</sub>).

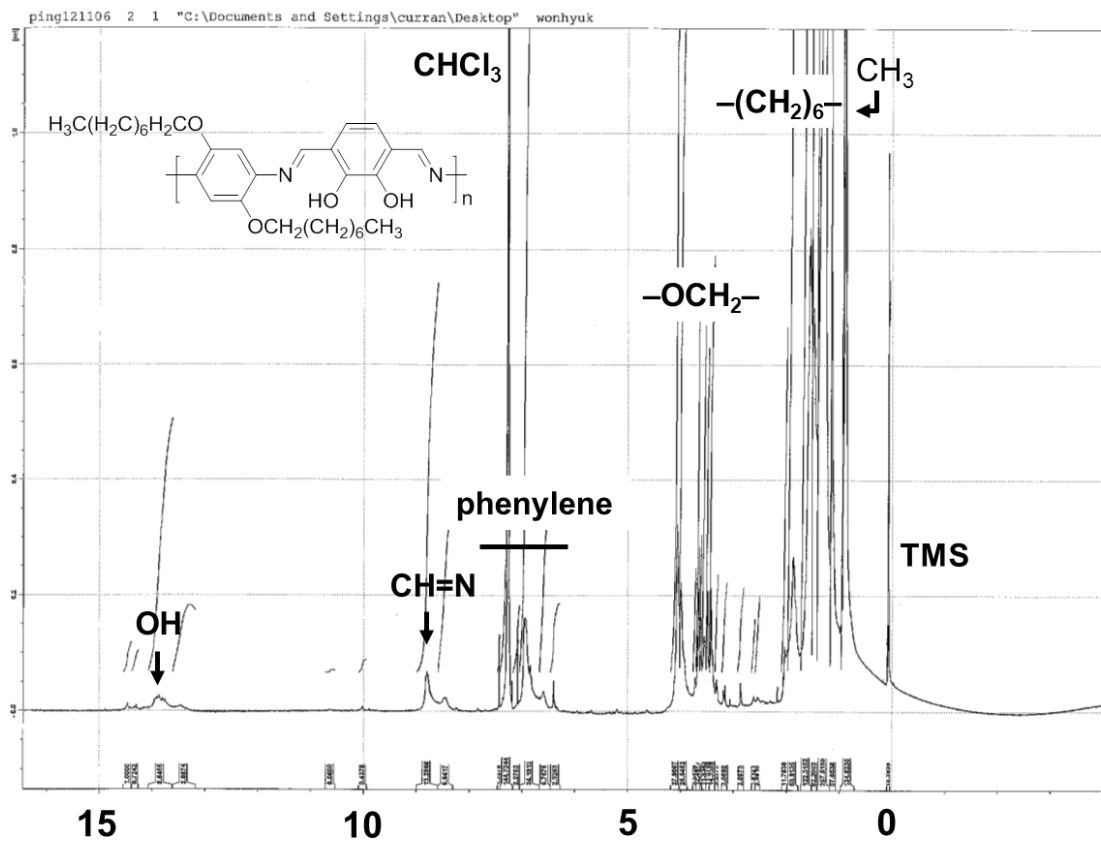
**1,4-Dioctyloxy-2,5-dinitrobenzene (6).** Concentrated HNO<sub>3</sub> (25 mL) was added dropwise to a solution of 1,2-dioctyloxybenzene (**5**) (15.2 g, 45.5 mmol) in 50 mL of glacial AcOH. (Caution: extremely exothermic reaction). The reaction mixture was then heated at 80-90°C for additional 5 min and another 25 mL of concentrated HNO<sub>3</sub> was added. After cooling, 500 mL of iced water was added to the reaction mixture, and the yellow precipitate was filtered from the solution. The product is a mixture of 1,4-dioctyloxy-2,5-dinitrobenzene and 1,4-dioctyloxy-2,3-dinitrobenzene, and they were subsequently separated by column chromatography (SiO<sub>2</sub>: Hexane/EtOAc, 30:1 then 10:1). Crystallization from EtOH yielded 1,4-dioctyloxy-2,5-dinitrobenzene as yellow sheet crystals (5.2 g, 27%): Mp 100-101°C. <sup>1</sup>H-NMR (CDCl<sub>3</sub>) δ 7.52 (2H, s, aromatic CH), 4.10 (4H, t, <sup>3</sup>J<sub>HH</sub> = 6.4 Hz, OCH<sub>2</sub>), 1.84 (4H, m, CH<sub>2</sub>), 1.33 (20H, m, CH<sub>2</sub>), 0.90 (6H, t, <sup>3</sup>J<sub>HH</sub> = 6.6 Hz, CH<sub>3</sub>). Anal. Calc'd for C<sub>22</sub>H<sub>36</sub>N<sub>2</sub>O<sub>6</sub> : C, 62.24; H, 8.55; N, 6.60. Found: C, 62.22; H, 8.65; N, 6.53.

**1,4-Dioctyloxy-2,5-phenylenediamine (7).** To a solution of 1,4-dioctyloxy-2,5-dinitrobenzene (**6**) (580 mg, 1.37 mmol) in 40 mL of EtOH, 10% Pd/C (40 mg) and of hydrazine

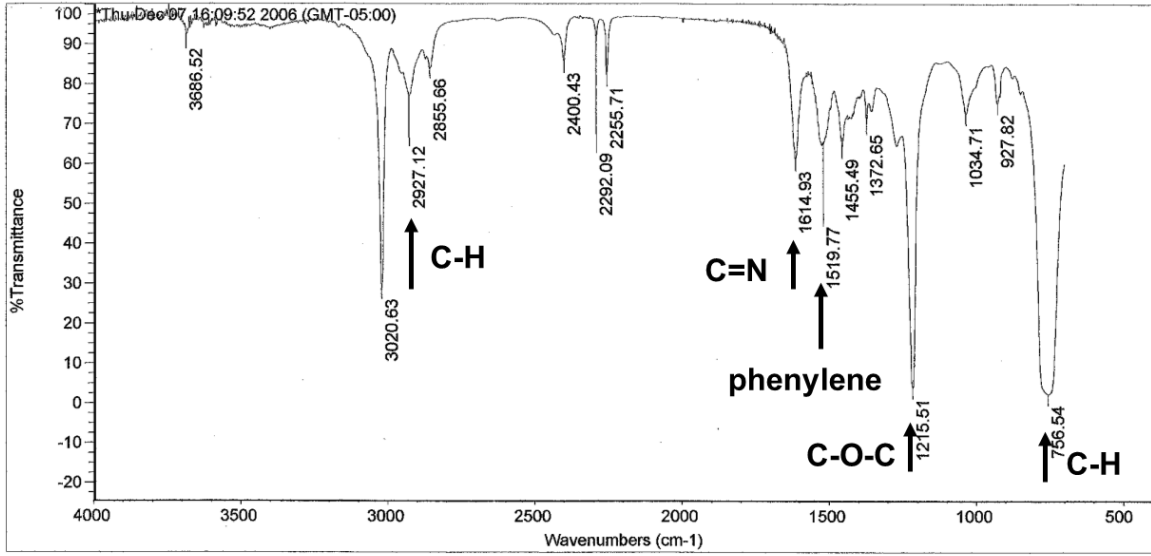
monohydrate (2.5 mL, 51 mmol) were added. The resulting solution was heated at 80 °C for 5 h, and brownish red solution became colorless. After cooling to room temperature, the catalyst was filtered out and EtOH was evaporated under reduced pressure. 20 mL of hexane was added to the flask and kept in the freezer overnight to provide the pure product 1,4-dioctyloxy-2,5-diaminobenzene as a white precipitate (220 mg, 46%). <sup>1</sup>H-NMR (CDCl<sub>3</sub>) δ 6.34 (2H, s, aromatic CH), 3.90 (4H, t, <sup>3</sup>J<sub>HH</sub> = 5.47 Hz, OCH<sub>2</sub>), 1.73 (4H, m, CH<sub>2</sub>), 1.28 (20H, m, CH<sub>2</sub>), 0.88 (6H, t, <sup>3</sup>J<sub>HH</sub> = 6.69 Hz, CH<sub>3</sub>). EI, *m/e* (relative intensity): 364.31 (83). HR EI-MS: calcd. For C<sub>22</sub>H<sub>40</sub>N<sub>2</sub>O<sub>2</sub> (M<sup>+</sup>) 364.308979; found 364.309616.

**1,2-Octyloxy-4,5-dinitrobenzene (9).**<sup>50</sup> To a mixture of 4,5-dinitrocatechol (**8**) (302 mg, 1.5 mmol) and Cs<sub>2</sub>CO<sub>3</sub> (984 mg, 3.0 mmol) in DMF (5 mL), 1-bromooctane (0.78 mL, 4.5 mmol) was added. The resulting mixture was stirred for 3h at 100 °C under a N<sub>2</sub> atmosphere. After evaporation of the mixture, the product was purified by column chromatography (SiO<sub>2</sub>, hexane/EtOAc = 40/1) to yield 1,2-octyloxy-4,5-phenylenediamine as a yellowish solid (382 mg, 60%)

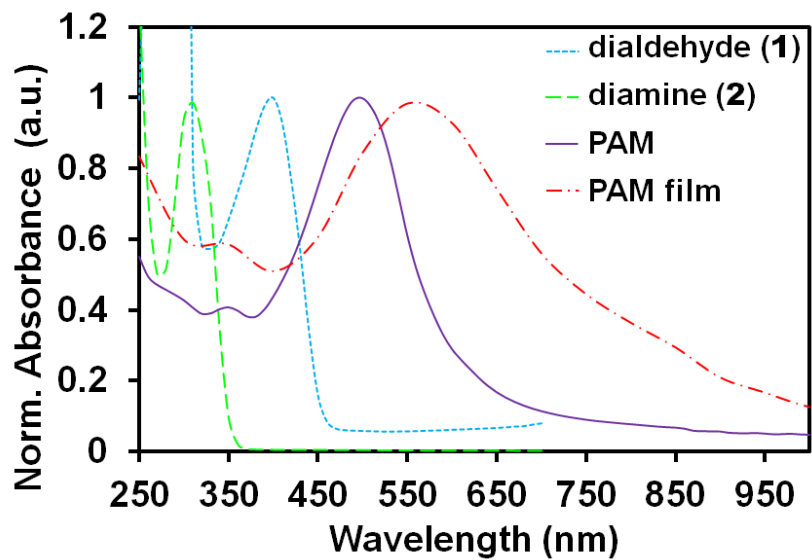
**1,2-Octyloxy-4,5-phenylenediamine (10).** To a solution of 1,2-Octyloxy-4,5-dinitrobenzene (**9**) (580 mg, 1.37 mmol) in EtOH (40 mL), 10% Pd/C (40 mg) and hydrazine monohydrate (2.5 mL, 15 mmol) were added. After 5h of refluxing, the hot solution was filtered through Celite. After cooling, the white precipitate was filtered off and rinsed with chilled MeOH to yield 1,2-octyloxy-4,5-diaminobenzene (430 mg, 86%). The diamine is quite unstable to storage and the following steps were carried out immediately.



FigureS 2-1. <sup>1</sup>H-NMR (CDCl<sub>3</sub>, 300 MHz) of PAM polymer

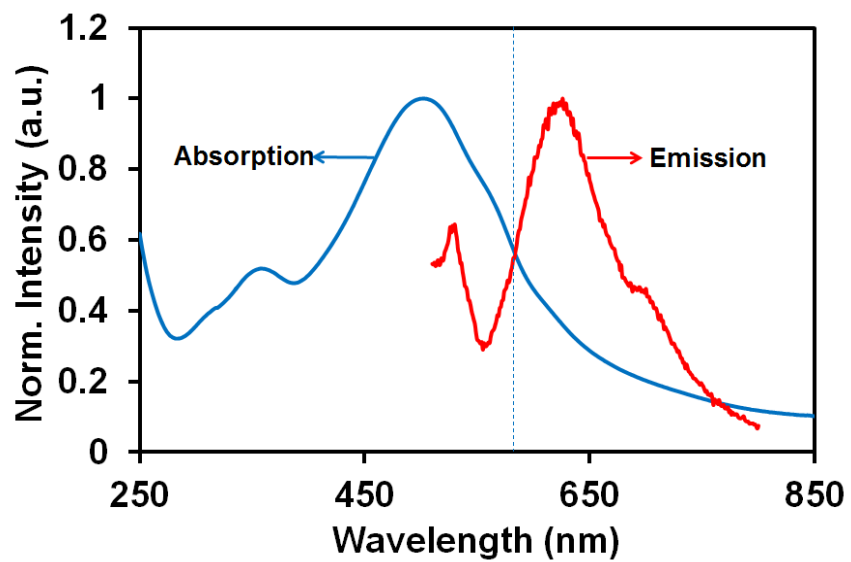


FigureS 2-2. FTIR (NaCl) spectra of PAM polymer



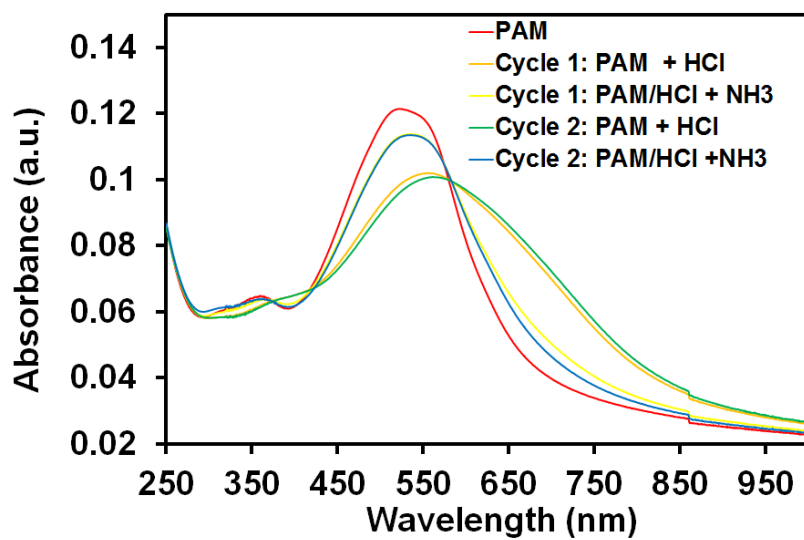
**FigureS 2-3.** UV-vis absorption spectra of PAM and its constituent monomers

Spectra of PAM in solution (THF) and as a solid film deposited onto a quartz plate, and spectra of PAM's constituent monomers, 1,4-dioctyloxy-2,5-phenylenediamine (diamine (1)) and 3,6-diformylcatechol (dialdehyde (2)), in THF are also given for a comparison.



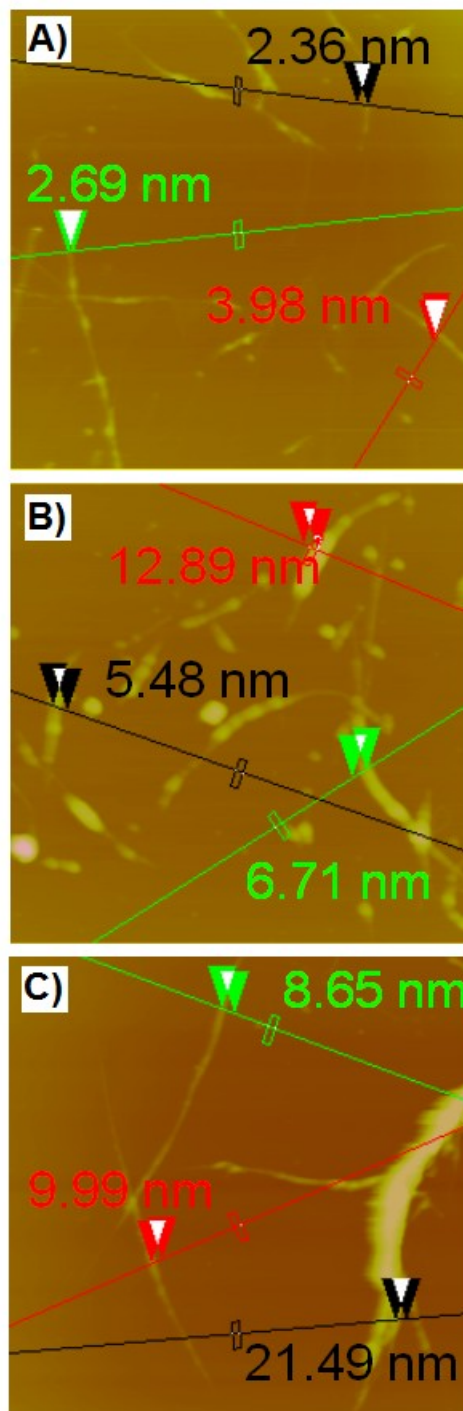
**FigureS 2-4.** Normalized absorption and emission spectra of PAM polymer (in THF)

It allow for estimation of the bandgap of the conducting polymer to be ca. 2.1 eV.



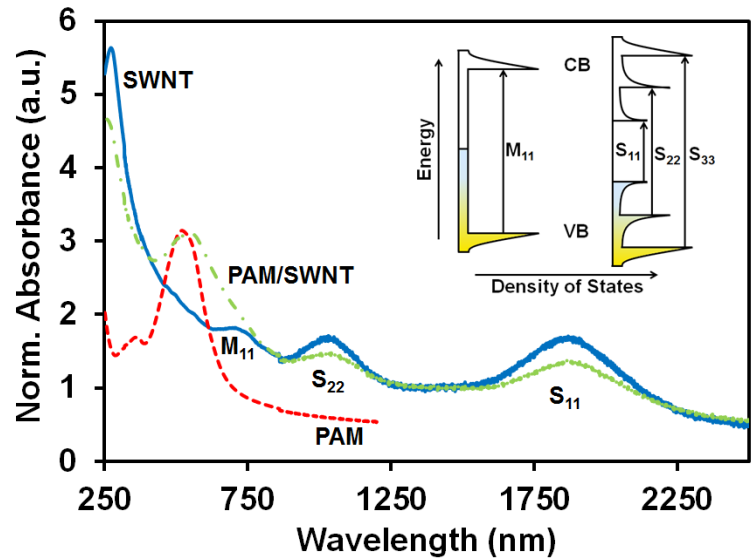
**FigureS 2-5.** Optical reponse of PAM polymer in acidic and basic vapors

Absorption spectra of PAM polymer thin film on quartz plate as well as its response upon treatment with HCl and NH<sub>3</sub> vapors.



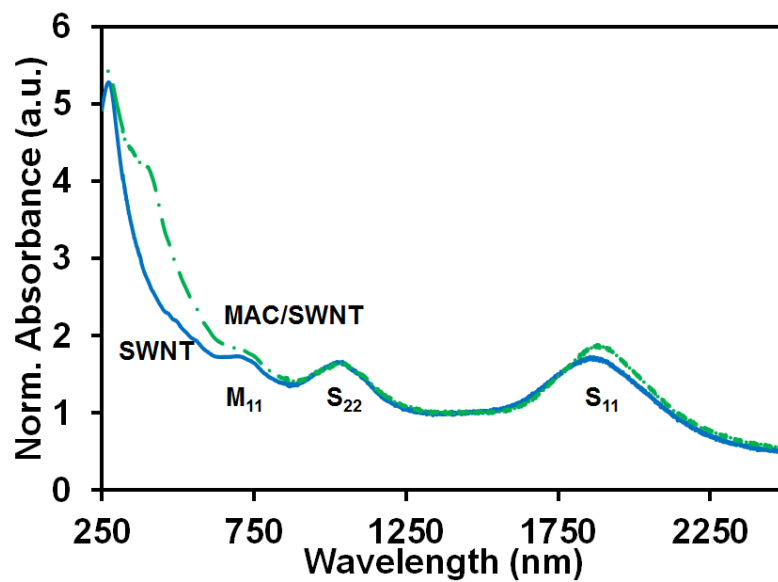
**FigureS 2-6.** AFM images of bare SWNT, MAC/SWNT and PAM/SWNT

AFM images and section analysis of (A) bare SWNT, (B) MAC/SWNT, (C) and PAM/SWNT.



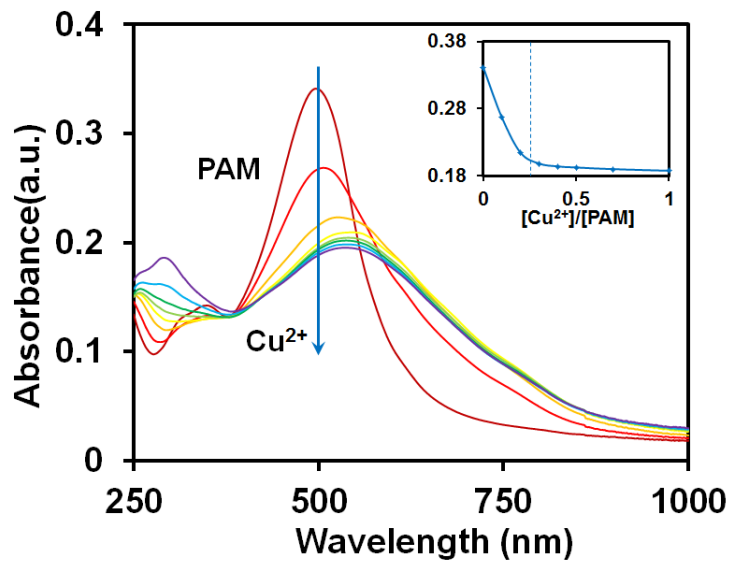
**FigureS 2-7.** UV-vis-NIR absorption spectra of SWNT, PAM, and PAM/SWNT

UV-vis-NIR absorption spectra of SWNT (blue), PAM (red) and PAM/SWNT (green). Inset: Density of states (DOS) diagram showing the electron transitions in SWNTs.



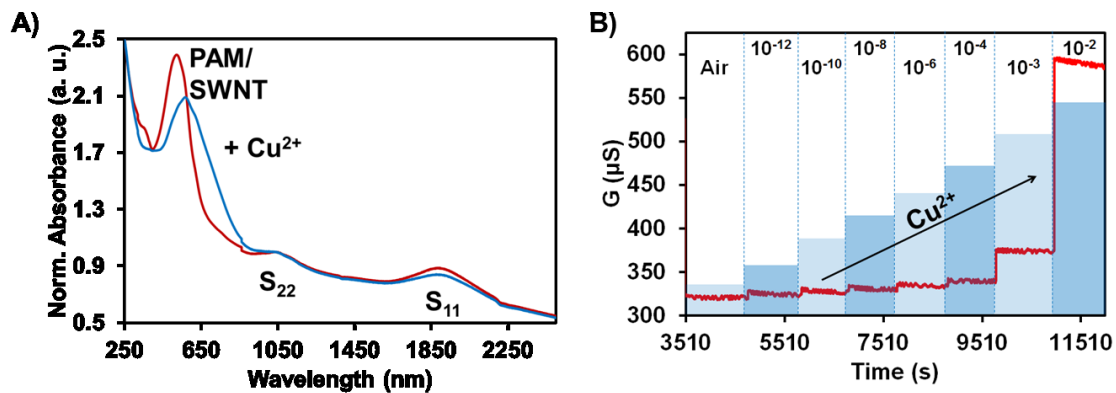
**FigureS 2-8.** UV-vis-NIR absorption spectra of SWNT and MAC/SWNT

UV-vis-NIR absorption spectra of SWNT (blue) and MAC/SWNT (green).



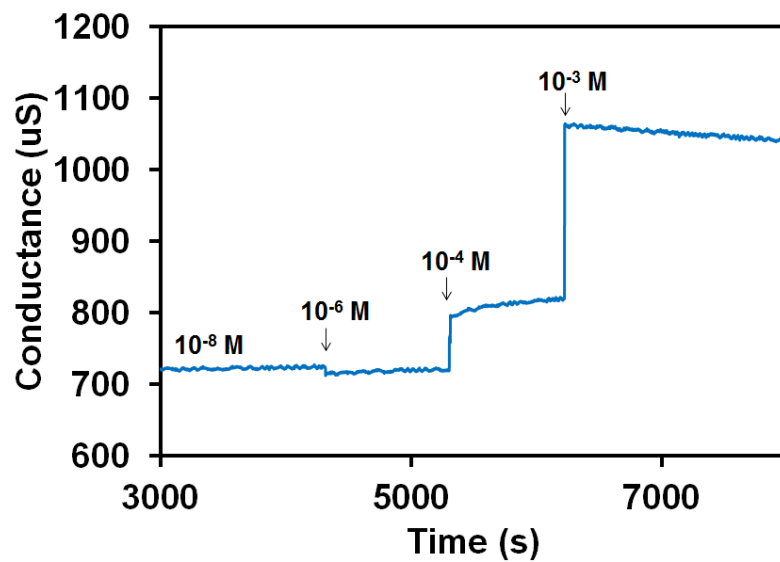
**FigureS 2-9.** UV-Vis titration of PAM polymer with  $\text{CuCl}_2$

The inset shows the absorption intensity of the complex ( $\lambda_{\text{max}}=500\text{nm}$ ) as a function of  $\text{Cu}^{2+}$  to PAM ratio, where the concentration of PAM is  $10^{-4}$  M.



FigureS 2-10. Optical and electrical dependence of PAM/SWNTs to Cu<sup>2+</sup> ions

A) UV-Vis-NIR absorption spectra of a PAM/SWNT film (red) and the film upon addition of 10<sup>-2</sup> M Cu<sup>2+</sup> ions (blue). B) Conductance dependence of PAM/SWNT to varying concentrations (M) of Cu<sup>2+</sup> ions.



**FigureS 2-11.** Electrical dependence of bare SWNTs to  $\text{Cu}^{2+}$  ions

Real-time conductance measurement of a bare SWNT film exposed to varying concentrations of  $\text{Cu}^{2+}$  ions.

### 3.0 SOLID STATE PH SENSORS BASED ON CARBON NANOTUBES

The results presented in this chapter will be submitted for publication in the near future.

**List of Authors:** Pingping Gou, Ian Matthew Feigel, and Alexander Star.

### 3.1 CHAPTER PREFACE

The aim of this work was to develop a SWNT-based pH-sensing platform based upon noncovalent interactions between poly(1-aminoanthracene) (pAA) and oxidized SWNTs. It was reported that the protonation and deprotonation of the carboxylic groups on oxidized SWNTs could cause electrostatic doping/charging of the nanotube and therefore shift its Fermi level.<sup>58</sup> In this work, this effect was amplified by noncovalent interactions involving hydrogen bonding and  $\pi$ - $\pi$  stacking between pAA and SWNTs. The pAA/SWNT sensory system displayed high sensitivity, selectivity, and stability. Moreover, the interactions and pH sensing mechanism were investigated by the combined techniques of optical spectroscopy and electrical measurements.

## 3.2 INTRODUCTION

Aqueous solutions receive a lot of attention as water covers over seventy percent of the planet and is vital for all known forms of life. In water, hydrogen ions constantly transfer from one water molecule to another forming two charged species: the hydroxide ion ( $\text{OH}^-$ ) and the hydronium ion ( $\text{H}_3\text{O}^+$ ). While the relative concentrations of these two ions can vary, their product remains constant. Addition of foreign species, such as an acid or a base, can adjust the ratio of these two ions. The pH scale, a log concentration scale, has been developed to define such solutions, which is related to the concentration of hydronium ions by  $\text{pH} = -\log [\text{H}_3\text{O}^+]$ . Concurrently, the term pH originated from a French term meaning “power of hydrogen.” The pH of a solution can have a significant effect on chemical processes, therefore both the measurement and control of pH is important for materials, life, and environmental sciences. For example, it would be beneficial to monitor the pH inside the human body, however is very difficult with conventional technologies. Additionally, pH sensors which can be exposed to extraordinary conditions, such as extreme temperature and pressure, can be applied in geochemistry for monitoring pH levels inside the earth’s ocean and facilitate carbon sequestration technologies.

The most common pH sensors are glass electrodes with a salt solution-filled glass membrane, however their applications are limited. Some common problems associated with such electrodes include temperature dependence and errors in measurement under intense conditions (i.e., low pH and low ionic-strength solutions).<sup>59</sup> Additionally, glass pH electrodes become sensitive to alkali-metal ions at high pH, degrade if dehydrated, and require calibration with a standard buffer, which has errors associated with itself. The field of ion-selective field-effect transistors (ISFETs) which started more than 40 years ago<sup>60</sup> has promised development of rugged, small, rapid response pH sensor devices. Additionally, ISFETs would not require

hydration and would be inert toward harsh environments. While there are numerous advantages of using ISFETs, one major limitation of the technology involves the requirement of a reference electrode ultimately limiting their size.<sup>60</sup> Continued efforts have been made to develop on-chip tiny reference electrodes; however their need causes ISFETs to suffer the same limitations as conventional glass pH electrodes. Therefore a crucial factor for development of ISFET remains the reference electrode. We demonstrate here that carbon nanotube (CNT) based chemiresistors could alleviate the aforementioned problems. Specifically, a chemiresistor based on CNTs only requires measurement of the resistance of the nanotube network as a function of ion concentration, making measurement relatively easy. The low-cost, rugged properties of CNT based sensors and the excellent electronic properties of single-walled carbon nanotubes (SWNTs) offer great potential as a platform for a stable, miniaturized pH sensor.

To achieve the required specificity to hydronium ions ( $\text{H}_3\text{O}^+$ ), carbon nanotubes were functionalized with a conducting polymer. Recently, conducting polymers have been studied for detection of pH,<sup>61,62,63</sup> as their electrical properties strongly depend on their protonation, and interestingly have shown very fast response when the sensing process occurs on the surface of the polymer.<sup>64</sup> However, a major problem of all organic conductors is their limited chemical stability. CNTs can help to stabilize polymers, increasing the lifetime of the sensor device,<sup>33</sup> while additionally increasing the aspect ratio of the polymer for facile integration into micrometer sized electronics. It is apparent that by combining the two types of materials synergetic effects are observed: First, the polymer contributes to the device selectivity, while the carbon nanotubes provide a sensitive and robust platform necessary to chemically stabilize the polymer. Polypyrrole (PPy) and polyaniline (PANi) polymers have been combined with nanotubes toward the development of solid state pH sensor devices,<sup>65</sup> however these

electrochemical based devices require the use of a reference electrode which limits many advantages of the system.

We have developed a pH sensitive device by combining oxidized SWNTs (o-SWNTs) with a conducting polymer, poly(1-aminoanthracene) (PAA) that does not require the use of a reference electrode. The pH levels can be monitored electrically by configuring the nanotube/polymer composite as a chemiresistor as well as optically by depositing a film onto a quartz plate. Specifically, the conductance of the PAA/o-SWNT network changes linearly with respect to the concentration of hydronium ions in solution. Additionally the absorption of the S<sub>11</sub> electronic transition of a PAA/o-SWNT film is influenced by the presence of acidic (HCl) or basic (NH<sub>3</sub>) gases (Fig. 3-2B). The low-cost, extremely small size, and sensitivity of this device offers great promise toward the development of a low-cost solid-state pH sensor device.

### 3.3 EXPERIMENTAL

**Materials:** Pristine single-walled carbon nanotubes (SWNTs) were purchased from Carbon Solutions, Inc (P2). 1-aminoanthracene (AA), anhydrous acetonitrile (MeCN) and FeSO<sub>4</sub>·7 H<sub>2</sub>O powder and were obtained from Sigma Aldrich. Tetrabutylammonium perchlorate (TBAP) was prepared from the reaction of tetraalkylammonium bromide (Sigma Aldrich) and HClO<sub>4</sub>. The reaction product was recrystallized four times and dried under vacuum at room temperature overnight. Phosphate buffers solutions were prepared from combinations of 0.01 M K<sub>2</sub>HPO<sub>4</sub>, 0.01 M KH<sub>2</sub>PO<sub>4</sub>. The pH was then adjusted with 1M HCl or 1M KOH and the ionic strength was adjusted with 0.13 M KCl. The pH of the buffered solution was measured using a Mettler Toledo

SevenGo SG2 pH meter. The pH meter was calibrated with standard buffered solutions obtained from J. T. Baker.

**Chemical oxidative polymerization of 1-aminoanthracene (AA):**<sup>66</sup> To a solution of AA (27 mg, 0.14 mmol) in CH<sub>3</sub>CN (8 mL), distilled water (8 mL) and sulfuric acid (68 μL, 1.2 mmol) were added dropwise. With the resulting solution was stirred at 30 °C, FeSO<sub>4</sub>·7 H<sub>2</sub>O powder (1 mg, 3.6 μmol) was added, followed by the slow addition of 30% H<sub>2</sub>O<sub>2</sub> (50 μL). The reaction mixture was stirred continuously for 48 hours under air at 30 °C to cause precipitation of a brown solid. After quenching with ice water, the solid was collected on a membrane filter and washed with methanol, 28% aqueous ammonia, and methanol again. The solid was then dried in vacuum at room temperature to give poly(1-aminoanthracene) (PAA) as a brown solid in 90% yield. Gel permeation chromatography (GPC) analysis using polystyrene standards in THF indicated that there are 198 average repeating units in the PAA polymer main chain ( $M_w = 3.8 \times 10^4$  g/mol and PDI = 1.12). GPC was performed on a Waters Gel Permeation Chromatography system equipped with a Waters 510 HPLC pump, phenogel columns, and a Waters 410 Differential Refractometer at a flow rate of 0.4 mL/min.

**Preparation of conductive carboxylated SWNTs:** SWNTs were dispersed in 20 mL of concentrated H<sub>2</sub>SO<sub>4</sub>/HNO<sub>3</sub> (3:1). The mixture was subsequently sonicated for 2 hrs at 40 °C in an ultrasonic bath (5510 Brasonic) to yield oxidized SWNTs (o-SWNTs) with lengths around 500 nm. Carboxylic acid groups were confirmed through FTIR spectroscopy. FT-IR spectra were recorded as thin films on KBr pellets on an Avatar 380 Nicolet FI-IR spectrometer. Upon completion, the mixture was added dropwise to 100 mL of cold distilled water, and then filtered through 0.2-μm pore size PTFE (Teflon) laminated filter paper, and then washed with water until no residual acid was present.

**Sensor Device Fabrication:** Silicon chips with 300 nm thermal oxide layer and pre-fabricated interdigitated Au electrodes (MEMS and Nanotechnology Exchange) were wire-bonded into a 40-pin CERDIP package, followed by passivation of the system with epoxy (EPO-TEK, Epoxy Technology, MD USA). Aqueous suspensions (0.3  $\mu\text{L}$ ) of o-SWNTs in N,N-dimethylformamide (DMF) were dropcast onto the Si chips and allowed to dry in ambient. PAA was subsequently added to the o-SWNT network *via* Electropolymerization (EP) of the monomeric units, AA, into the polymer, PAA.<sup>67</sup> EP was performed with a CH instruments electrochemical analyzer with o-SWNTs configured as the working electrode in a three-electrode single compartment electrochemical cell. A platinum wire and a Ag/AgCl quasi-reference electrode were used as the auxiliary and reference electrodes, respectively. Anhydrous acetonitrile was used as the electrolyte solution which contained the supporting electrolyte, TBAP (0.1 M), and the monomeric units, AA (1 mM). PAA was prepared on the o-SWNT film using cyclic voltammetry by sweeping the electrode potential between 0 and + 0.8 V at rate of 0.05 V/s. 24 hr prior to testing, the electrodes were conditioned in an aqueous solution containing a phosphate buffer (pH = 5.60). The formation as well as morphology of PAA was characterized through scanning electron microscopy (SEM). SEM was performed on a Philips SL30 FEG microscope at an accelerating voltage of 10 keV.

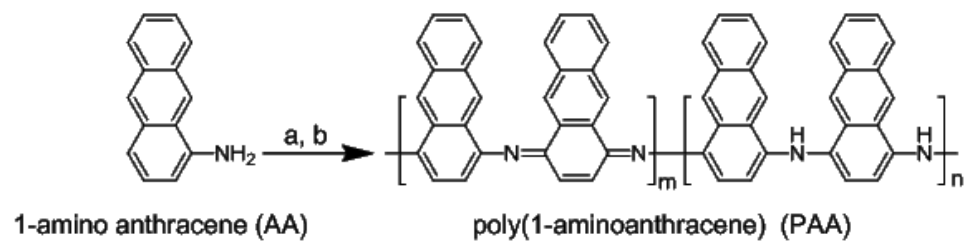
**Electrical Measurement:** For pH-solution sensing, devices fabricated as explained above were modified with a custom Teflon flow cell powered by a variable flow mini-pump at a rate of 0.205  $\text{cm}^3/\text{min}$ . A Teflon cube, attached with silicone to the CERDIP package through silicone rubber sealant, was used to expose the device to varying buffered pH solutions, while simultaneously keeping the buffered pH solutions in a closed system. Conductance of the nanotube network was measured at a constant voltage ( $V_{\text{SD}}$ ) of 50 mV, and were taken with a

Keithley 2400 source meter. Specifically the conductance through the nanotube network was determined by measuring the current at a constant bias voltage of 50 mV.

**Spectroscopic Measurement:** UV-vis-NIR absorption spectra studies were taken by a Perkin-Elmer Lambda 900 UV-vis-NIR spectrophotometer. In the case of thin film measurements, an Iwata HP-BC Plus airbrush was used to spray a DMF suspension of o-SWNT onto a 1" × 1" quartz plate at 180°C. PAA in THF was added to the SWNT network *via* spincoating and dried in ambient.

### 3.4 RESULTS AND DISCUSSION

The PAA polymer was synthesized following a published procedure.<sup>66</sup> The AA monomeric units were homogeneously dissolved in acetonitrile (MeCN), and with addition of H<sub>2</sub>O<sub>2</sub> in the presence of catalytic FeSO<sub>4</sub>, the brown solid PAA polymer was formed in 90 % yield (Scheme 3-1). The polymer was characterized using GPC and indicated an average molecular weight as 198 repeating units in the PAA polymer main chain. To study the interactions between PAA polymer and SWNTs as well as the response of the material to different pH solutions, a solution of PAA in THF was spincoated onto a network of previously deposited o-SWNTs. PAA is a polymer very close in structure to polyaniline (PANi), having an anthracene group instead of benzene. For this reason it is expected that PAA and SWNT will have stronger interactions than PANi/SWNT due to  $\pi$ - $\pi$  stacking, which can be observed through UV-Vis-NIR spectroscopy. PANi interactions with SWNT have been heavily studied and well documented<sup>33,68</sup> and will serve as a good comparison to the research conducted in this report.



**Scheme 3-1.** Synthesis of poly(1-amino anthracene ) (PAA)

Synthesis of poly(1-amino anthracene ) (PAA) from 1-amino anthracene (AA). a)  $\text{H}_2\text{O}_2$ ,  $\text{Fe}^{2+}$ ,  $30^\circ\text{C}$ ; b)  $\text{NH}_4\text{OH}$ .

Adapted from Reference 66.

UV-vis-NIR absorption spectroscopy was chosen to investigate the interaction of PAA polymer with o-SWNTs as well as the response of PAA/o-SWNT to acidic and basic vapors (Figure 3-1). UV-vis-NIR proves a useful technique to probe electron transfer in SWNTs,<sup>69,19,55</sup> as SWNTs have a unique electronic structure with several van Hove singularities.<sup>70</sup> A density of states (DOS) diagram of metallic and semiconducting SWNTs is depicted in Figure 3-1B specifically showing the transition bands of the two types of SWNTs. Electronic transitions between corresponding singularities in the valence band (VB) and the conduction band (CB) result in absorption bands observed in the UV, visible, and NIR regions of the electromagnetic spectrum (Figure 3-1A). A solid film was necessary in order to monitor the S<sub>11</sub> electronic transition, the most sensitive transition band as it corresponds to the top of the valence band. The film was produced by first spraycoating o-SWNTs from a solution of dimethylformamide (DMF) onto a quartz plate followed by spincoat deposition of the polymer from a solution of tetrahydrofuran (THF). Figure 3-1A shows the entire range of the UV-Vis-NIR absorption spectra of an o-SWNT film (blue), a PAA/o-SWNT film (red), and the response of the PAA/o-SWNT film to acidic (HCl) and basic gases (NH<sub>3</sub>). A comparison of the optical properties of o-SWNT film to that of the polymer coated film shows a distinct red shift in both the S<sub>22</sub> and S<sub>11</sub> electronic transitions, and an increased S<sub>11</sub>/S<sub>22</sub> ratio (S<sub>11</sub>/S<sub>22</sub> = 1.37) over bare o-SWNT film (S<sub>11</sub>/S<sub>22</sub> = 1.15). The red shift is indicative of the attachments of PAA to the o-SWNT surface through noncovalent interactions.<sup>42,71</sup> The enhancement in S<sub>11</sub>/S<sub>22</sub> ratio suggests the electron donation to valence band of semiconducting SWNT. Figure 3-1C demonstrates how the device's spectrum changes when it is exposed to NH<sub>3</sub> and HCl gas. A significant change in the intensity of the S<sub>11</sub> transition was observed for the exposure of such proton donating/withdrawing gases (Brønsted-Lowry acids/bases). Specifically there was an increase in absorption for NH<sub>3</sub> gas and a

decrease in absorption for HCl gas. A change in the  $S_{11}$  transition band has been attributed to the amount of electrons added to or removed from the nanotube network.<sup>17</sup> Specifically, a decrease in the  $S_{11}$  absorbance (which corresponds to an increase in conductance *vide infra*) can be attributed to electrons being removed from the partially filled SWNT valence band. Importantly, the device absorption recovers fully when HCl is purged and  $NH_3$  reintroduced (Figure 3-1C)

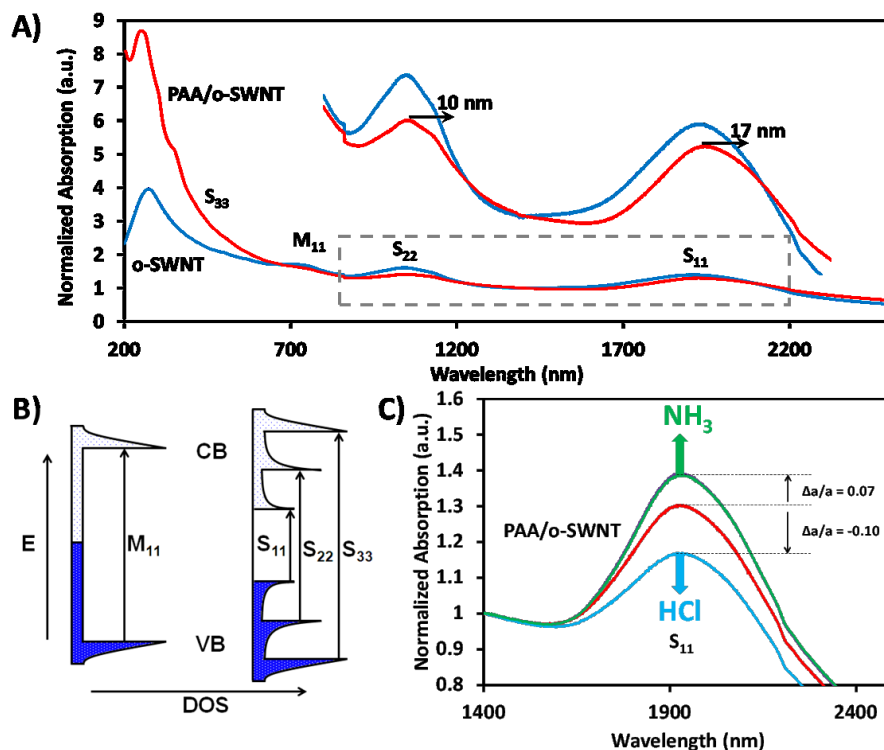


**Figure 3-1.** Optical measurements of PAA/o-SWNT film

A) UV-Vis-NIR absorption spectra of an o-SWNT film (blue) (spraycast from solution onto a quartz plate) and a PAA/o-SWNT film (red) (spincoat from solution onto the quartz plate). Inset: magnification of the spectra showing red shifts of the S<sub>11</sub> and S<sub>22</sub> bands. The red shifts observed are indicative of noncovalent interactions between PAA and nanotubes. B) Density of states (DOS) diagram showing the transition bands of metallic and semiconducting SWNTs. C) Optical response of the PAA/o-SWNT film to acidic (HCl) and basic (NH<sub>3</sub>) gases. The S<sub>11</sub> electronic transition reveals a significant decrease in absorption for the acidic gas and an increase for the basic gas.

Configuring the device as a chemiresistor allows for direct real-time electrical measurements of the system as a function of analyte as well as analyte concentration. A chemiresistor is a device that changes resistance upon exposure to an analyte of interest. The PAA/o-SWNT can be integrated easily into such a device by depositing o-SWNTs on top of a Si/SiO<sub>2</sub> chip containing interdigitated gold electrodes, followed by electropolymerization (EP) of PAA on o-SWNTs. The formation of PAA has been confirmed by scanning electron microscopy (SEM). An image of an EP prepared device after 30 CV cycles is given in Fig 3-2B showing the morphology of the polymer. A higher magnification image (below) reveals o-SWNTs that are not connected to the nanotube network. Since these o-SWNTs were not connected to the “W.E.” no polymer was deposited onto them. First, o-SWNTs in DMF are dropcast onto the chip and dried in ambient, followed by formation of PAA *via* electropolymerization (EP). Figure 3-2A depicts a typical device setup for EP of aminoanthracene (AA) to poly(1-aminoanthracene) (PAA).<sup>67</sup> In this three electrode electrochemical cell, a network of oxidized single-walled carbon nanotubes (o-SWNTs) is used as the working electrode (W.E.). The potential of the W.E. is varied with respect to a quasi-reference electrode (R.E.) (Ag/AgCl), while the Pt wire auxiliary electrode (A.E.) is used to monitor the current produced without changing the potential of the R.E. By sweeping the potential of the working electrode while the system is submerged into an electrolyte solution (TBAP in MeCN) containing AA monomeric units, PAA is formed. More specifically by sweeping the potential between 0 to + 0.8V at a sweep rate of 0.05 V/s, one cyclic voltammetry (CV) cycle is completed, and thus formation of PAA. The resulting current, plotted *versus* potential in Fig 2C, tells us information about the EP process. With an increase in the number of cycles from 1 (red) to 30 cycles (purple), peaks for the oxidation of the monomeric

unit (A1) decrease in amplitude and the peaks for dimer and oligomer units (A2) increase in amplitude.

By holding the voltage passing through the o-SWNT network ( $V_{SD}$ ) constant and measuring the resulting current ( $I_{SD}$ ) as a function of analyte, the sensitivity of the chemiresistor to various analytes can be determined with relative ease. A custom-built Teflon flow cell was fabricated on top of the sensor device in order to facilitate the flow of various solutions over the device, while simultaneously maintaining a steady-state diffusion of hydronium ions (Figure 3-3D). Figure 3-3A presents a conductance *versus* time plot for a PAA/o-SWNT device ( $V_{SD}$ ) showing response to buffered solutions from pH = 2 to pH = 12. An increase in conductance is observed for increasing amounts of  $H_3O^+$  ion (Brønsted-Lowry acid) which is in agreement with the optical measurements discussed above. Specifically increasing the amount of  $H_3O^+$  ions in solution withdraws electrons from the partially filled SWNT VB increasing the electrical conductivity. Furthermore, plotting the relative response ( $\Delta G/G_0$ ) of the device *versus* pH (Figure 3-3B) reveals a linear calibration curve with very little variance ( $R^2 > 0.99$ ). This scaling relationship between response and pH is necessary toward development of a sensor device, and the deviation between the responses from 12 to 2 and that from 2 to 12 is minuscule (most error bars are smaller than the markers themselves). The PAA coated o-SWNT electrodes were robust as even 8 days after fabrication and initial testing, the device characteristics have not significantly degraded (Fig 3-4A).

Control experiments were performed in order to further evaluate sensor performance and elucidate the mechanism of detection. In order to determine that the functionalization platform is specific to hydronium ions,  $Ca^{2+}$  and  $Na^+$  were tested as control analytes (Figure 3-4B). The PAA/o-SWNT device did not respond to concentrations of such ions in the range of  $10^{-12}$  to  $10^{-6}$

M, comparable to the range of concentrations of  $\text{H}_3\text{O}^+$  ions tested. Pristine SWNTs functionalized with PAA *via* EP resulted in a platform not sensitive to pH (Figure 3-4C), leading to the conclusion that oxidation of SWNTs is required. It is hypothesized that the carboxylate groups on the surface of o-SWNT are required for attachment of the polymer to the nanotube *via* hydrogen bonding. Additionally, o-SWNT without the PAA layer are sensitive to pH, however, the response is very small and shows relatively large noise, implying the enhancement of electrical signal by PAA coating (Figure 3-4D). Previous experiments suggest a mechanism based on intercalation of  $\text{H}^+$  ions into the SWNT bundle, diffusion of  $\text{H}^+$  inside the tubes, or protonation of carboxylate groups.<sup>58</sup>

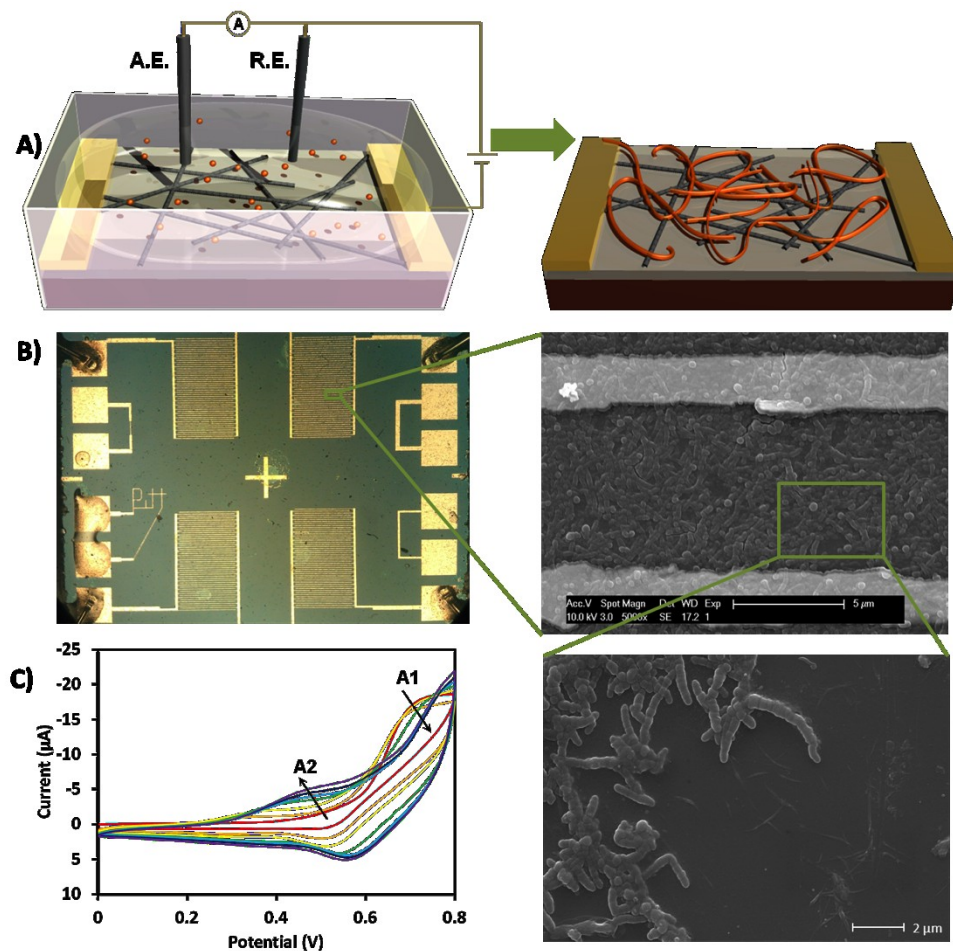


**Figure 3-2.** Device fabrication and characterization of PAA/o-SWNT

A) Generalized schematic of electropolymerization (EP) of poly(1-aminoanthracene) (PAA) onto oxidized single-walled carbon nanotubes (o-SWNTs) using the nanotube network as the working electrode (W.E.) accompanied by a Ag/AgCl quasi reference electrode (R.E.) and a Pt wire auxiliary electrode (A.E.). The whole system was submersed into an electrolyte solution (TBAP in MeCN) containing the aminoanthracene (AA) monomeric units (represented by the orange spheres). Performing cyclic voltammetry (CV) results in formation of PAA, and after removal of the liquid cell, the device is ready for testing. B) Microscopy images of a typical devices (after 30 CV cycles). Scanning electron microscopy (SEM) images depict the morphology of the polymer formed. A higher magnification image (below) shows some SWNTs not connected to the network, without polymer coating. C) Cyclic voltammetry of EP of PAA onto o-SWNT. As the number of cycles increase, from 1 (red) to 30 cycles (purple), the oxidation peaks for the AA monomeric unit (A1) disappear and the peak for PAA (A2) appear.

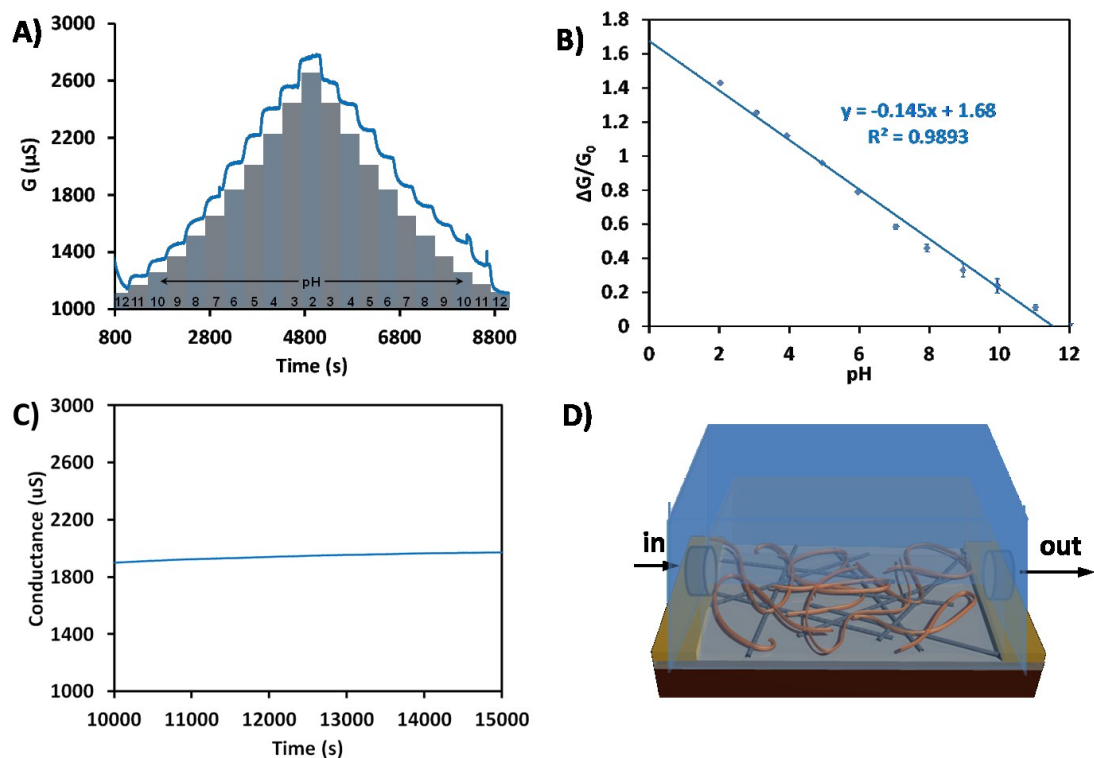


**Figure 3-3.** Electrical measurements of PAA/o-CNT

A) Conductance vs. time for PAA/o-CNT (18 cycles) for pH from 12 to 2 and back to 12 (increments of 1 pH unit). An increase in conductance is observed for increasing amounts of protons in solution, which is in agreement with absorbance measurements. B) A relative response plot of the device in A shows that the response over the given pH range and has very little variance ( $R^2 > 0.99$ ). C) Stability of the device over in a buffered solution (pH = 7) for more than two hours. D) Schematic illustration of custom-built Teflon flow cell fabricated on top of the sensor device.

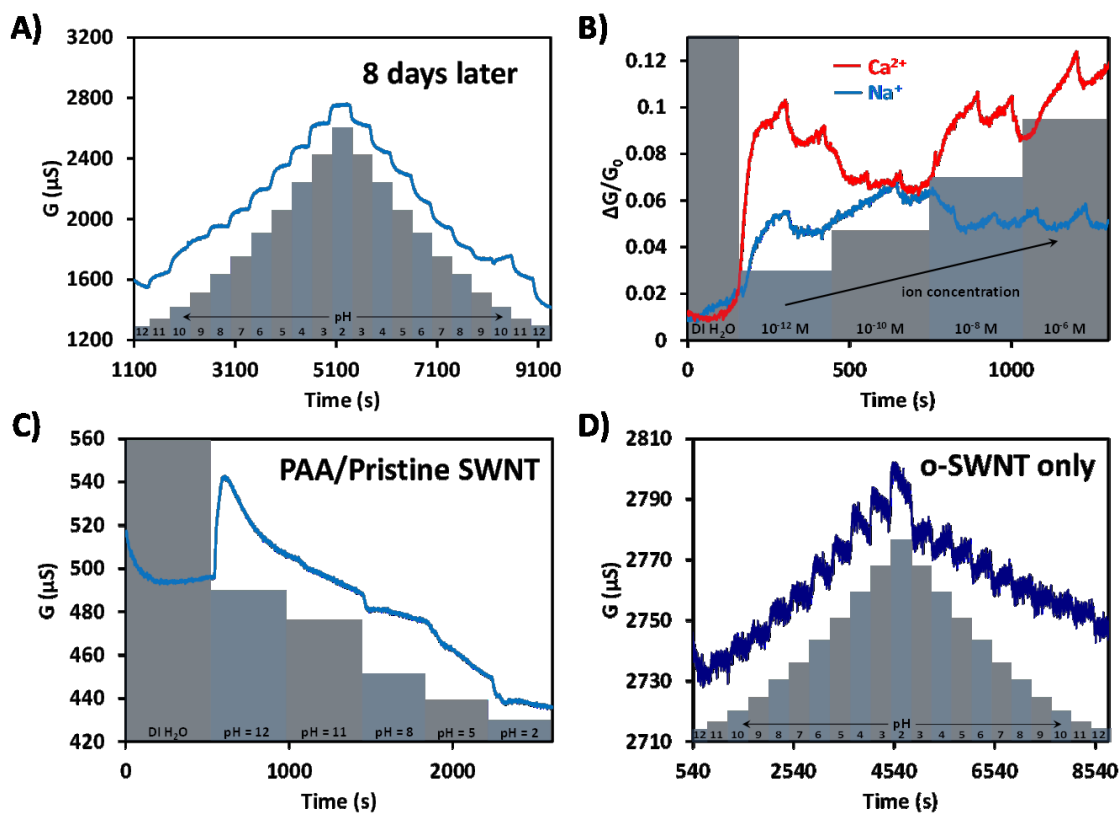
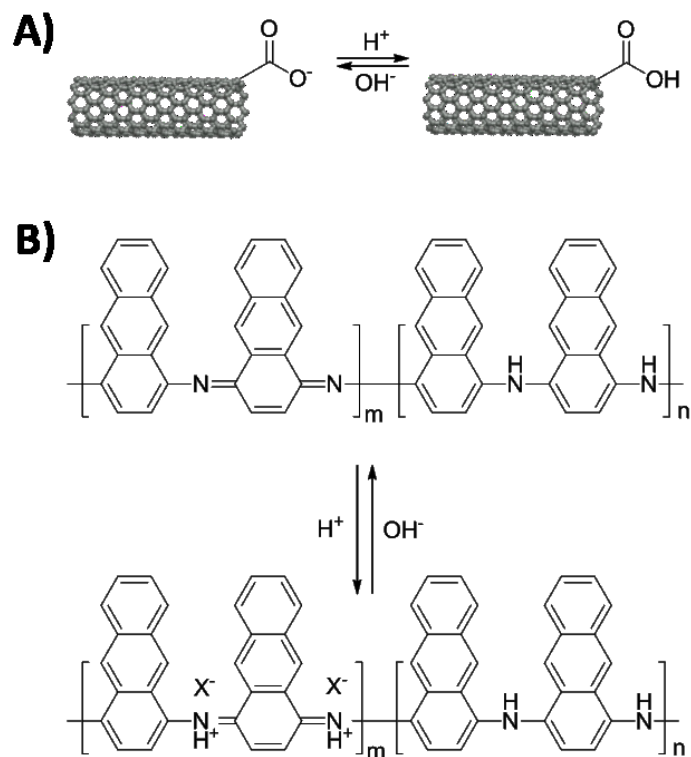


**Figure 3-4.** Additional/Control experiments for PAA/SWNT

A) Conductance ( $G$ ) vs. time of PAA/o-CNT 8 days after original test (Figure 3A). B) Cross sensitivity tests for the response of PAA/o-CNT (PAA dropcast from solution) to  $\text{Ca}^{2+}$  and  $\text{Na}^{+}$  ions. The response was negligible. C) Response of PAA/pristine-SWNTs to pH. D) Response of o-SWNT (no PAA) to pH.

Scheme 3-2 depicts the mechanism of detection of pH for o-SWNT and PAA separately. As seen in Scheme 3-2A, by increasing the concentration of  $H^+$  ions in solution the carboxylate groups ( $-COO^-$ ) of the SWNT get protonated. The pH response of PAA coated o-SWNTs is primarily related to the PAA conductivity. Due to the similarities of PAA and PANi, looking at the mechanism of pH detection of PANi can provide insight into the detection mechanism for PAA. PANi pH sensitivity is attributed to the reversible acid/base doping of the polymer which exhibits a measurable effect on the electrical properties of the polymer.<sup>72</sup> Specifically, acid doping of PANi consists of the addition of a proton and a counter ion for every imine nitrogen in the polymer backbone, causing a significant increase in the conductivity of PANi. This is in agreement with the electrical results obtained from PAA in this report.

Table 3-1 summarized the effect of the number of CV cycles on the sensitivity of the device to pH. Sixty cycles does not show any response to pH due to the thickness of the polymer layer. It is important to note that the number of CV cycles is relatively arbitrary, as the dropcast o-SWNT network is difficult to control and thus varies quite largely (i.e. affecting the W.E.).



**Scheme 3-2.** Proposed mechanism of detection pH for pAA and SWNT

A) Upon addition of  $H^+$  to o-SWNT, the oxygen in the COOH group gets protonated. B) Upon addition of  $H^+$  to PAA, the imine (C=N) group gets protonated.

**Table 3-1.** Summary of the effect of the number of CV cycle on the sensitivity of the devices

Number of Cycles	Sensitivity
0	-0.0019 ± 0.0004
10	No response
18	-0.145 ± .002
20	-0.025
30	-0.194
40	-0.214
60	No response

## 4.0 BIOSENSORS BASED ON CARBON NANOTUBES FOR METAL ION DETECTION

### 4.1 INTRODUCTION

#### 4.1.1 Carbon nanotubes as biosensors

SWNTs have several significant advantages for biosensing applications: (1) Their diameters are comparable to the size of biological species; (2) they have every atom located on the surface, which makes them highly sensitive to changes in their local chemical environment;<sup>73</sup> (3) they are micrometer in length so they can be integrated in micrometer-scale electronic devices; and (4) their electrical properties offer a platform for electronic detection of electrostatic interactions and charge transfer that commonly occur in biosensing.

Two common SWNT-based electronic devices were applied for direct electrical detection of biomolecules: chemiresistor<sup>42,46 74 , 75</sup> and field-effect transistor (FET).<sup>76 , 77 ,32</sup> In both configurations SWNTs form the conducting channel connecting the source (S) and drain (D) electrodes (Figure 4-1). The interaction between biomolecules and SWNTs can induce changes in electronic properties of SWNTs, thus appearing as conductance change of the devices.

For SWNT-based FET (NTFET) devices, two typical gating configurations are employed: backgate configuration (Figure 4-1) and liquid-gate configuration (Figure 4-2). In the

first configuration, conductive Si is used as a bottom-gate, and separated from a conducting channel of SWNTs by a thin insulating SiO<sub>2</sub> layer. However, the source-drain current of this device can be influenced by the screening effect of species bound on SiO<sub>2</sub>, thus reducing the signal. In the second configuration, the whole device is immersed in a buffer electrolyte solution. The reference electrode is to calibrate the gating potential, while at the same time a source-drain current is achieved by setting the source and drain electrodes at a constant bias voltage and sweeping the gate voltage ( $V_G$ ) between positive and negative values.

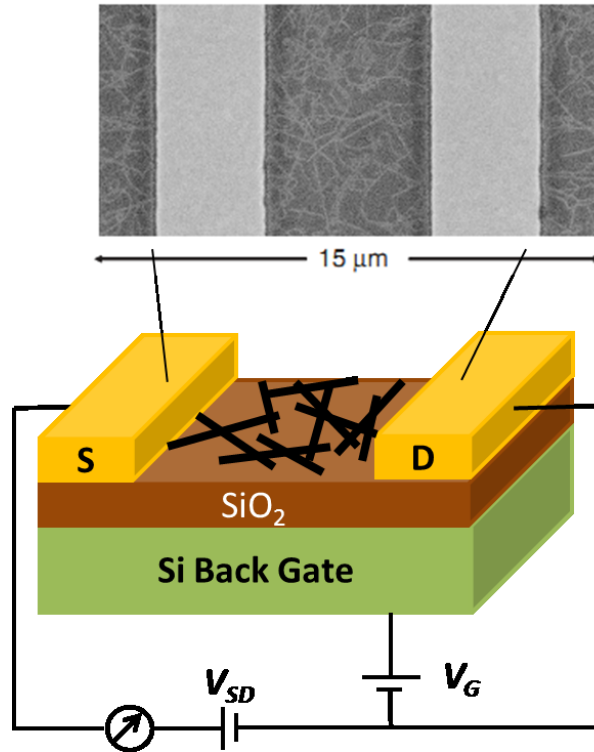


**Figure 4-1.** Schematic representation of a back-gate nanotube field-effect transistor (NTFET) device

The device with SWNTs (black) contacted by source (S) and the drain (D) electrodes (light brown), and a Si back gate (green), separated by a SiO<sub>2</sub> insulating layer (dark brown) in a transistor-configured circuit. Enlarged image is scanning electron microscopy (SEM) image of a typical NTFET device consisting of a random array of carbon nanotubes.

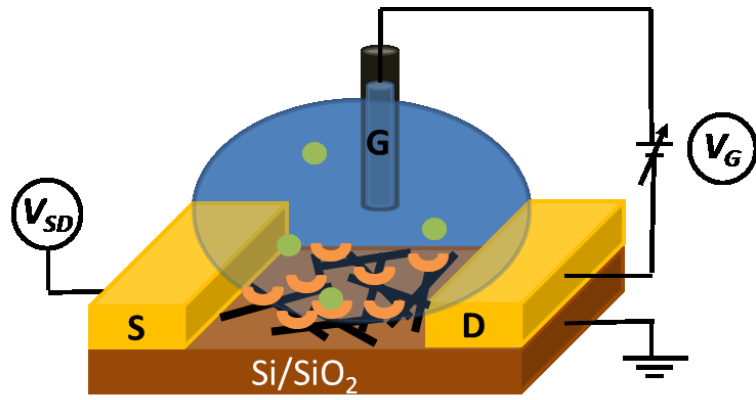


**Figure 4-2.** Schematic illustration of detection in liquid with functionalized NTFET by using liquid gate configuration

### **4.1.2 Interactions between Carbon Nanotubes and Protein Molecules**

The interaction between carbon nanotubes and protein molecules can primarily be described as non-specific. Hydrophobic interactions are widely thought to contribute to the adsorption of aromatic species onto the surface of carbon nanotubes. However, non-specific adsorption is more complicated. Recently, it was demonstrated that protein adsorption is related to the amino affinity of carbon nanotubes.<sup>78</sup>

Basically, the effects of proteins on nanotubes' conductance may have two types of mechanism. The first involves charge transfer from charged biomolecules to the carbon nanotubes. The second is attributed to scattering potential developing across the carbon nanotube because of the protein adsorption. These two mechanisms can be distinguished by FET measurements.<sup>79</sup> In a charge transfer mechanism, the resulting threshold voltage will be shifted to more positive values by electron withdrawing species, or to more negative values by electron donating species. While in a scattering mechanism, an overall drop in conductance may be observed, due to protein adsorbed on the sidewalls of SWNT. In addition, the adsorbed species at metal contacts or nanotube-metal contact interfaces can modulate the metal work functions and thus the Schottky barrier.<sup>80</sup> However, the exact mechanism of biodetection using NTFET is complicated and may involve a combination of all mechanisms discussed above.

### **4.1.3 NTFET fabrication**

NTFET devices were fabricated by patterning interdigitated microelectrodes (source-drain electrode spacing of 10  $\mu\text{m}$ ) on top of a 200 nm oxide layer on Si substrates using photolithography and e-beam evaporation of 30 nm Ti and 100 nm of Au. Three kinds of

SWNTs were used to fabricate FET. Pristine SWNTs and carboxylated SWNTs (P3-SWNTs) were purchased from Carbon Solutions Inc, o-SWNTs were obtained by sonication of SWNTs in a mixture of concentrated  $\text{H}_2\text{SO}_4/\text{HNO}_3$  (3:1) acids for 2h, which was detailed above. o-SWNTs and P3-SWNTs were dropcasted on Si chip with interdigitated gold electrodes; pristine SWNT networks were deposited on FET by dielectrophoresis (DEP) technique from N,N-dimethylformamide (DMF) suspension. Two Keithley 2400 sourcemeters were used for FET measurements. The electrical performance of each device was investigated in an electrolyte gated FET device configuration. The conductance of the NTFET device was tuned using the electrolyte as a highly effective gate. A small chamber was placed over the NTFET device to control the liquid environment with buffer solution. A liquid gate potential (-0.75 to +0.75 V) was applied using an Ag/AgCl (3 M KCl) reference electrode submerged in the electrolyte. The source-drain current of the device was measured at a constant source drain voltage of 50 mV. Transfer characteristics (i.e., source-drain conductance (G) vs gate voltage ( $V_g$ )) were measured to investigate the interactions between analytes and carbon nanotubes.

## 4.2 CALMODULIN MODIFIED SWNTS FOR DETECTION OF CALCIUM IONS

### 4.2.1 Introduction

Calcium ( $\text{Ca}^{2+}$ ) is recognized as an important intracellular second messenger in response to extracellular stimuli. Within a typical cell, the intracellular  $\text{Ca}^{2+}$  concentration is roughly 100 nM,<sup>81</sup> which contains  $\sim 60$   $\text{Ca}^{2+}$  ions. Increase in the cytoplasmic  $\text{Ca}^{2+}$  concentration induces binding of  $\text{Ca}^{2+}$  by intracellular regulatory proteins, thus initiating a wide variety of cellular processes.<sup>82</sup> A  $\text{Ca}^{2+}$ -dependent regulatory protein, calmodulin (CaM) is a small (148 amino acids), acidic protein consisting two globular domains connected by an extended linker.<sup>83</sup> When the intracellular calcium level rises to  $10^{-5}$  M, four  $\text{Ca}^{2+}$  ions bind to calmodulin, two each in the N-terminal and C-terminal lobes (Figure 4-3).

Calmodulin contains two pair of EF-hand motifs that resemble the spread thumb and forefinger of the human hand in helix-loop-helix topology, and change conformation upon binding  $\text{Ca}^{2+}$ .<sup>84</sup> Each EF-hand motif has two  $\alpha$ -helices connected by a 12-residue loop. In the absence of  $\text{Ca}^{2+}$ , the  $\alpha$ -helices in the EF-hand motif are positioned almost parallel to each other, known as a “closed” conformation (Figure 4-3a). As  $\text{Ca}^{2+}$  binds to the loop region,  $\alpha$ -helices of the EF-hand motifs change their position relative to each other, forming a dumbbell shape, also known as an “open” conformation (Figure 4-3b).<sup>83,85</sup>

The most interesting feature of CaM is its large conformational changes from closed to open form, which induces the opening of the solvent accessible hydrophobic surface. This  $\text{Ca}^{2+}$ -induced conformational transition was confirmed by Zheng *et al* using NMR and X-ray method.<sup>83</sup> A large solvent-exposed hydrophobic surface is located in both domains of  $\text{Ca}^{2+}$ -CaM. Each hydrophobic surface is surrounded by a polar rim which is rich in negative charges. The

center of each surface has a deep hydrophobic cavity that is ready for capturing an aromatic or long aliphatic side chain of the target proteins. Thus in the open form, the extensive hydrophobic interactions and electrostatic interactions could occur simultaneously between  $\text{Ca}^{2+}$ -CaM and target proteins. This central deep hydrophobic cavities is completely absent in  $\text{Ca}^{2+}$  free-CaM, or apo-CaM, resulting in a negatively charged but a partially hydrophobic surface in apo-CaM.

In this work, we show that CaM-modified NTFET can be used to detect  $\text{Ca}^{2+}$  ions, and monitor changes in the interaction between CaM and SWNTs.

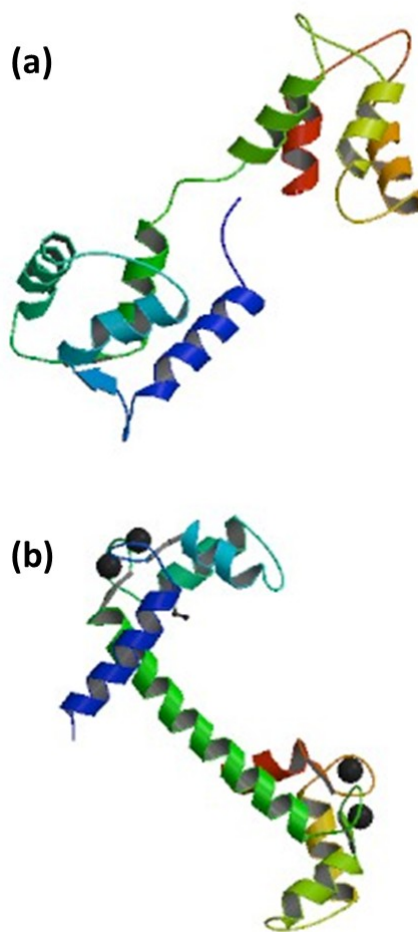


**Figure 4-3.** Structure of apo CaM and  $\text{Ca}^{2+}$ -CaM

(a) apoCaM, protein data base (PDB) ID = 1CFD, and (b)  $\text{Ca}^{2+}$ -CaM PDB ID =1CCLL

## 4.2.2 Experimental

NTFET devices were fabricated with high defect o-SWNT. For real-time conductance measurements, o-SWNT and pristine SWNTs were drop-cast on Si chips with interdigitated gold electrodes, respectively; electrical conductance of the chips was monitored with Keithley 2602 SourceMeter.

Both types of devices were functionalized with CaM. Briefly, surface functionalization of SWNTs with CaM was performed by incubating the Si chips with 500  $\mu\text{g/mL}$  CaM in HEPES (10mM, pH = 7) for 1 h at room temperature, followed by rinsing with deionized water.

$\text{Ca}^{2+}$  solutions were made from  $10^{-3}$ - $10^{-7}$  M in HEPES (10mM pH=7)/KCl (10mM).  $\text{Zn}^{2+}$  solution ( $10^{-4}$  M) in same buffer solution was used as control. The functionalized NTFET chips were incubated for 10 min in different concentrations of metal ion solutions and later washed three times with DI water.

## 4.2.3 Result and Discussion

### FET Study

The liquid gate FET measurements of bare NTFETs exhibited p-type transfer characteristics (Figure 4-4). The ON/OFF ratio of the device was below  $10^2$  due to the presence of metallic SWNTs in the networks. After functionalization with the CaM, the conductance was increased with positive shift in gate voltages (Figure 4-4). This observation demonstrated the adsorption of CaM on the surface of SWNTs. Known as an acidic protein (pI  $\sim$  3.9-4.3),<sup>86, 87</sup> apo-CaM was negatively charged in buffer solution (pH = 7.4). Thus adsorption of a negatively charged apo-CaM caused electrostatic gating to SWNT by inducing additional positive charge in the SWNT,

thus p-doping the SWNT and shifting the  $I-V_g$  curve toward more positive gate voltages.<sup>88</sup> To study selectivity, the CaM-functionalized devices were treated with  $Ca^{2+}$  ions and  $Zn^{2+}$  ions as the control. When treated with  $Ca^{2+}$  ( $1\mu M$  in HEPES), a decrease in ON conductance was observed. While treated with  $Zn^{2+}$  at 100 times higher concentration ( $0.1\text{ mM}$  in HEPES), the transfer characteristics remained unaffected, indicating excellent selectivity between  $Ca^{2+}$  and  $Zn^{2+}$  ions. The selectivity can be explained by conformational change of CaM. Binding of  $Ca^{2+}$  triggered exposure of the hydrophobic cavity in both domains to the surface of the SWNTs, thus enhanced  $\pi$ - $\pi$  interactions between protein and SWNTs induced a drop in conductance by the scattering mechanism. On the other hand,  $Zn^{2+}$  had no effect on the conformation of CaM, resulting in an undisturbed  $I-V_g$  curve.

Additionally, the sensitivity of NTFET devices was investigated by plotting the  $G$  vs  $V_g$  for CaM functionalized devices at different concentrations ( $0.1\ \mu M$  to  $1\text{ mM}$ ) of  $Ca^{2+}$  ions (control measurements with  $0.1\text{ mM}$   $Zn^{2+}$ ) (Figure 4-4). The decrease in conductance was recorded with increasing concentrations of  $Ca^{2+}$  ions. In addition to increased hydrophobic interactions, increased electrostatic gating by binding positively charged  $Ca^{2+}$  ions may contribute to the observed drop in conductance.

Figure 4-5 shows that the response  $\Delta G/G_0$  of the CaM/NTFET increased with the log of  $Ca^{2+}$  concentration, and this concentration dependence was linear in the range of  $0.1\ \mu M$  –  $1\text{ mM}$ . The NTFET response to the lowest concentration ( $0.1\ \mu M$ ) of  $Ca^{2+}$  was higher than the response to  $0.1\text{ mM}$  of the control  $Zn^{2+}$ , demonstrating excellent selectivity. The detection limit of NTFET devices was comparable to other techniques traditionally used for  $Ca^{2+}$  detection such as flame emission ( $1.75\ \mu M$ ), inductively coupled plasma (ICP) ( $0.15\ \mu M$ ), ion chromatography ( $0.025\ \mu M$ ), and inductively coupled plasma-mass spectrometry (ICPMS) ( $0.02\ \mu M$ ).

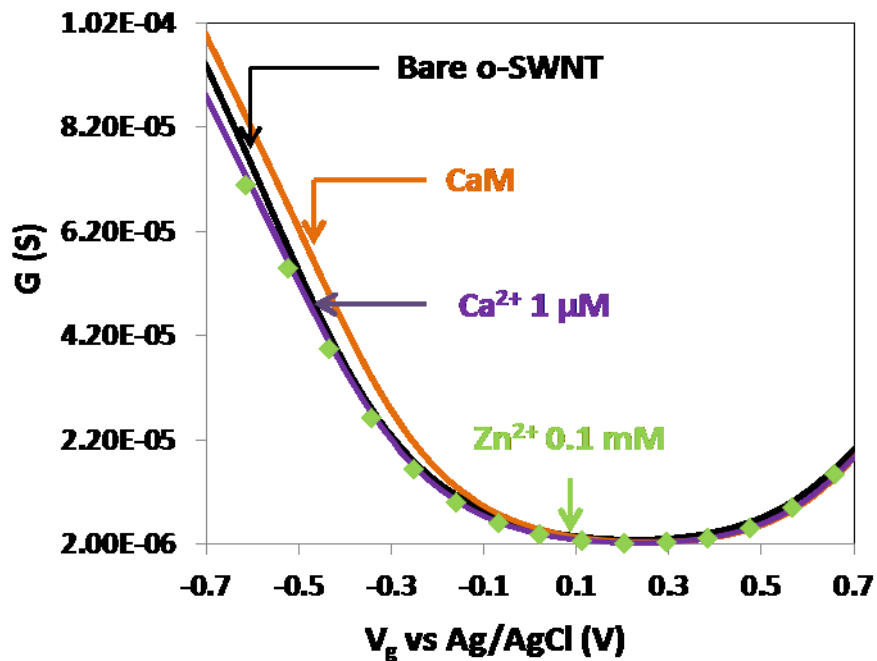


**Figure 4-4.** Electronic detection of Ca<sup>2+</sup>-CaM interactions on NTFET device

Conductance (G) vs gate voltage ( $V_g$ ) of bare NTFET device (black line) after functionalization with CaM (orange line), and after addition of 1  $\mu$ M Ca<sup>2+</sup> (purple line) and the control Zn<sup>2+</sup> (green dots).

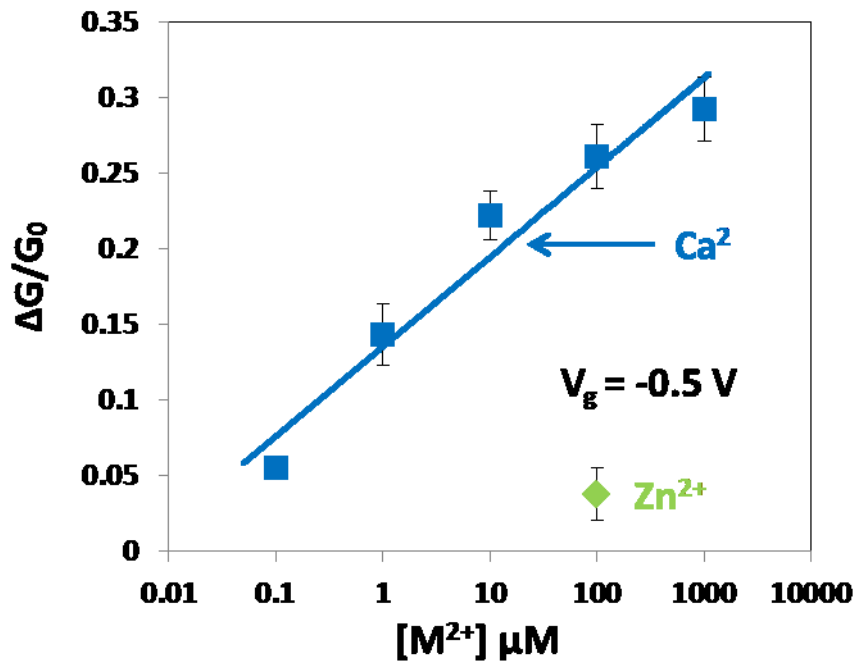
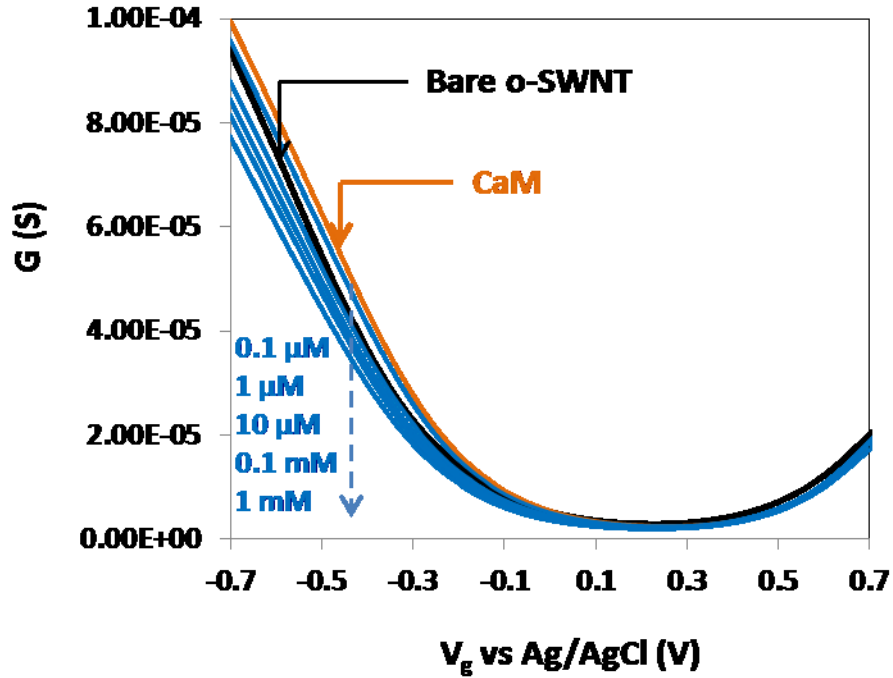


Figure 4-5. Sensitivity study with  $\text{Zn}^{2+}$  as control on CaM-modified NTFET devices

Sensitivity study with  $\text{Zn}^{2+}$  as control and varying concentration of the  $\text{Ca}^{2+}$  ( $0.1 \mu\text{M}$  to  $1 \text{mM}$ ). (Top) NTFET characteristics and (bottom) the biosensor calibration plot: normalized change in the device conductance versus metal ion concentrations.

## Conductance Measurements

The real-time detection of  $\text{Ca}^{2+}$ -CaM interactions was performed by pumping  $\text{Ca}^{2+}$  solutions with varying concentrations (1  $\mu\text{M}$  to 0.1 mM) to CaM functionalized NTFET covered by a chamber. The signal was recorded as a plot of conductance versus time, and conductance of  $\text{Ca}^{2+}$ -free HEPES buffer was set as  $G_0$ . Figure 4-6 showed the same response as the liquid-gate NTFET study: conductance decreased upon addition of  $\text{Ca}^{2+}$  ions from 1  $\mu\text{M}$  to 0.1 mM. The response of conductance change upon treatment with  $\text{Ca}^{2+}$  was biphasic. The faster drop was attributed to  $\text{Ca}^{2+}$  binding dynamics on the millisecond time scale,<sup>89</sup> the subsequent slower drop could be explained by hydrophobic interactions initiated by  $\text{Ca}^{2+}$  binding to CaM, and this time scale may span from seconds to many minutes.<sup>90</sup> Then the signal could be recovered as  $\text{Ca}^{2+}$  ions were bleached by a  $\text{Ca}^{2+}$ -free buffer (HEPES) flowing through the device. Addition of  $\text{Ca}^{2+}$  for second cycle produced the same relative response as the first cycle.

In a control experiment, the device was fabricated from pristine SWNTs, and incubated with CaM for the same period as in the o-SWNTs case. When the varying concentration of  $\text{Ca}^{2+}$  in buffer solutions were flowing across the device, no measurable electrical response was observed (Figure 4-7). This observation indicated that apo-CaM offered higher affinity on oxidized SWNTs, likely attributed to electrostatic interactions. In addition, because of less hydrophobic surface exposed in apo-CaM, even nonspecific adsorption, apo-CaM seemed not strongly bind to exterior surface of pristine SWNT.

In another control experiment, when a device fabricated with bare o-SWNT was treated with  $\text{Ca}^{2+}$  ions (Figure 4-8), the conductance showed no change until concentration of  $\text{Ca}^{2+}$  ions reached 0.1 mM. Binding of  $\text{Ca}^{2+}$  to carboxylate groups on the surface of oxidized SWNTs contributed to the drop in conductance. This experiment carried out with unmodified SWNT

indicate that the responses obtained at low concentration of  $\text{Ca}^{2+}$  ions are indeed arise from  $\text{Ca}^{2+}$  binding to CaM receptor. Additionally, compared to  $\text{Ca}^{2+}$  detection with pristine SWNT device, it seemed that  $\text{Ca}^{2+}$  ions in flowing solutions was insufficient to modulate the device Schottky barrier (SB) by changing the metal work function.

### **AFM Study**

Finally, AFM imaging was performed to observe the surface morphology of the CaM-SWNTs composite before and after addition of  $\text{Ca}^{2+}$ . The CaM-SWNT sample was prepared by mixing a suspension of o-SWNT ( $\sim 0.01$  mg/mL in HEPES) and CaM ( $\sim 1$   $\mu\text{M}$  in HEPES) and incubated for 1h at room temperature. The carboxylic functional groups impart hydrophilicity to the nanotubes and afford stable aqueous suspensions without apparent aggregation for 1 day.

The size changes between apo-CaM /SWNT and CaM-SWNT with addition of  $\text{Ca}^{2+}$  were difficult to investigate by AFM technique (Figure 4-9). Actually, AFM images did not reveal any significant difference in total height. However, there were some changes in the surface morphology for CaM adsorbed on SWNTs before and after addition of  $\text{Ca}^{2+}$ . AFMs image for apo-CaM on SWNTs revealed bright spots, indicating CaM molecules attached on SWNTs. After treatment with  $\text{Ca}^{2+}$  ions, the surface of SWNTs was almost fully covered, attributed to enhancement of hydrophobic interactions between CaM and SWNTs. The surface morphology in AFM is in good agreement with the results obtained from electronic measurements.

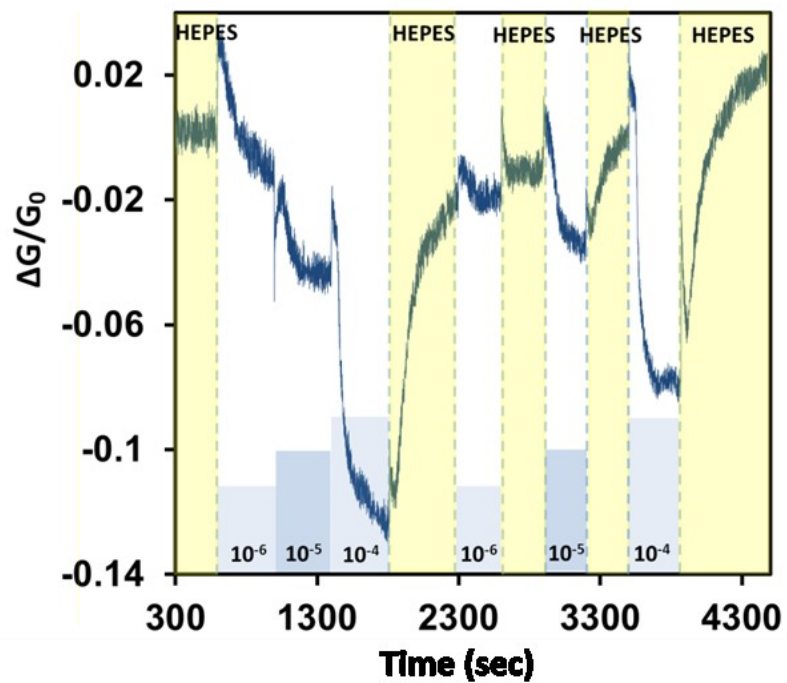


**Figure 4-6.** Real-time detection of the binding of  $\text{Ca}^{2+}$  to a CaM/o-SWNT device

The device was tested in a flowing buffer solution (HEPES 10mM pH=7.4) with varying concentration of  $\text{Ca}^{2+}$  ( $10^{-6}$  -  $10^{-4}$ M).

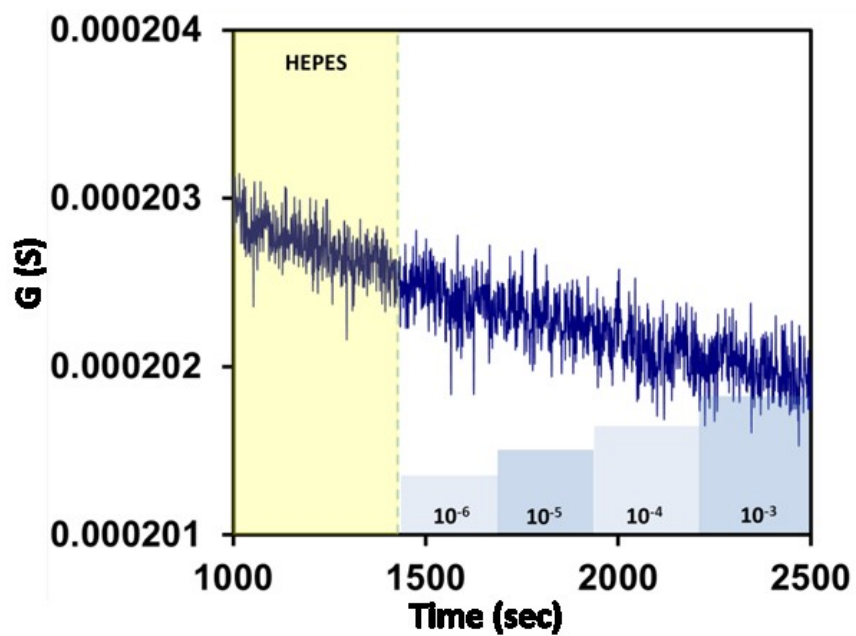


**Figure 4-7.** Control experiment on a pristine SWNT device

Real-time detection of the binding of Ca<sup>2+</sup> to a pristine SWNT device that was pre-incubated with CaM in a flowing buffer solution (HEPES 10mM pH=7.4) with varying concentration of Ca<sup>2+</sup> (10<sup>-6</sup> - 10<sup>-3</sup> M).

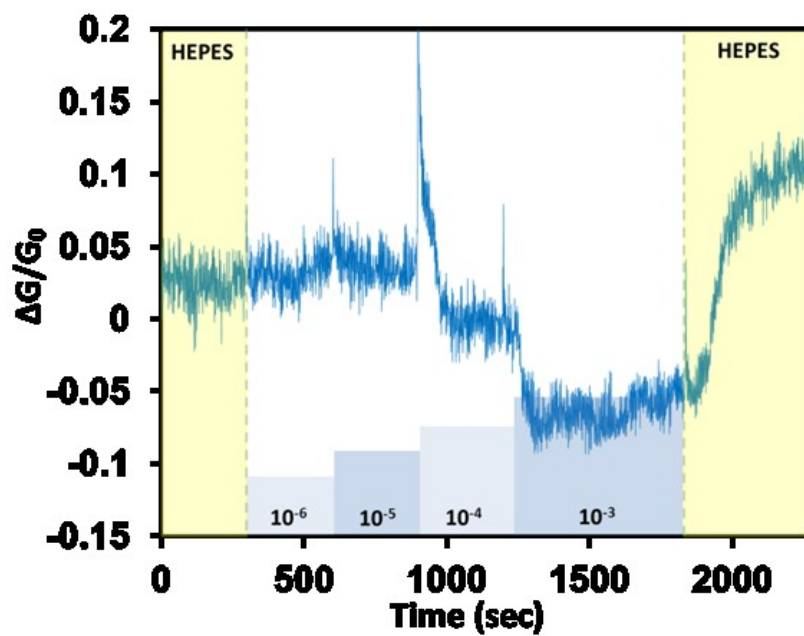


**Figure 4-8.** Control experiment on a bare o-SWNT device

Real-time detection of the  $\text{Ca}^{2+}$  on a bare o-SWNT device in a flowing buffer solution (HEPES 10mM pH=7.4) with varying concentration of  $\text{Ca}^{2+}$  ( $10^{-6}$  -  $10^{-3}$  M).

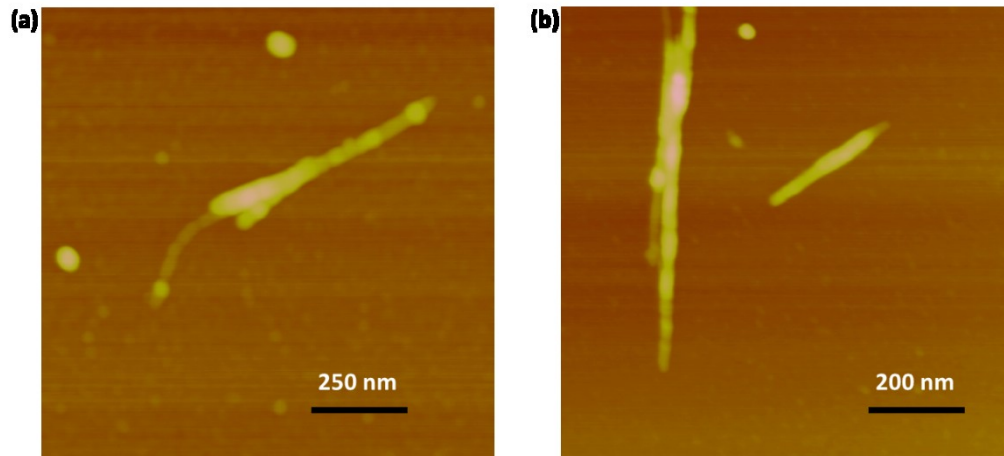


**Figure 4-9.** AFM images of apo-CaM/SWNTs and Ca<sup>2+</sup>-CaM/SWNTs

(a) apo-CaM on SWNTs, (b) CaM-SWNTs after addition of 1  $\mu\text{M}$  of Ca<sup>2+</sup>.

#### 4.2.4 Conclusion

In summary, we have demonstrated application of NTFET devices for highly selective detection of interactions between  $\text{Ca}^{2+}$  ions and CaM. The interaction between  $\text{Ca}^{2+}$  and CaM was transduced into changes in the device conductance ( $\Delta G$ ). Moreover, the  $\Delta G$  of CaM/NTFETs increased linearly with the log of  $[\text{Ca}^{2+}]$  over the range of  $10^{-7} - 10^{-4}$  M. In order to further investigate  $\text{Ca}^{2+}$ -induced conformational change for CaM, some targeted proteins such as CaM kinase I/II/IV, CaM kinase kinase, and myosin light chain kinase will be used to bind  $\text{Ca}^{2+}$ -CaM in the future study.

## 4.3 BACTERIOFERRITIN MODIFIED SWNTS FOR DETECTION OF IRON IONS

### 4.3.1 Introduction

The element iron is essential for life and plays a number of key roles in molecules and mechanisms where the oxidation states of iron is biologically relevant, i. e. insolubility of  $\text{Fe}^{3+}$  ions and potential of soluble  $\text{Fe}^{2+}$  to catalyze the formation of cell-damaging free radicals in the presence of  $\text{O}_2$ .<sup>91</sup> To overcome these problems, iron storage proteins, termed ferritin and ferritin-like proteins, have been developed by Nature. The ferritin family of proteins possesses a form of spherical protein coat surrounding a hollow center, where a large amount of iron can be stored and mineralized.<sup>92</sup>

Bacterioferritins (Bfrs) are composed of 24 subunits that assemble into a spherical protein with a hollow internal cavity. Bfrs are unique among ferritins in that they contain up to 12 heme molecules.<sup>93</sup> Basically, the iron storage process starts when  $\text{Fe}^{2+}$  is captured by the protein to form a diferrous center, known as the ferroxidase center, where it is oxidized to  $\text{Fe}^{3+}$ .<sup>94</sup> Structural studies with bacterioferritin from *Escherichia coli* (Ec Bfr) revealed that the ferroxidase center in Ec Bfr is stable in diferric form and does not return spontaneously to the apo form. In addition, the ferroxidase center does not act as a pore for entry of iron into the internal cavity.<sup>92,95</sup> In the structure of Bfr from *Azotobacter vinelandii* (Av Bfr) the ferroxidase center is occupied by two irons but the  $\text{Fe}_2$  position (nomenclature as in Figure 4-10B) has low occupancy, suggesting the translocation of  $\text{Fe}^{3+}$  from the ferroxidase center to the interior cavity.<sup>96</sup> Distinct from those two types of Bfrs, *Pseudomonas aeruginosa* bacterioferritin B (Pa BfrB) that can mineralize ~600 iron atoms in its core harbors a completely empty ferroxidase center.<sup>94</sup> Structural studies indicate

that the ferroxidase center in Pa BfrB functions in a dual role, as a cofactor and as a pore for the oxidation and internalization of iron (Figure 4-10).

In this work, we used PaBfrB modified NTFET devices to detect capturing of  $\text{Fe}^{2+}$  ions and investigated dual functions of ferroxidase center.

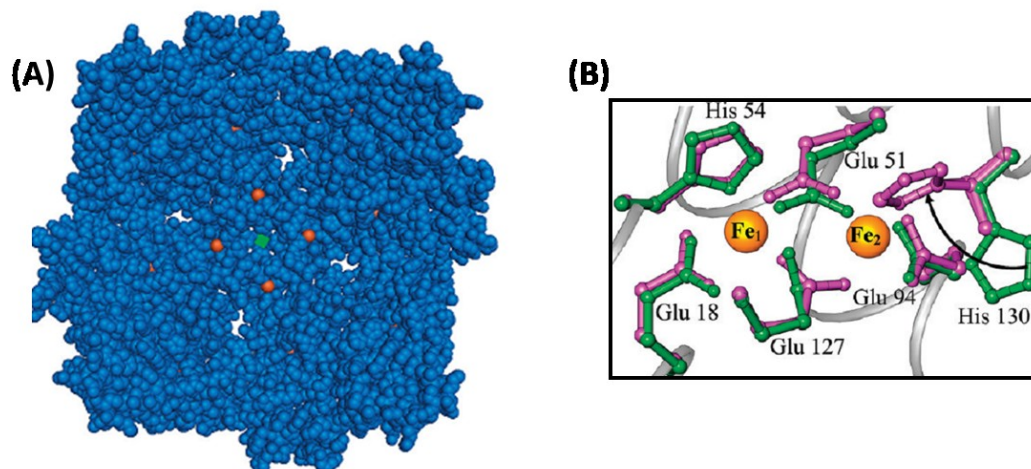


**Figure 4-10.** Structure of *Pseudomonas aeruginosa* bacterioferritin B (Pa BfrB) and its ferroxidase center upon complexation of  $\text{Fe}^{2+}$  ions.

(A) Fe-soaked Pa BfrB structure viewed from the interior cavity. The iron ions are represented by orange spheres. (B) Overlap of the Fe-soaked (magenta) and mineralized (green) Pa BfrB structures in ferroxidase center: All residues possess similar conformations with the exception of His130, which is rotated toward the ferroxidase center in the Fe-soaked structure, as indicated by the arrow, to assist Fe<sub>2</sub> binding. Adapted from Reference 94.

### 4.3.2 Experimental

NTFETs were fabricated with three types of SWNTs: pristine SWNTs, carboxylated SWNTs (P3-SWNTs) and oxidized SWNTs (o-SWNTs). All NTFET devices were noncovalently functionalized with Pa BfrB. Briefly, surface functionalization of SWNTs with Pa BfrB was performed by incubating the Si chips with 500  $\mu\text{g/mL}$  Pa BfrB in the buffer 2-(N-morpholino)ethanesulfonic acid (MES) (100 mM)/KCl (100mM) (pH = 6.5) for different period of time, 1h at room temperature, 6h and up to overnight at 4  $^{\circ}\text{C}$ , followed by rinsing with  $1\times$  PBS buffer.

$\text{Fe}^{2+}$  solutions were prepared in a range of concentrations of  $10^{-12}$ - $10^{-4}$  M from MES (100 mM)/KCl (100 mM) (pH =6.5), sealed in capped vials and filled with nitrogen gas to slow down oxidation of  $\text{Fe}^{2+}$  ions in the air.  $10^{-4}$  M  $\text{Ca}^{2+}$  solution in the same buffer solution was used as a control.  $\text{Zn}^{2+}$  solutions in range of  $10^{-12}$ - $10^{-4}$  M from MES (100mM)/KCl (100mM) (pH =6.5) were made for competition experiments. The functionalized NTFET chips were incubated for 10 min in different concentrations of metal ion solutions and later washed three times with  $1\times$  PBS buffer.

Pure iron-free *Pa* BfrB was obtained from Rivera Group.<sup>94</sup>

### 4.3.3 Results and Discussion

#### Selectivity Study

The liquid gate FET measurements of bare NTFETs exhibited p-type device characteristics (Figure 4-11). After functionalization with Pa BfrB, a decrease in conductance with a slight negative shift in gate voltage was observed, indicating the interaction between Pa BfrB and

SWNTs (Figure 4-11). A drop in conductance can be attributed to the net negative charge of the Pa BfrB (pI  $\sim$  5.85) at the measured pH of 6.5 and charge transfer to SWNTs. In a control experiment, the Pa BfrB functionalized device was treated with  $\text{Ca}^{2+}$  ions in a relatively high concentration ( $10^{-4}$  M), resulting in a slight decrease of conductance that may be due to binding of  $\text{Ca}^{2+}$  on carboxylated groups of SWNTs. However, this reduction in conductance caused by  $\text{Ca}^{2+}$  was negligible compared to the response to the treatment with  $\text{Fe}^{2+}$  ions in range of  $10^{-10}$ - $10^{-4}$  M, demonstrating excellent selectivity.

The selectivity study also demonstrated the different mechanisms for reduction of the device on conductance induced by  $\text{Fe}^{2+}$  and  $\text{Ca}^{2+}$  ions. Briefly,  $\text{Fe}^{2+}$  ions were captured by Pa BfrB and oxidized to  $\text{Fe}^{3+}$  ions which were subsequently mineralized in the inner cavity of protein,<sup>94</sup> thus the response of the device upon treatment with  $\text{Fe}^{2+}$  could be caused by a combination of the effects: the increased positive charges by  $\text{Fe}^{2+}$  capturing, electron transport by  $\text{Fe}^{2+}$  oxidation, and induced negative charges by  $\text{Fe}^{3+}$  mineralization. Positively charged  $\text{Fe}^{2+}$  bound on a functionalized device is one possible reason for a decrease in the p-type conductance. The electron transfer from  $\text{Fe}^{2+}$  oxidation to valence band of SWNTs can cause the negative shift in I- $V_g$  curves. Moreover,  $\text{Fe}^{3+}$  mineralization where anions are needed to support the growth of a mineral core<sup>94</sup> could induce additional negative charge in the SWNT, thus n-doping the SWNT and shifting the I- $V_g$  curve toward more negative gate voltages. On the other hand,  $\text{Ca}^{2+}$  seemed to interact with the SWNT surface rather than with the protein attached to the SWNT. To prove this, in a control experiment, metal ions were applied to bare P3-SWNTFET devices. Upon treatment with  $\text{Ca}^{2+}$  or  $\text{Fe}^{2+}$  at high concentration ( $10^{-4}$  M) (Figure 4-12), device conductance was decreased comparably in both cases. The reduction of conductance was mainly caused by positively charged ions binding to p-type SWNTs, thus decreasing the concentration of hole-

carriers. The similar responses ( $\Delta G/G_0 \sim 0.06$ ) for  $\text{Ca}^{2+}$  and  $\text{Fe}^{2+}$  on bare SWNT devices could provide evidence for the good selectivity of Pa BfrB functionalized NTFET devices.

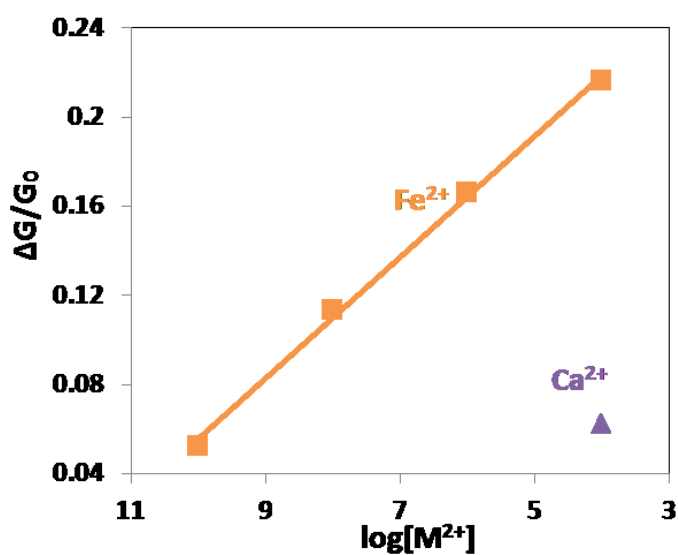
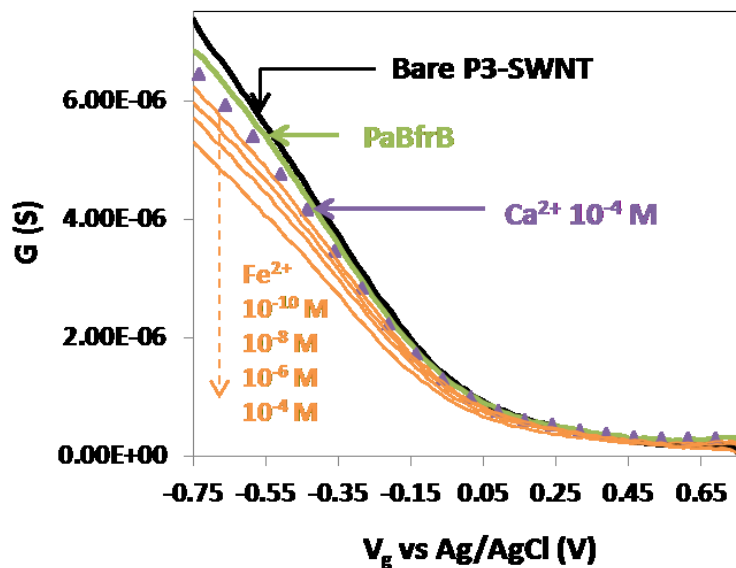


**Figure 4-11.** Electronic detection of  $Fe^{2+}$  ions on Pa BfrB/ P3-SWNTFET device

(Top) conductance ( $G$ ) vs gate voltage ( $V_g$ ) of bare P3-SWNTFET device (black line) after functionalization with Pa BfrB (incubation for 1 h) (green line), and sensitivity for varying concentration of the  $Fe^{2+}$  ( $10^{-10}$  to  $10^{-4}$  M) (orange lines) with  $Ca^{2+} 10^{-4}$  M as a control (purple triangle dots). (Bottom) Biosensor calibration plot: normalized change in the device conductance *versus* metal ion concentrations.

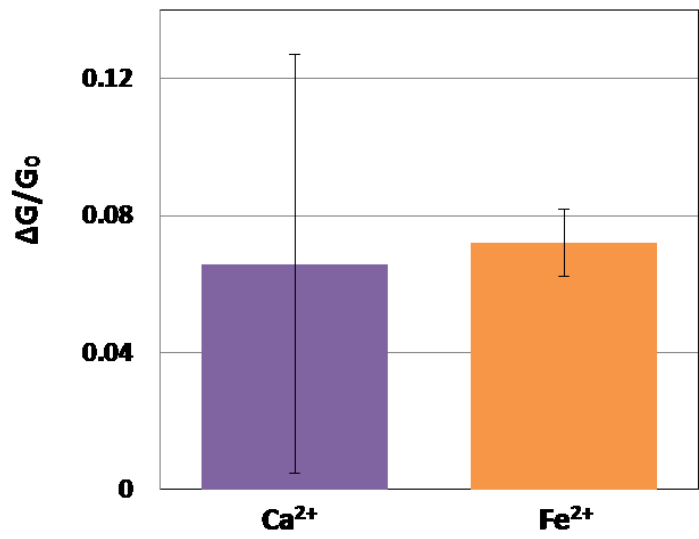
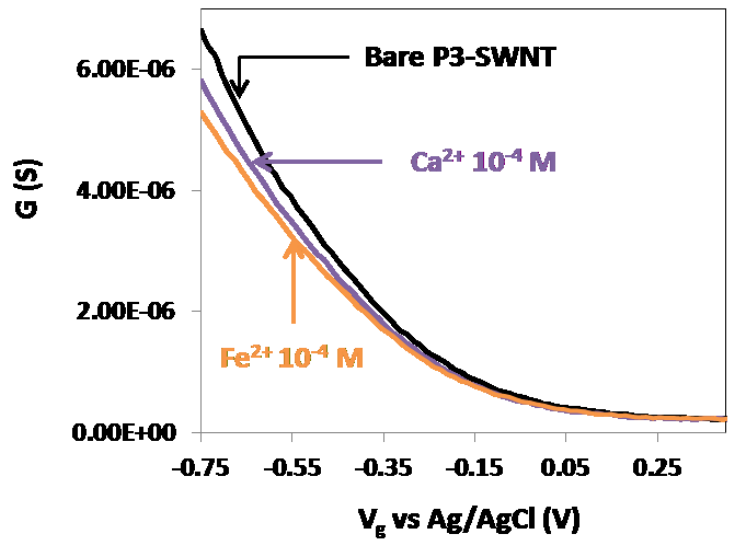


**Figure 4-12.** Electronic detection of metal ions interactions with bare P3-SWNTFETs

Both  $Ca^{2+}$  (purple) and  $Fe^{2+}$  ions (orange) are in  $10^{-4} M$ .

## Competition Study

Some Bfrs possess a stable ferroxidase center that functions exclusively as a cofactor for the oxidation of  $\text{Fe}^{2+}$ , such as Ec Bfr; whereas Pa BfrB forms an “unstable” ferroxidase center that functions in the oxidation of  $\text{Fe}^{2+}$  and as a pore for the translocation of  $\text{Fe}^{3+}$  into the internal cavity.<sup>94</sup> The instability of the diferric center may be a feature that allows Pa BfrB to efficiently take up iron *via* the ferroxidase center. Here we used  $\text{Zn}^{2+}$  ion, a potent competitive inhibitor of  $\text{Fe}^{2+}$  binding and oxidation,<sup>95</sup> to apply in the NTFET study for illustration of the dual role for the ferroxidase center of Pa BfrB.

As demonstrated in Figure 4-13, binding of  $\text{Fe}^{2+}$  ions to Pa BfrB functionalized o-SWNTFET under aerobic conditions leads to a negative shift of I- $V_g$  curve, due to mixed contributions from  $\text{Fe}^{2+}$  binding, oxidation, and mineralization. Then the addition of  $\text{Zn}^{2+}$  ions to the same device led to a continuous decrease in p-type conductance, indicating binding of  $\text{Zn}^{2+}$  ions at ferroxidase center. However, the NTFET device showed a smaller slope of  $\Delta G/G_0$  vs  $\text{Zn}^{2+}$  concentration than  $\Delta G/G_0$  vs  $\text{Fe}^{2+}$  concentration, indicating that  $\text{Zn}^{2+}$  ions may simply bind at the empty ferroxidase centers rather than displace all of the iron from Bfr, which occurs for Ec Bfr.<sup>95</sup>

On the other hand, the addition of  $\text{Zn}^{2+}$  ions prior to addition  $\text{Fe}^{2+}$  resulted in reduction in device conductance to the same level as addition of  $\text{Zn}^{2+}$  after the iron (Figure 4-14), indicating  $\text{Zn}^{2+}$  binding at the ferroxidase centers. Then the addition of  $\text{Fe}^{2+}$  ions to the same device resulted in only a minor decrease in conductance, consistent with the ability of  $\text{Zn}^{2+}$  to effectively block  $\text{Fe}^{2+}$  binding at the ferroxidase center.

In different experiments using P3-SWNTFET, we observed that the pre-addition of  $\text{Zn}^{2+}$  (Figure 4-17) could show higher response of devices than post-addition of  $\text{Zn}^{2+}$  (Figure 4-16). These results could be attributed to detection sensitivity of different devices, instead could imply

that ferroxidase centers may not be the only binding sites for  $Zn^{2+}$  and  $Fe^{2+}$ . Thus  $Zn^{2+}$  ions pre-added could bind to other sites besides ferroxidase centers. And  $Zn^{2+}$  post-added can only bind at ferroxidase centers, because iron has already occupied all the internal sites in Pa BfrB. Although these observations need further experimental evidence to support this hypothesis, they were in agreement that ferroxidase center acts as a gated iron pore as well as catalytic sites for  $Fe^{2+}$ .

In addition, we observed some differences in the responses of Pa BfrB functionalized NTFET devices when incubation periods were varied from 1h to overnight (~ 20 hr). Incubation for 1hr resulted in the smallest response (Figure 4-15) compared to incubation of longer period in fridge, due to less amount of proteins adsorbed on SWNTs.

Moreover, it seemed that devices fabricated with SWNTs containing more carboxylated groups resulted in enhanced response to  $Fe^{2+}$  ions, primarily due to increased adsorption of Pa BfrB on SWNTs. Comparison of pristine SWNTs devices (Figure 4-18), P3-SWNT devices (Figure 4-16 & 4-17) and o-SWNT devices (Figure 4-13 & 4-14) showed that the hydrophobic interactions were not the only reason for adsorption of Pa BfrB, amino affinity may also increase with more carboxylated groups,<sup>78</sup> thus leading to detection of more iron storage.

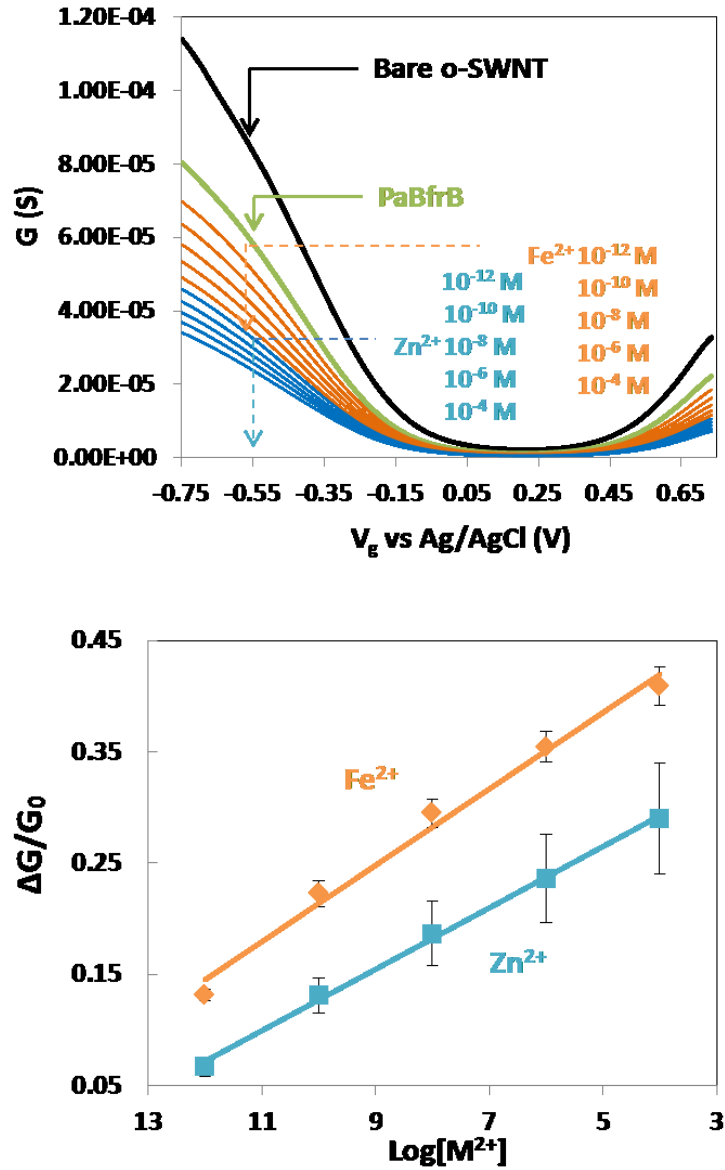


**Figure 4-13.** Electronic detection of competition between  $Fe^{2+}$  (first added) and  $Zn^{2+}$  (next added) on Pa BfrB/o-SWNTFET devices

Electronic study of competition between  $Fe^{2+}$  (orange) and  $Zn^{2+}$  (blue) on Pa BfrB modified o-SWNTFET devices (incubation for overnight at  $4^\circ C$ ), with first treatment with  $Fe^{2+}$  then  $Zn^{2+}$  next. (Top) NTFET characteristics and (bottom) biosensor calibration plot: normalized change in the device conductance *versus* metal ion concentrations.

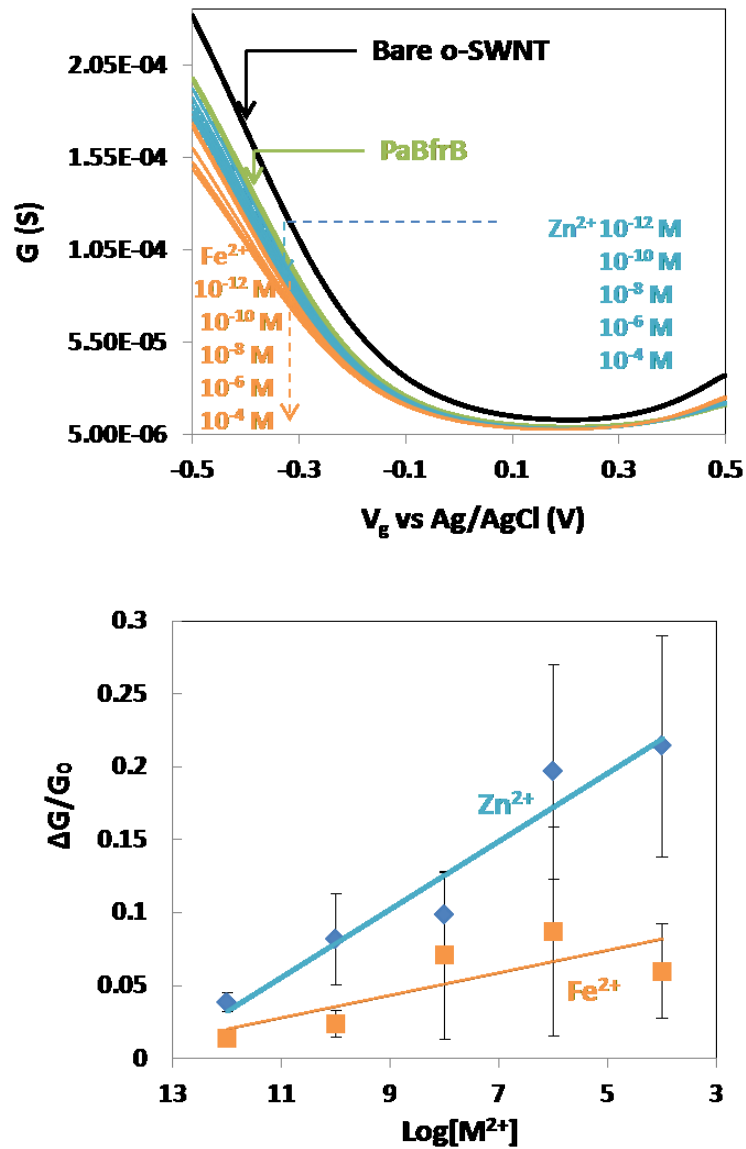


**Figure 4-14.** Electronic detection of competition between  $Zn^{2+}$  (first added) and  $Fe^{2+}$  (next added) on Pa BfrB/o-SWNTFET devices

Electronic study of competition between  $Fe^{2+}$  (orange) and  $Zn^{2+}$  (blue) on Pa BfrB modified o-SWNTFET devices (incubation for overnight at 4 °C), with first treatment with  $Zn^{2+}$  then  $Fe^{2+}$  next. (Top) NTFET characteristics and (bottom) biosensor calibration plot: normalized change in the device conductance versus metal ion concentrations.

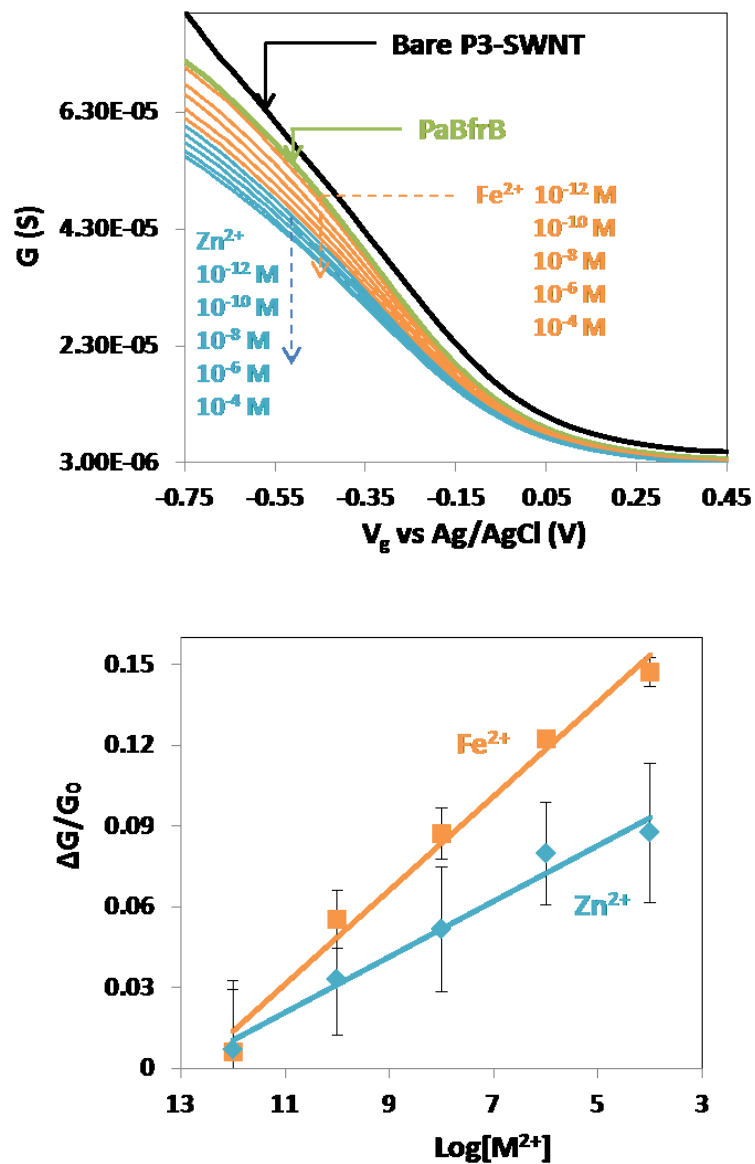


**Figure 4-15.** Electronic detection of on Pa BfrB/P3-SWNTFET devices in 1h incubation

Electronic study of competition between  $Fe^{2+}$  (orange) and  $Zn^{2+}$  (blue) on Pa BfrB modified P3-SWNTFET devices (incubation for 1 h at room temperature), with first treatment with  $Fe^{2+}$  then  $Zn^{2+}$  next. (Top) NTFET characteristics and (bottom) biosensor calibration plot: normalized change in the device conductance versus metal ion concentrations.

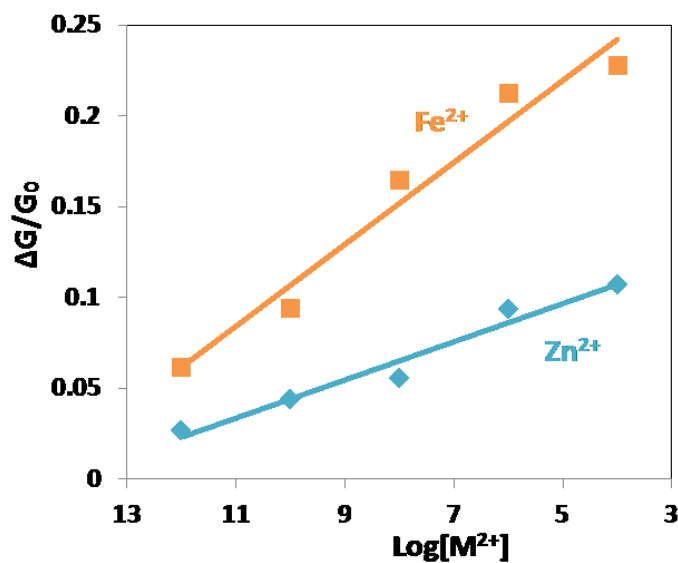
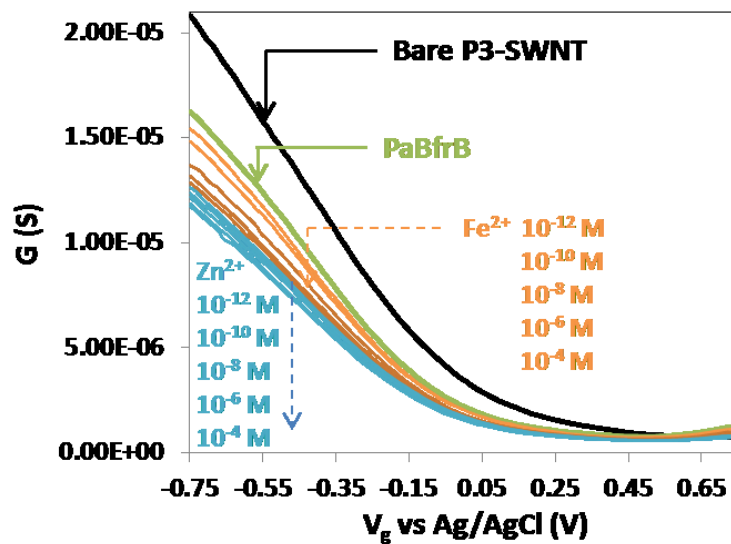


**Figure 4-16.** Electronic detection of on Pa BfrB/P3-SWNTFET devices in 6h incubation with first treatment with  $\text{Fe}^{2+}$  then  $\text{Zn}^{2+}$  next.

Electronic study of competition between  $\text{Fe}^{2+}$  (orange) and  $\text{Zn}^{2+}$  (blue) on Pa BfrB modified P3-SWNTFET devices (incubation for 6 h at 4 °C), with first treatment with  $\text{Fe}^{2+}$  then  $\text{Zn}^{2+}$  next. (Top) NTFET characteristics and (bottom) biosensor calibration plot: normalized change in the device conductance versus metal ion concentrations.

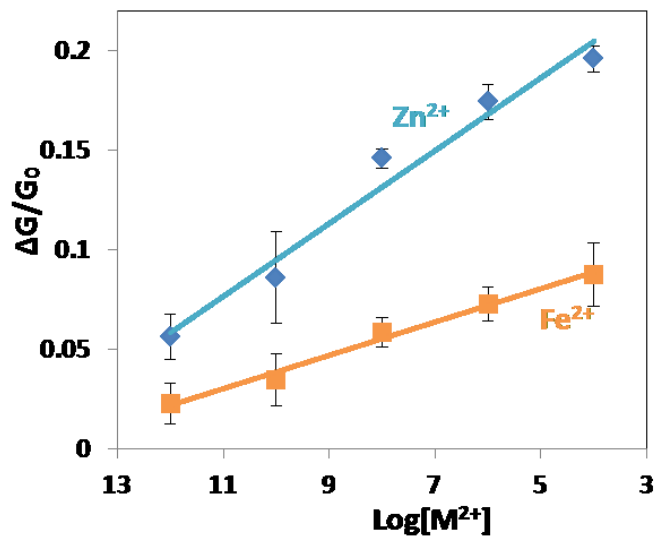
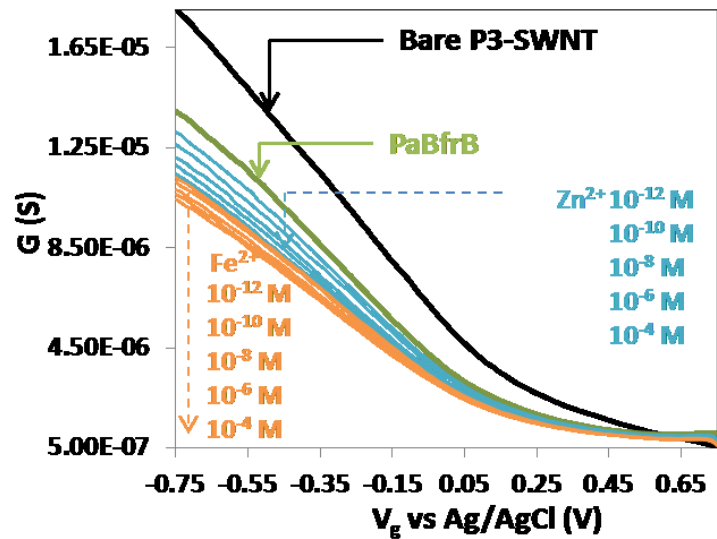


**Figure 4-17.** Electronic detection of on Pa BfrB/P3-SWNTFET devices in 6h incubation with first treatment with  $Zn^{2+}$  then  $Fe^{2+}$  next

Electronic study of competition between  $Fe^{2+}$  (orange) and  $Zn^{2+}$  (blue) on Pa BfrB modified P3-SWNTFET devices (incubation for 6 h at 4 °C), with first treatment with  $Zn^{2+}$  then  $Fe^{2+}$  next. (Top) NTFET characteristics and (bottom) biosensor calibration plot: normalized change in the device conductance versus metal ion concentrations.

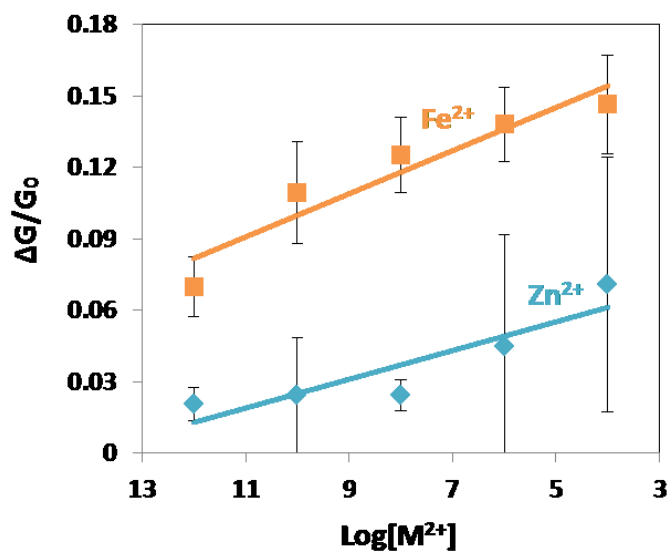
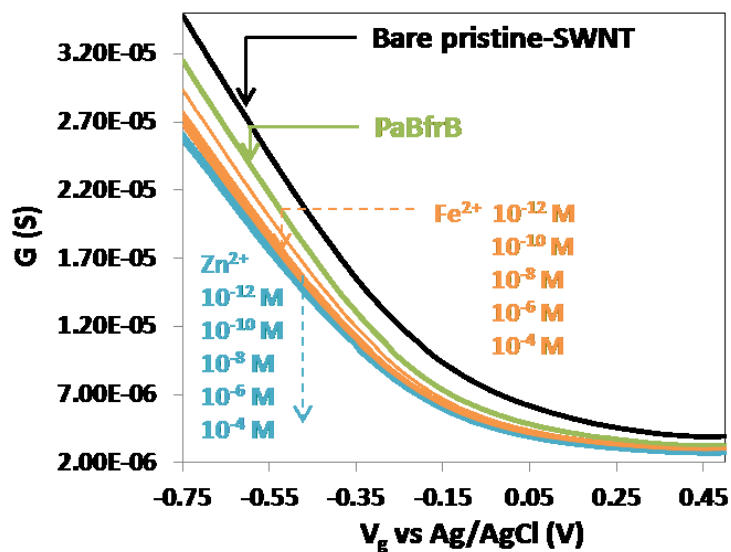


Figure 4-18. Control experimental on Pa BfrB/pristine-SWNT device

Electronic study of competition between  $\text{Fe}^{2+}$  (orange) and  $\text{Zn}^{2+}$  (blue) on Pa BfrB modified pristine-SWNTFET devices (incubation for 6 h at 4 °C), with first treatment with  $\text{Fe}^{2+}$  then  $\text{Zn}^{2+}$  next. (Top) NTFET characteristics and (bottom) biosensor calibration plot: normalized change in the device conductance versus metal ion concentrations.

## Conductance Measurements

The real-time detection of  $\text{Fe}^{2+}$  ions (in competition with  $\text{Zn}^{2+}$ ) was performed by plotting of conductance *versus* time for a Pa BfrB functionalized o-SWNTFET device. Addition of  $\text{Fe}^{2+}$  resulted in a rapid reduction in conductance followed by a slower increase (Figure 4-19). This behavior is consistent with biphasic response described in the literature:<sup>94</sup> The rapid phase corresponds to the oxidation of di- $\text{Fe}^{2+}$  center to form a di- $\text{Fe}^{3+}$  center at ferroxidase center, that n-doped SWNT and thus decreased conductance; while the subsequent slower phase corresponds to the mineralization of iron with the cavity, and the decrease of positive charge led to recovery of conductance. On the other hand, the addition of  $\text{Zn}^{2+}$  resulted in relatively negligible change in conductance, maybe attributed to its only occupancy in ferroxidase centers.

It is worth to mention that the conductance measurements were performed at  $V_g = 0$ , at which the conductance changes were minor according to NTFET studies (Figure 4-13). So the conductance measurement cannot exactly explain the kinetic behavior of iron mineralization in Pa BfrB, and addition of  $\text{Fe}^{2+}$  at  $10^{-10}$  and  $10^{-8}$  M did not show any biphasic response. However, it clearly displayed the different behavior upon treatment with  $\text{Fe}^{2+}$  and  $\text{Zn}^{2+}$ , and supported the hypothesis that the ferroxidase center was a catalytic site for  $\text{Fe}^{2+}$  ions and was free of iron after its catalytic process completed (Figure 4-10), which explain why  $\text{Zn}^{2+}$  cannot displace  $\text{Fe}^{3+}$  ions in Pa BfrB.

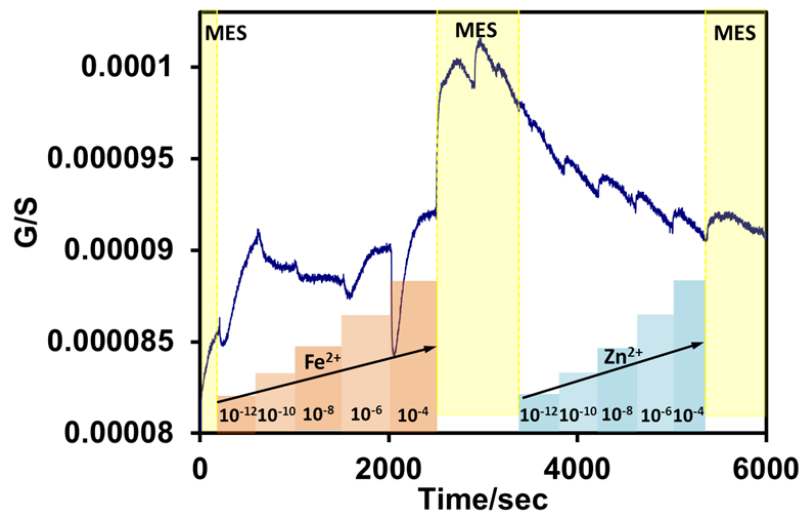


**Figure 4-19.** Conductance measurement on Pa BfrB/o-SWNT device

Real-time detection of the binding of  $\text{Fe}^{2+}$  to a Pa BfrB modified o-SWNT device in MES (100 mM)/KCl (100 mM) buffer solutions with varying concentrations of  $\text{Fe}^{2+}$  and  $\text{Zn}^{2+}$  ions ( $10^{-12}$  -  $10^{-4}$ M).

## AFM Study

Finally, AFM imaging was performed to observe the surface morphology of the modified SWNTs. The Pa BfrB modified SWNT samples were prepared by a mixing suspension of o-SWNT (~ 0.01 mg/mL in MES) and Pa BfrB (~ 1  $\mu$ M in MES) and incubation for 1h at room temperature. The carboxylated functional groups impart hydrophilicity to the nanotubes and make them stable in aqueous solutions without apparent aggregation for 1 day.

An average height of around 1 nm was observed for bare SWNTs indicating individual SWNTs (Figure 4-20). After functionalization with Pa BfrB the total height increased to 12 nm, where Pa BfrB was previously reported with an external diameter of ~11 nm.<sup>94</sup> Later, when Pa BfrB functionalized SWNTs were exposed to  $\text{Fe}^{2+}$  ions, no obvious change in height was observed, supporting iron stored inside the Pa BfrB (Figure 4-21). As a control, exposure of bare P3-SWNTs to  $\text{Fe}^{2+}$  ions resulted in obvious bundles of carbon nanotubes (Figure 4-20), suggesting  $\text{Fe}^{2+}$  intertube binding on carboxylated groups P3-SWNTs.

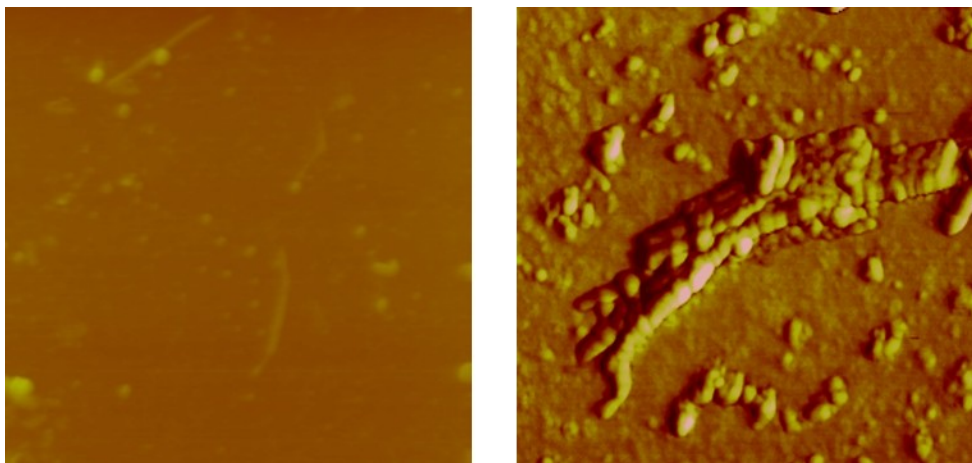


**Figure 4-20.** AFM images of bare P3-SWNTs before and after Fe<sup>2+</sup> addition

AFM images of (left) bare P3-SWNTs (a), and (right) bundles of P3-SWNTs due to Fe<sup>2+</sup> intertubes coordination.

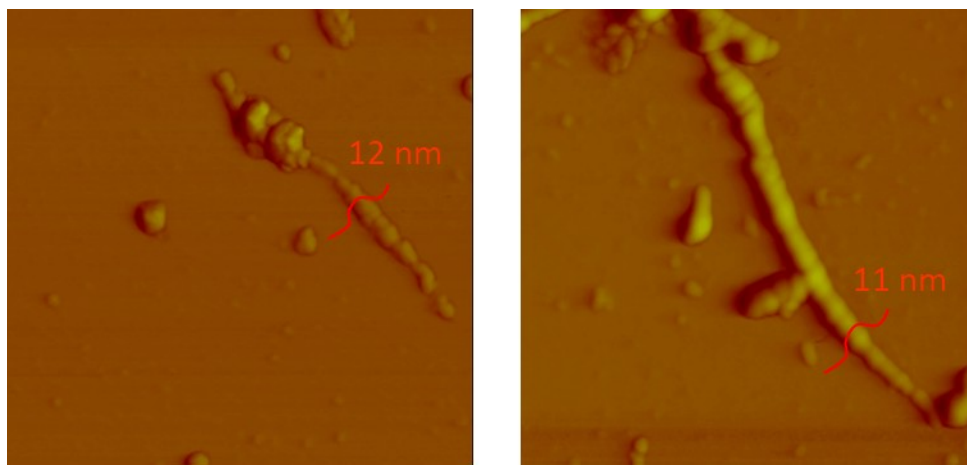


**Figure 4-21.** AFM images of Pa BfrB/P3-SWNTs before and after Fe<sup>2+</sup> addition

AFM images of Pa BfrB/P3-SWNTs composite before (left) and after Fe<sup>2+</sup> addition (right).

#### 4.3.4 Conclusion

In summary, we have demonstrated application of Pa BfrB NTFET devices for highly selective detection of iron storage. The  $\Delta G$  of Pa BfrB modified NTFETs increased linearly with the log of  $[\text{Fe}^{2+}]$  over a range of  $10^{-12} - 10^{-4}$  M, showing great sensitivity. Also the electronic detection of competitive  $\text{Zn}^{2+}$  ions supported the hypothesis that ferroxidase center of Pa BfrB plays a dual role as catalytic sites and pore of entry, which is distinct from Ec BfrB.

## BIBLIOGRAPHY

---

- (1) Hobman, J. L. *Mol. Microbio.* **2007**, 63, 1275.
- (2) A. Hulanicki, S. Glab, and F. Ingman, *Pure & Appl. Chem.*, **1991**, 63, 1247.
- (3) C. Strydom, C. Robinson, E. Pretorius, J.M. Whitcutt, J. Marx, M.S. Bornman, ISSN 0378-4738 = Water SA Vol. 32 No. 4 October 2006
- (4) R. B. Martin, in *Encyclopedia of Inorganic Chemistry*, Vol. 4, Wiley, Chichester **1994**
- (5) J.S. Benco, H.A. Nienaber, W.G. McGimpsey, *Sens. Actuators, B, Chem.* **2002**, 85, 126
- (6) Marsella, M. J.; Newland, R. J.; Carroll, P. J.; Sweger, T. M. *J. Am. Chem. Soc.* **1995**, 117, 9842
- (7) (a) Zazula, W.; Chapoteau, E.; Czech, B. P.; Kumar, A. J. *J. Org. Chem.* **1992**, 57, 6720; (b) Bartsch, R. A.; Chapoteau, E.; Czech, B. P.; Krzykawski, J.; Kumar, A. J.; Robison, T. *W. J. Org. Chem.* **1994**, 59, 616
- (8) (a) Prodi, L.; Bargossi, C.; Montalti, M.; Zaccheroni, N.; Su, N.; Bradshaw, J. S.; Izatt, R. M.; Savage, P. B. *J. Am. Chem. Soc.* **2000**, 122, 6769. (b) Rurack, K.; Kollmannsberger, M.; Resch-Genger, U.; Daub, J. *J. Am. Chem. Soc.* **2000**, 122, 968
- (9) S. Iijima, *Nature*, **1991**, 354, 56
- (10) M. Monthieux, V. Kuznetsov, V *Carbon*, **2006**, 44, 1621.
- (11) (a) T. W. Odom, J. -L. Huang, P. Kim, C. M. Lieber *J. Phys. Chem. B* **2000**, 104, 2794.

- 
- (b) K. Balasubramanian, M. Burghard *Small* **2005**, 1, 180.
- (12) Wallace, P. R. *Phys. Rev.* **1947**, 71, 622
- (13) R. Satio, M. Fujita, G. Dresselhaus, M. S. Dresselhaus *Appl. Phys. Lett.* **1992**, 60, 2204
- (14) S. V. Rotkin in *Applied Physics of Carbon Nanotubes* (Eds.: S. V. Rotkin and S. Subramoney), Springer, New York, **2005**, pp. 3-39.
- (15) S. J. Tans, A. R. M. Verschueren, C. Dekker, *Nature*, **1998**, 393, 49.
- (16) M. Meitl, Y. Zhou, A. Gaur, S. Jeon, M. Usrey, M. Strano, J. Rogers *Nano Lett.* **2004**, 4, 1643
- (17) Z. Wu, Z. Chen, X. Du, J. Logan, J. Sippel, M. Nikolou, K. Kamaras, J. Reynolds, D. Tanner, A. Hebard, A. Rinzler *Science* **2004**, 305, 1273
- (18) I. Sayago, E. Terrado, M. Aleixandre, M.C. Horrillo, M.J. Fernandez, J. Lozano, E. , W.K. Maser, A.M. Benito, M.T. Martinez, J. Gutierrez, E. Munoz *Sensors and Actuators B* **2007**, 122, 75
- (19) E. Bekyarova, I. Kalinina, M. E. Itkis, L. Beer, N. Cabrera, R. C. Haddon *J. Am. Chem. Soc* **2007**, 129, 10700
- (20) E. Snow, J. Novak, P. Campbell, D. Park *Appl. Phys. Lett.* **2003**, 82, 2145
- (21) L. Hu, D. S. Hecht, G. Grüner *Nano Lett.* **2004**, 4, 2513
- (22) Website of [http://en.wikipedia.org/wiki/Percolation\\_threshold](http://en.wikipedia.org/wiki/Percolation_threshold)
- (23) M. Stadermann, S. J. Papadakis, M. R. Falvo, J. Novak, E. Snow, etc. *Phys. Rev. B* **2004**, 69, 201402
- (24) T. Sreekumar, T. Liu, S. Kumar, L. Ericson, R. Hayge, R. Smalley *Chem. Mater.* **2003**, 15, 175.

- 
- (25) M. Spotnitz, D. Ryan, H. J. Stone *Mater. Chem.* **2004**, 14, 1299
- (26) A. Schindler, J. Brill, N. Fruehauf, J. P. Novak, Z. Yaniv *Phys. E* **2007**, 37, 119
- (27) Z. Li, P. Dharap, S. Nagarajaiah, E. Barrera, J. Kim *Adv. Mater.* **2004**, 16, 640
- (28) S. Lim, H. Jeong, Y. Park, D. Bae, Y. Choi, Y. Shin, W. Kim, K. An, Y. J. Lee *Vac. Sci. Technol. A* **2001**, 19, 1786
- (29) Y. Zhou, A. Gaur, S.-H. Hur, C. Kocabas, M. A. Meitl, M. Shim, J. A. Rogers *Nano Lett.* **2004**, 4, 2031
- (30) K. Bradley, J.-C. P. Gabriel, G. Gruner *Nano Lett.* **2003**, 3, 1353
- (31) D. R. Kauffman, C. M. Shade, H. Uh, S. Petoud, and A. Star. *Nat Chem.* **2009**, 1, 500.
- (32) H. Vedala, Y. Chen, S. Cecioni, A. Imberty, S. Vidal, A. Star *Nano. Lett.* **2011**, 11, 170.
- (33) M. Ding, Y. Tang, P. Gou, M. J. Reber, A. Star. *Adv. Mater.* **2011**, 23, 536.
- (34) S. M. Bachilo, M. S. Strano, C. Kittrell, R. H. Hauge, R. E. Smalley, R. Bruce Weisman *Science*, **2002**, 298, 2361
- (35) K. Bradley, J.-C. P. Gabriel, A. Star, G. Gruner *Appl. Phys. Lett.* **2003**, 83, 3821
- (36) C. A. Hunter, J. K. M. Sanders *J. Am. Chem. Soc.* **1990**, 112, 5525
- (37) J. Zhao, J. P. Lu, J. Han, C.-K. Yang *Appl. Phys. Lett.* **2003**, 82, 3746
- (38) Y. Sun, S. R. Wilson, D. I. Schuster *J. Am. Chem. Soc.* **2001**, 123, 5348
- (39) A. Star, J. F. Stoddart, D. Steuerman, M. Diehl, A. Boukai, E. Wong, X. Yang, S.-W. Chung, H. Choi, J. R. Heath *Angew. Chem., Int. Ed.* **2001**, 40, 1721
- (40) D. R. Kauffman and A. Star *Small* **2007**, 3, 1324
- (41) D.R. Kauffman, O. Kuzmych, A. Star, *J. Phys. Chem. C* **2007**, 111, 3539.

- 
- (42) J. Kong, N. R. Franklin, C. Zhou, M. G. Chapline, S. Peng, K. Cho, H. Dai, *Science*, **2000**, 287, 622.
- (43) A. Star, E. Tu, J. Niemann, J.-C. P. Gabriel, C. S. Joiner, C. Valcke, *Proc. Natl. Acad. Sci. U. S. A.*, **2006**, 103, 921.
- (44) A. Star, J.-C. P. Gabriel, K. Bradley, G. Grüner, *Nano Letters* **2003**, 3, 459.
- (45) R. J. Chen, S. Bangsaruntip, K. A. Drouvalakis, N. Wong Shi Kam, M. Shim, Y. Li, W. Kim, P. J. Utz, H. Dai, *Proc. Natl. Acad. Sci. USA* **2003**, 100, 4984.
- (46) A. Star, T. R. Han, V. Joshi and J. Stetter, *Electroanalysis*, **2004**, 16, 108.
- (47) C. Journet, W. K. Maser, P. Bernier, A. Loiseau, M. L. de la Chapelle, S. Lefrant, P. Deniard, R. Lee, J. E. Fischer, *Nature* **1997**, 388, 756.
- (48) E. H. Vickery, L. F. Pahler, E. J. Eisenbraun, *J. Org. Chem.* **1979**, 44, 4444.
- (49) D.-H. Kim, M. J. Choi, S.-K. Chang, *Bull. Korean Chem. Soc.* **200**, 21, 145.
- (50) A. J. Gallant, M. J. MacLachlan, *Angew. Chem. Int. Ed.* **2003**, 42, 5307.
- (51) X. Zhang, M. Köhler, A. J. Matzger, *Macromolecules* **2004**, 37, 6306.
- (52) C. J. Yang, S. A. Jenekhe, *Chem. Mater.* **1991**, 3, 878.
- (53) A. C. W. Leung, M. J. MacLachlan, *J. Mater. Chem.* **2007**, 17, 1923.
- (54) C.-Y. Li, X.-B. Zhang, Z. Jin, R. Han, G.-L. Shen, R.-Q. Yu, R.-Q., *Anal. Chim. Acta* **2006**, 580, 143.
- (55) D. R. Kauffman, A. Star, *J. Phys. Chem. C* **2008**, 112, 4430.
- (56) (a) H. Kataura, Y. Kumazawa, Y. Maniwa, I. Umezumi, S. Suzuki, Y. Ohtsuka, Y. Achiba, *Synth. Met.* **1999**, 103, 2555; (b) J.-I. Aihara, *J. Phys. Chem. A.* **1999**, 103, 7487.
- (57) N. Kuhnert, G. M. Rossignolo and A. Lopez-Periago, *Org. Biomol. Chem.*, **2003**, 1, 1157.

- 
- (58) W. Zhao, C. Song, P. E. Pehrsson *J. Am. Chem. Soc.* **2002**, 124, 12418.
- (59) D. A. Skoog, F. J. Holler and S. R. Crouch, *Principles of Instrumental Analysis*, Thomson Brooks/Cole, Belmont, CA, **2007**.
- (60) P. Bergveld, *Sensors Actuators B: Chem.*, **2003**, 88, 1.
- (61) A. Talaie, *Polymer*, **1997**, 38, 1145.
- (62) H. Kaden, H. Jahn and M. Berthold, *Solid State Ionics*, **2004**, 169, 129.
- (63) W. Gao and J. Song, *Electroanalysis*, **2009**, 21, 973.
- (64) G. Jin, J. Novish, C. Too and G. Wallace, *CAP*, **2004**, 4, 366.
- (65) Y. Liao, C. Zhang, Y. Zhang, V. Strong, J. Tang, X.-G. Li, K. Kalantar-Zadeh, E. M. V. Hoek, K. L. Wang and R. B. Kaner, *Nano Letters*, **2011**, 11, 954
- (66) D. K. Moon, K. Osakada, T. Maruyama, K. Kubota and T. Yamamoto, *Macromolecules*, 1993, **26**, 6992.
- (67) R. C. Faria and L. O. S. Bulhões, *Electrochim. Acta*, **1999**, 44, 1597.
- (68) M. Gao, S. Huang, L. Dai, G. Wallace, R. Gao and Z. Wang, *Angew. Chem. Int. Ed.*, **2000**, 39, 3664.
- (69) (a) M. Zheng and B. A. Diner, *J. Am. Chem. Soc.*, **2004**, 126, 15490; (b) M. J. O'Connell, E. Eibergen and S. K. Doorn, *Nat Mater*, **2005**, 4, 412; (c) D. R. Kauffman, O. Kuzmych and A. Star, *J. of Phys. Chem. C*, **2007**, 111, 3539; (d) D. R. Kauffman, D. C. Sorescu, D. P. Schofield, B. L. Allen, K. D. Jordan and A. Star, *Nano Lett*, **2010**, 10, 958.
- (70) R. Saito and M. Fujita, *Appl. Phys. Lett.*, **1992**, 60, 2204
- (71) P. G. Collins, K. Bradley, M. Ishigami and A. Zettl, *Science*, **2000**, 287, 1801.
- (72) S. Virji, J. Huang, R. B. Kaner and B. H. Weiller, *Nano Letters*, **2004**, 4, 491.

- 
- (73) A. Star, E. Tu, J. Niemann, J.-C. P. Gabriel, C. S. Joiner, C. Valcke, *Proc. Natl. Acad. Sci. U. S. A.*, **2006**, 103, 921.
- (74) A. Star, T.-R. Han, J.-C. P. Gabriel, K. Bradley and G. Grüner, *Nano Lett.*, **2003**, 3, 1421
- (75) T. Someya, J. Small, P. Kim, C. Nuckolls and J. T. Yardley, *Nano Lett.*, **2003**, 3, 877.
- (76) S. J. Tans, A. R. M. Verschueren, C. Dekker, *Nature*, **1998**, 393, 49.
- (77) A. Star, J.-C. P. Gabriel, K. Bradley, G. Grüner, *Nano Lett.* **2003**, 3, 459
- (78) K. Bradley, M. Briman, A. Star, G. Grüner, *Nano Lett.* **2004**, 4, 253
- (79) D. S. Hecht, R. J. A. Ramirez, M. Briman, E. Artukovic, K. S. Chichak, J. F. Stoddart, G. Grüner, *Nano Lett.* **2006**, 6,
- (80) T. Nakanishi, A. Bachtold, C. Dekker, *Phys. Rev. B*, **2002**, 66, 073 307.
- (81) Website from [http://en.wikipedia.org/wiki/Calcium\\_in\\_biology](http://en.wikipedia.org/wiki/Calcium_in_biology)
- (82) A. C. R. da Silva, F. C. Reinach, *Trends biochem. Sci.* **1991**, 16, 53.
- (83) M. Zhang, T. Tanaka, M. Ikura, *Nat. Struct. Biol.*, **1995**, 2, 758.
- (84) Website from <http://en.wikipedia.org/wiki/EF-hand>
- (85) B. D. Slaughter, M. W. Allen, J. R. Unruh, R. J. Bieber Urbauer, C. K. Johnson *J. Phys. Chem. B* **2004**, 108, 10388
- (86) Y.M. Lin, P. L. Yung, Y. C. Wai, *J. Biol. Chem.*, **1974**, 249, 4943.
- (87) T. H. Crouch, C. B. Klee, *Biochem.*, **1980**, 19, 3692.
- (88) I. Heller, A. M. Janssens, J. Mannik, E. D. Minot, S. G. Lemay, C. Dekker, *Nano Lett.*, **2008**, 8, 591.
- (89) J. D. Johnson, C. Snyder, M. Walsh, M. Flynn, *J. Biol. Chem.* **1996**, 271, 761.
- (90) O. B. Peersen, T. S. Madsen, J. J. Falke, *Protein Sci.* **1997**, 6, 794.

- 
- (91) A. Lewin, G. R. Moore, N. E. Le Brun, *Dalton Trans.* **2005**, 3597.
- (92) A. Crow, T. L. Lawson, A. Lewin, G. R. Moore, N. E. Le Brun, *J. Am. Chem. Soc.* **2009**, 131, 6808.
- (93) F. Frolow, A. J. Kalb, J. Yariv, *Nat. Struct. Biol.* **1994**, 1, 453.
- (94) S. K. Weeratunga, S. Lovell, H. Yao, K. P. Battaile, C. J. Fischer, C. E. Gee, M. Rivera, *Biochem.* **2010**, 49, 1160.
- (95) T. L. Lawson, A. Crow, A. Lewin, S. Yasmin, G. R. Moore, N. E. Le Brun, *Biochem* **2009**, 48, 9031.
- (96) H.-L. Liu, H.-N. Zhou, W.-M. Xing, J.-F. Zhao, S.-X. Li, J.-F. Huang, R.-C. Bi, *FEBS Lett.* **2004**, 573, 93–98.